

ABSTRACT

DIWAKAR, NIDHI MALLIK. New Principles and Applications of Active Particle Propulsion Driven by Electrical and Chemical Gradients (Under the direction of Dr. Orlin D. Velev).

The “self-propelling” or “active” microparticles are an emerging class of colloidal species that draw energy from their environment to power their motion. Their main feature allowing the propulsive motion is the principle of breaking symmetry to create a localized gradient, whether it be physical or chemical. A variety of methods to induce this self-propulsion have been explored, including stimulation by magnetic, electric, acoustic, optical, biological, and chemical means. Depending on their size scale and subsequent characteristics in materials and dynamics of motion, these particles offer innovative solutions to many current challenges in key technology fields, such as targeted drug delivery and selective micro-scale surgeries, as well as environmental remediation and nanofabrication. Despite the strides that have been made over the last several decades, the field of active particles faces the ongoing challenge of balancing functionality with increased cost and complexity of fabrication.

In this thesis, we present two concepts that we have developed to address these issues: (1) asymmetric alternating current (AC) field propulsion that would grant multiple new degrees of freedom and (2) creating novel osmotically-driven ultra-simple superdiffusive pellets made from salt and acid particles. First, we introduce a new electrohydrodynamic effect in which spatially homogenous, temporally non-uniform AC signals drive field-collinear motion of symmetric particles. A systematic voltage sweep revealed an unusual power law dependence of particle velocity on field strength ($U \propto E^3$). Reversing the signal asymmetry results in a reversal of particle direction without a change in velocity. Further, the particle velocity decreases steeply with increasing frequency ($U \propto 1/\sqrt{f}$) and increasing particle size. For a temporally nonuniform signal, we observe that the particle (homogeneous sphere) propulsion is size-dependent and hypothesize

that it is a result from the imbalance in counterion motion due to signal asymmetry. The experimental electrophoretic findings are supported by a theoretical model employing a sawtooth wave signal and considering a partial induced-charge screening effect on the powering electrodes. This newly reported temporally asymmetric AC-driven electrophoretic mobility effect opens numerous possibilities for controlling particle propulsion, as it may be combined with induced-charge electrophoresis to drive active motion in two directions independently controlled by signal shape, amplitude, and frequency.

Next, we present a new ultrasimple system of interacting active particles, which we name *superdiffusive pellet*. This pellet represents a vehicle for the collective dispersal of rapidly reacting acid and salt particles. The radial dispersion is driven by a combination of osmotic propulsion, created by the solute concentration gradients established by the reaction between acid and base particles, and Marangoni flows arising from the surface-active nature of the acid particles. The chemical load of the resulting pellet is able to immediately spread rapidly due to the directional propulsion of the particles. We observed the rate of such effervescent spreading for single- and bi-component pellets. The single-component system was evaluated for (i) CA pellets dispensed into AB bulk and (ii) AB pellets in CA bulk. Bi-component pellets composed of varying ratios of AB:CA and AB:SA were dispensed into water. The rate of particle dispersion is tunable by moderating the ratio of reactants, and in turn, adjusting the amount of surface-active material in the pellet. Given the expected ability to rapidly disperse across a relatively large area, this superdiffusive paste has potential in biomedical applications for rapid disinfection and pharmaceutical delivery.

© Copyright 2024 by Nidhi Diwakar

All Rights Reserved

New Principles and Applications of Active Particle Propulsion Driven by Electrical and
Chemical Gradients

by
Nidhi Mallik Diwakar

A dissertation submitted to the Graduate Faculty of
North Carolina State University
in partial fulfillment of the
requirements for the degree of
Doctor of Philosophy

Chemical Engineering

Raleigh, North Carolina
2023

APPROVED BY:

Dr. Orlin D. Velez
Committee Chair

Dr. Robert Riehn

Dr. Melissa Pasquinelli

Dr. Jan Genzer

DEDICATION

I dedicate this dissertation to Suman and Monisha for putting my education first, above all else.

This one is for you.

“The roots of education are bitter, but the fruit is sweet.” – Aristotle

BIOGRAPHY

Nidhi Diwakar was born in Brampton, Ontario, Canada. After moving to India followed by the US, she and her family settled down in Raleigh, NC. She received her bachelor's degree in robotics engineering from Worcester Polytechnic Institute in Massachusetts. While finishing her undergraduate degree, Nidhi worked as an REU student for Dr. Orlin D. Velev, where she first learned about the fascinating field of active particles. After working in the avionics industry for a few years, she turned her focus to graduate school, and returned to NCSU in 2019. Although her loyalty lies unwavering with robotics, she has enjoyed her journey into chemical engineering and active particles research under Dr. Velev's mentorship.

ACKNOWLEDGMENTS

I would first like to thank my advisor, Dr. Orlin D Velev, for his guidance and mentorship over the last many years. His creativity is seemingly endless and his enthusiasm for science is infectious. As a professor said to me once at a conference, “He must generate 1000 ideas a minute!”. To him, I credit my fascination with colloidal science.

I would also like to thank my committee – Dr. Melissa Pasquinelli, Dr. Robert Riehn, Dr. Lilian Hsiao, and Dr. Jan Genzer – for their support and scientific guidance over the course of my time in this program. In addition, I would like to recognize the mentorship and technical insights I have received from our collaborators, Dr. Gilad Yossifon and Dr. Touvia Miloh, whose expertise in electrokinetics has shaped my deep appreciation for the field. I am so grateful for the excellent microbiology training and advice I received from Eduardo Barbieri and Dr. Stefano Menegatti. I must also extend a huge thank you to my undergraduate researchers Rachel Sides and Max Destino for their dedication and willingness to follow me down into the rabbit hole of research without hesitation.

My experience in this program would not have been the same without the incredible people I had the great fortune of meeting. I want to thank Yosra, Rachel, Lucille, Abhirup, and Haeleen for making the day-to-day Ph.D. experience enjoyable. Sneha and Mike, you have been my partners in crime, a shoulder to cry on, a listening ear. Words cannot express how lucky I am to have found you. I would like to recognize Danielle Riegel, Sandra Bailey, and Mike Mantini for all that you do for the department and all that you have done to make my life easier. I would also like to thank my fellow '21-'22 GSA board members for making it an unforgettable experience. You have set the bar so high.

I am grateful to my family and friends for providing me with unconditional support and encouragement (and home-cooked meals!) throughout these years. Sam, you have been an amazing partner, friend, sounding board, chauffeur, and problem solver. Thank you for following me down to NC and, more importantly, staying put. Lastly, I would like to thank anyone who has taken the time to share a coffee or a meal with me or extend a helping hand in my work. In a world ruled by productivity, your generosity with your time will always be remembered.

TABLE OF CONTENTS

LIST OF TABLES	viii
LIST OF FIGURES	ix
Chapter 1 – Introduction: AC Field- and Chemically-Driven Active Particles	1
1.1 An Overview of AC Field-Driven Active Particles	2
1.2 AC-Electric Field Effects in Particle Systems	3
1.3 Classes of Particles that Can Exhibit AC-EHD	7
1.4 Motility of Particles with Engineered Shape	9
1.4.1 <i>Simple asymmetric particles</i>	9
1.4.2 <i>Doublets and multi-particle dynamic assemblies</i>	11
1.4.3 <i>Particle actuation and control with asymmetric and multiple fields</i>	17
1.4.4 <i>AC Propulsion of engineered particles</i>	20
1.5 An Overview of Chemically Driven Active Particles	24
1.5.1 <i>Bulk-Operating CDAPs</i>	28
1.5.2 <i>CDAPs Powered by Interfacial Tension Gradients</i>	30
1.5.3 <i>Collective Behavior of CDAPs</i>	32
1.6 Dissertation Outline	35
Chapter 2 - Active Microparticle Propulsion Pervasively Powered by Asymmetric AC Field Electrophoresis	36
2.1 Introduction	37
2.2 Materials and Methods	39
2.2.1 <i>Preparation of Electrodes and Particles</i>	39
2.2.2 <i>AC Signal and Motion Capture</i>	40
2.3 Results	41
2.3.1 <i>Velocity Dependence on Signal Asymmetry</i>	41
2.3.2 <i>Velocity Dependence on Field Strength</i>	43
2.3.3 <i>Velocity Dependence on Signal Frequency and Particle Separation</i>	46
2.3.4 <i>AFEP Motility of Metallic and Metallodielectric Particles</i>	50
2.4 Discussion	52
2.4.1 <i>Origins of Polarization and Motility</i>	52
2.4.2 <i>Numerical Correlation of Motility to Field Parameters</i>	54
2.5 Conclusions	55
Chapter 3 – Superdiffusive pellet from active particles driven by collective effervescent phenomena	57
3.1 Introduction	58
3.2 Materials and Methods	59
3.2.1 <i>Particle and solution preparation</i>	59
3.2.2 <i>Experimental setup</i>	60
3.3 Results	61
3.3.1 <i>Spreading behavior of a single-component pellet</i>	61
3.3.2 <i>Surface vs bulk activity</i>	64
3.3.3 <i>Spreading behavior of a mixed-component pellet</i>	65
3.4 Discussion	67

3.4.1 <i>Mechanisms driving collective particle propulsion</i>	67
3.4.2 <i>Scaling of particle velocity with driving forces</i>	72
3.5 Conclusions.....	75
Chapter 4 – Summary and Future Outlook	77
References	97
Appendices	116
Appendix A.....	117
Appendix B.....	121
Appendix C.....	129

LIST OF TABLES

Table 2.1	Table summarizing the fitting results determined by using OriginLab for six models that were applied to the field strength data.....	45
-----------	--	----

LIST OF FIGURES

Figure 1.1	Summary of common AC-electric field effects in particle systems.....	3
Figure 1.2	Tiered classification of particles that may exhibit AC-EHD motility.....	7
Figure 1.3	Key examples of Janus and other simple asymmetric particles that exhibit AC-EHD motility	10
Figure 1.4	Examples of dynamic motion of colloidal dimers and assemblies under AC electric field actuation	13
Figure 1.5	Recent examples of systems that can be controlled jointly by AC-EHD and other stimuli.....	17
Figure 1.6	Representative examples of electrically powered engineered particles	22
Figure 1.7	Schematic depicting concentration gradients driving propulsion of chemically driven active particles	26
Figure 1.8	Examples of CDAPs designed to operate primarily in bulk solvent conditions	29
Figure 1.9	Key examples of CDAP systems propelled by interfacial tension gradients	32
Figure 1.10	Examples of collective behavior observed in CDAP systems	33
Figure 2.1	Schematic of experimental cell with input parameters of asymmetric signal.....	39
Figure 2.2	Normalized particle velocity data as a function of signal asymmetry with COMSOL snapshots	42
Figure 2.3	Particle velocity data as function of field strength	43
Figure 2.4	Combined particle velocity data as a function of frequency	48
Figure 2.5	Particle separation data with micrographs.....	50
Figure 2.6	Independent driving of metallodielectric particle motility in two directions via the combined effects of AFEP and ICEP	51
Figure 3.1	Schematic outlining the experimental set up and systems studied.....	61
Figure 3.2	Area coverage data were collected for single-component pellets	63
Figure 3.3	Solute front spreading data for CA pellet dispensed into AB solution	65
Figure 3.4	Area coverage data collected for two mixed-pellet systems	66
Figure 3.5	Mechanisms of superdiffusive pellet dispersion	69
Figure 4.1	Particle tracking snapshots of 10 μm Au-PS JPs under varying frequencies	81
Figure 4.2	Micrographs of collective behavior under AFEP.....	82
Figure 4.3	Example of a proposed vertical field setup	83
Figure 4.4	Reported surface tension measurements for four surface-active organic acids	85
Figure 4.5	Snapshots of the spreading of bi-component AB:OA pellets.....	86
Figure 4.6	Snapshots of highly compressed AB:CA pellets traversing across the air-water interface	87
Figure 4.7	Examples of the possible design patterns of engineered superdiffusive pellets.....	88
Figure 4.8	Reaction mechanisms for 8-HPTS and 2-nitrobenzaldehyde.....	89
Figure 4.9	Illustration of our superdiffusive pellet for dermal wound treatment	91
Figure 4.10	Four types of model dermal wounds produced on porcine gelatin discs	92
Figure 4.11	Results of pellet spreading and penetration in gelatin trench model experiments ...	93
Figure 4.12	E. coli contact assays to assess disinfecting capacity.....	94
Figure 4.13	Snapshots showing the progression of spreading of AB:5-ALA	95

CHAPTER 1

Introduction: AC Field- and Chemically Driven Active Particles

1.1 An Overview of AC Field-Driven Active Particles

Active particles or “micromotors” are a class of microscale entities that harvest energy from external sources and dissipate it directionally, resulting in their net propulsion. In most cases, the motion is generated due to symmetry breaking in particles’ shape, size, or composition, directing the external energy into kinetic motion. Through theory, simulations and experiments, researchers have studied extensively the self-propulsion and assembly behavior of anisotropic spherical colloids, such as spherical Janus Particles (two-faced particles, abbreviated JP) [1–16] that enable control over their self-propelling behavior as well as collective effects [17–25]. As this research field has matured and expanded, researchers have introduced novel classes of particles with complex designed shape and composition, many of them resulting from advances in micro- and nanofabrication [26]. Such particles include, for example, dimers [27], chiral and shaped clusters [11,28], gear-shaped micro-objects, and super-colloidal spinners and motors [27,29–32].

Active particles can be defined as ones that harvest the energy provided by external fields traversing their medium and convert it into directional motion by means of locally induced gradients coupled to energy dissipation into the surrounding fluid [33]. Such particles can be energized by several physical mechanisms, where the energy needed for propulsion is provided by light, catalytic reactions, magnetic fields, ultrasound, or electric fields [34–41]. Of these, AC electric fields are of particular interest since they are a facile means to remotely power the active particles, while their effects can be tuned through the parameters of the AC signal. In turn, this results in intriguing electrokinetic behaviors including propulsion, rotation, and particle-particle interactions [32,42–44]. Distinct electrokinetic mechanisms, e.g., electrohydrodynamic (EHD) flow [45–47], self-electrophoresis through diode rectification [48,49], induced charge electrophoresis (ICEP) [50,51], and self-dielectrophoresis (sDEP) [52], can be modulated by

altering the field strength, frequency, and bias. Further, electrical actuation resolves the issue of finite energy supply associated with fuels, such as the commonly used hydrogen peroxide [53,54], and the challenge to manage chemical fuels in a biological environment. Additionally, it has been shown that the same electric actuation can be used simultaneously to accomplish both propulsion of active particles and manipulation of cargo, proving the robustness and versatility of AC electric energy [43].

1.2 AC-electric field effects in particle systems

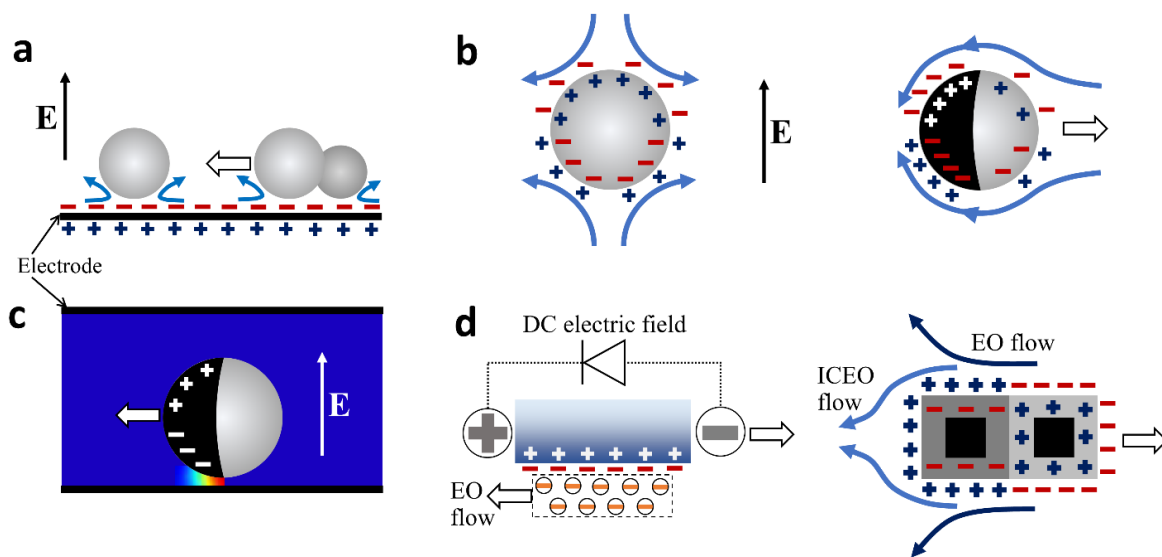


Figure 1: Summary of common AC-electric field effects in particle systems: **a)** Schematic of EHD flow around a stationary spherical dielectric particle (left) and asymmetric dimer experiencing propulsion (right) in a vertical electric field. **b)** Depiction of quadrupolar induced charge flow due to application of a steady state electric field that triggers the dipolar charges in the electrical double layer of the particle (left). A metallodielectric spherical particle with a hemispheric gold coating has asymmetric polarization (EDL around the gold is strongly polarized), resulting in induced charge electrophoretic motion (right). **c)** As a result of dual symmetry breaking of a Janus sphere near a wall, a nonuniform field gradient interacts with the induced dipole in the metallic coating and generates a propulsion force with the metallic half forward, which occurs in the high frequency regime. **d)** A diode particle system and its equivalent electric circuit. Localized electroosmotic flow propels the particle due to the direct-current (DC) field rectified from an external AC electric field. ICEP and diode-based propulsion jointly propel the microparticle. ICEO flow and EO flow (due to diode generated DC field) are shown by arrows (right).

A particle subjected to an AC electric field can experience the effect of a few different electrohydrodynamic mechanisms based on the applied strength and frequency of the electric field (Figure 1). For a particle near the bottom electrode in a parallel-plate electrode configuration (Figure 1a), mobile charges are induced within the electrolyte interfacing the electrode, forming an induced electric double layer (EDL). The presence of the particle near the electrode disrupts the uniformity of the applied electric field and results in a tangential field component that acts on this induced EDL to generate EHD flow around the particles [47,54–58]. This flow causes either repulsion or aggregation of particles near the electrode surface and may also elevate the particles from the substrate [58,59]. The symmetric EHD flow around a symmetric particle (e.g., isotropic spherical particle) will not result in net particle motion. However, if the particles have asymmetry in the shape (e.g., two different sizes of lobes of a colloidal dimer), an unbalanced flow surrounding the different lobes will generate a net motion (Figure 1a). EHD flow is generated at the lowest frequency regime in comparison to the ranges of frequencies for the other mechanisms. The characteristic frequency of the EHD is:

$$f_{EHD} = D/(2\pi\lambda_o H) \quad (1)$$

which corresponds to the charge relaxation time of the EDL induced at the electrolyte-electrode interface wherein λ_o is the Debye layer length, $2H$ the distance between electrodes and D the ionic diffusivity of the electrolyte (expressed here for the simplest case of a symmetric electrolyte, e.g. [47]). A maximum in the EHD effect is expected to occur around this frequency since for higher frequencies the induced EDL does not have time to be fully established, while for smaller frequencies the induced EDL screens the powered electrode and with it also the ability of the

electric field to penetrate the microfluidic chamber [30,47]. The particle propulsion velocity is a function of the frequency as well as electric field strength ($U \propto E^2$). The speed and direction of motion can be altered by changing the geometry and anisotropy through variation of particle properties.

For a surface with fixed natural charges, the electric field that acts on the EDL results in tangential body force that generates linear electroosmotic (EO) flow [50,51,60]. In contrast, in a polarizable free solid particle, the non-uniform induced zeta potential leads to a non-linear electrokinetic phenomenon termed induced charge electroosmosis (ICEO), which acts on its own induced EDL. Particle velocity under this effect can again be scaled as $U \propto E^2$, although in some systems there is a tendency to transition towards linear behavior under high voltage fields [61]. The induced EDL is dipolar in nature and results in a quadrupolar flow (Figure 1b, left), which due to its symmetry does not lead to net motion of a freely suspended particle. However, introducing asymmetry in the system will distort the symmetrical quadrupolar ICEO flow and generate a net electrophoretic motion [2,62]. For spherically shaped particles, this is commonly realized by coating one of its halves with a metallic layer, thus forming a Janus particle. The more intense unbalanced ICEO flow on the metallic coated hemisphere results in net propulsion of the particle with its dielectric side forward (Figure 1b, right) in a direction that is perpendicular to the applied electric field [52]. The direction of motion is due to the orientation of the induced dipole along the metallodielectric interface (Figure 1b, right). The ICEO flow decays at frequencies beyond the charge relaxation time of the induced EDL, which is also known as the RC time for charging the double layer [51]. This flow can be expressed as:

$$f_{ICEO} = D / (2\pi\lambda_o a) \quad (2)$$

where a is the characteristic particle's length scale. Beyond a certain frequency, the metallodielectric JP reverses direction with its metallic hemisphere forward. This effect, termed self-dielectrophoresis (sDEP), has been associated with a net electrostatic force that is generated in the high frequency regime where the induced EDLs on both the polarizable hemisphere of the JP as well as that on the powered electrode are partially screened (Figure 1c) [52]. Typical frequencies that were experimentally observed for a 5-10 μm metallo-dielectric JP within a low conductivity solution ($\sim 10^{-5}$ - 10^{-3} M KCl) are $f_{EHD} \sim 10$ -100Hz, $f_{ICEO} \sim 1$ -10kHz and reversal from ICEP to sDEP ~ 10 -100kHz [30,52].

Yet another electrokinetic self-propelling mechanism stems from the internal asymmetry of the particle conductance. This can be achieved by using semiconductor diodes as particles in kind (Figure 1d, left). The diode particles rectify the applied external AC electric field by conducting in one direction only. The resulting DC electric field component between the electrodes of each diode drive electroosmotic ionic flow along the surface and lead to the particles' self-propulsion [48]. This mechanism can also be used to remotely power electrohydrodynamic diode pumps embedded in microfluidic devices [48].

1.3 Classes of particles that can exhibit AC-EHD

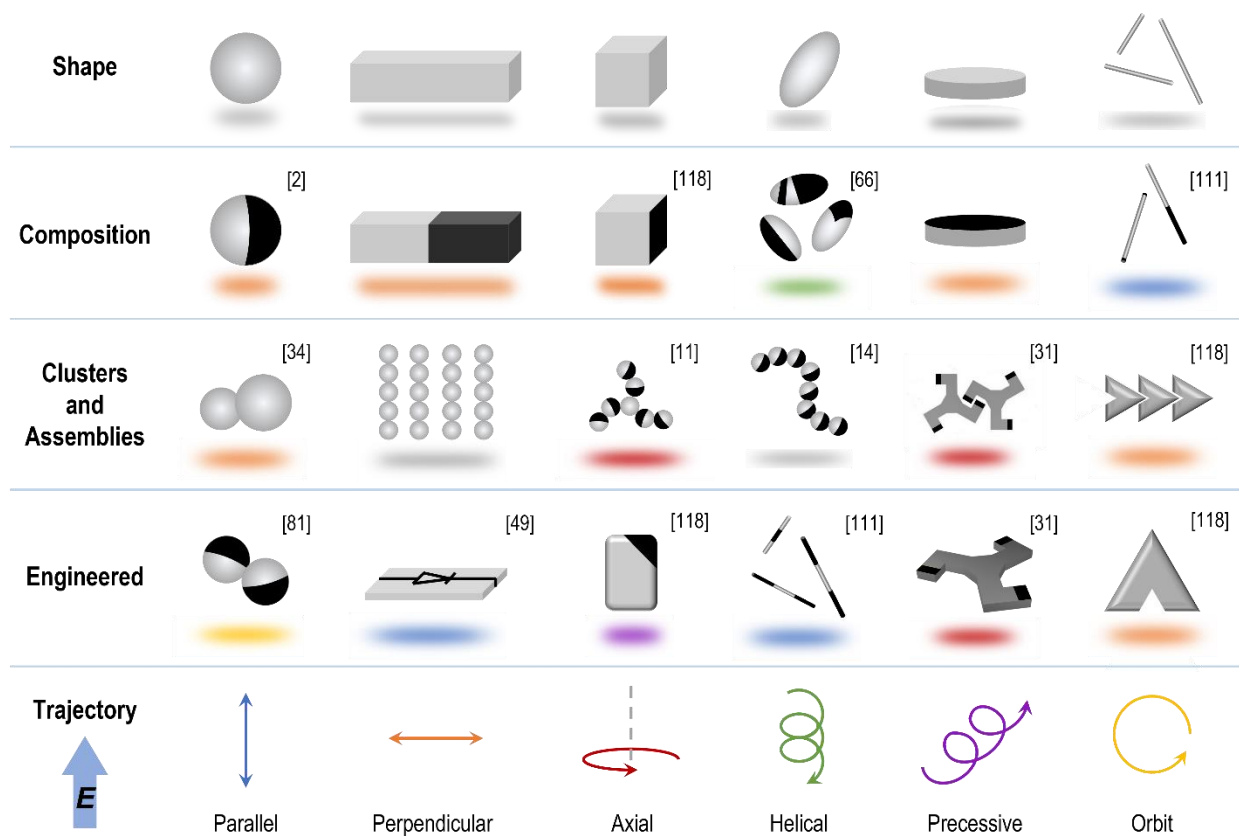


Figure 2. Tiered classification of particles that may exhibit AC-EHD motility. From top to bottom, particles can vary in shape, composition, number (via clusters and assemblies) and engineered design. These features, directing the EHD flows can produce a rich variety of trajectories. The color of the shadow under each unit corresponds to the color of its expected EHD-driven trajectory (bottom row). The trajectories row contains many of the most common examples but is not exhaustive.

Over the last several decades, we have seen the development of a rich variety of active particles that exhibit unique trajectories and behaviors as a result of AC-EHD effects. Due to the diverse particle features that contribute to these effects, it can be challenging to systematically analyze the rich phenomena resulting from this. One can examine these effects via a system of classification for these particles in which complexity builds through the following tiers: shape, composition, number (via clusters and assemblies), and engineered design. A schematic of this

classification with representative examples for each category is presented in Figure 2. This figure also presents the observed or expected types of corresponding trajectories.

In understanding the effect of particle shape on AC field motility, one can consider the number of foci or vertices present as well as the distance and angle between these points, which effectively define the shape-based asymmetry of the particle. The localized AC-EHD effects at these points combine to induce various modes of particle motion. Particle anisotropy can also be varied through patches, coatings, and body composition, often resulting in a difference in polarizability between the regions. However, the trajectories evoked by simple shapes or coatings are often limited to linear-type motions. Incorporating asymmetry in both shape and composition can evolve trajectories into helical paths [20,63]. Recent advances have made the transition from static field-driven assemblies to dynamic, multi-component active clusters, demonstrating behaviors such as rotation, flagellar motion, and linear trains [11,12,14,27]. These clusters and assemblies are generally comprised of individually active particles with attractive or interlocking interactions, leading to increasingly intricate EHD interactions within the larger group [28,30]. The modular nature of these clusters provides additional flexibility in design without the need for sophisticated fabrication techniques. However, such dynamic assemblies are still limited in complexity and shape. Thus, the final tier of our classification pertains to the engineered design and fabrication of more sophisticated AC-field propelled active particles.

The making of engineered active particles involves rational design of the structure along with moderate to high complexity in fabrication. For example, the fifth engineered particle in Figure 2 is a “supercolloidal spinner”. This gear-like particle contains three arms, each with a metal patch near the tip, and was fabricated with lithographic techniques [30]. The spinner is designed with the intention of inducing EHD flow effects in multiple locations on the particle. The last row

in Figure 2 presents the various trajectories one can expect to observe with AC field driven active particles, where the color of the shadows under each particle in the rows above matches the similarly colored trajectory. One additional degree of EHD-driven rotational motion can be observed by various types of Quincke rollers [64–68], but such DC-based systems fall outside the scope of this review on AC field-driven particles. All trajectories listed are derived from previously reported results, but one can imagine numerous other possible paths, such as undulatory waves, levitation, and flipping.

1.4 Motility of particles with engineered shape

1.4.1. Simple asymmetric particles

The simplest type of asymmetric particle is the Janus sphere, in which the two constituent hemispheres vary in composition [1]. Janus spheres have been designed to respond to a variety of stimuli, which may be magnetic, electric, light, acoustic, and chemical [1,69–76]. For the scope of this review, we discuss only those responsive to AC electric fields. Fabrication of electrically-responsive Janus spheres usually involves assembling a monolayer of dielectric (e.g., polystyrene (PS), silica) microbeads onto a substrate and then depositing on top of it a 20-30 nm layer of metal (e.g., Au, Pt, TiO₂, Cr, Fe₃O₄). The second step can be completed by a number of fabrication methods, including thermal evaporation, electron beam evaporation, glancing angle deposition (GLAD) and even microfluidic emulsification [2,20,77,78]. The mechanism of propulsion, at low to moderate (relative to the RC time) frequencies, originates from the imbalance in electroosmotic slip between the two differently polarizable hemispheres of the particle, as originally reported for Au-PS Janus spheres [2] (Figure 3a). Particle motion is in a direction perpendicular to the electric field lines and shows frequency-dependent direction switching. Due to their simple physical nature

but complex behavior, Janus spheres have been the subject of many investigations of active particle propulsion and steering [5,9,51,77].

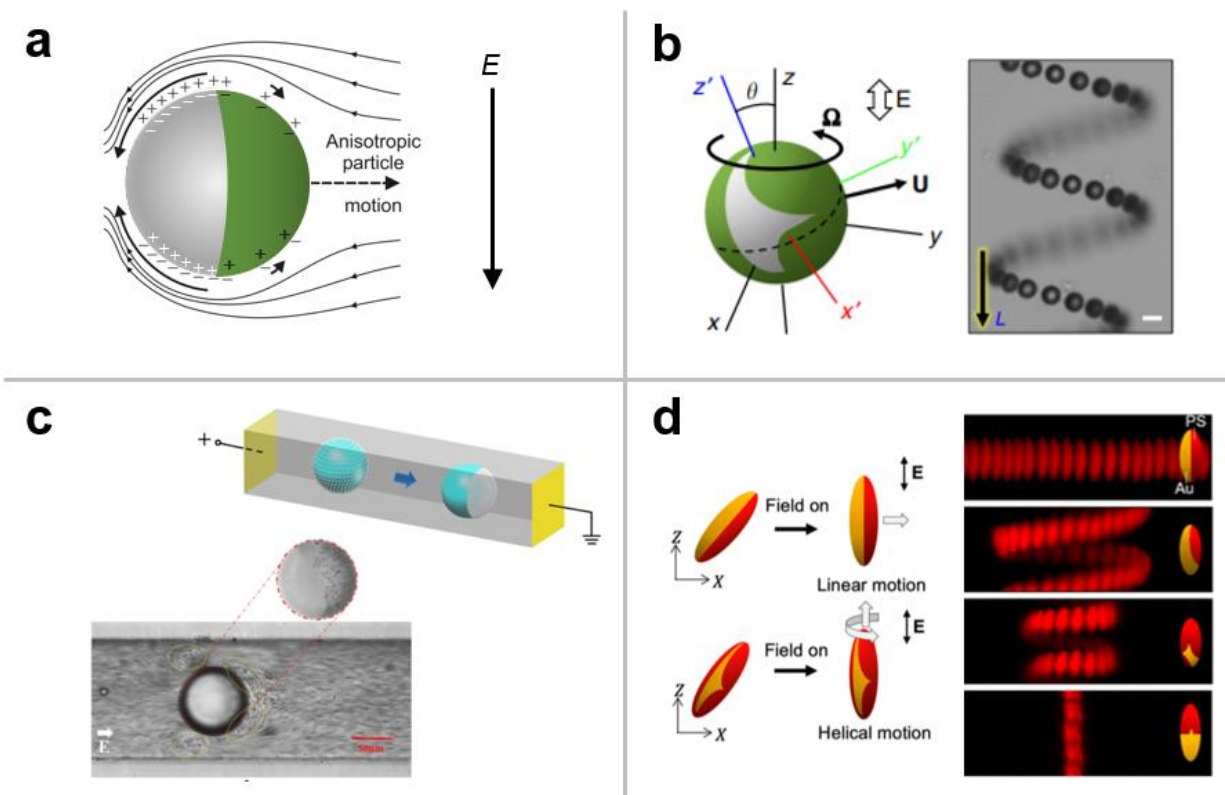


Figure 3: Key examples of Janus and other simple asymmetric particles that exhibit AC-EHD motility. (a) Schematic of ICEO flow in (EDL) of an Au-PS Janus particle with differently polarizable hemispheres [2], (b) Schematic depicting axes of motion of patchy Au-PS spherical particle and superimposed brightfield micrographs showing corresponding 3-D helical trajectories [20], (c) Microscope image of Janus oil droplet with Al_2O_3 nanoparticle half-shell and schematic of microfluidic chamber used for its fabrication [78], and (d) Schematic of patchy Au-PS ellipsoidal particles alongside superimposed brightfield micrographs showing corresponding trajectories based on patchy configuration [63].

As an evolution to more complex anisotropy, Lee et al. fabricated via GLAD patchy spherical particles that move in helical, three-dimensional trajectories under an AC field (Figure 3b) [20]. This is an example of how complex trajectories can be encoded on a simple particle by shaping the patch on its surface. The patch orientation and size guide the EHD flows around the particles, leading to non-cylindrical helices and other programmed trajectories. Li and Li reported

the microfluidic fabrication and field-driven behavior of Janus droplets in which positively charged, mobile Al₂O₃ nanoparticles comprised the hemispheric coating (Figure 3c) [78,79]. Upon exposure to a DC electric field, the nanoparticles collected on one side of the oil surface, rendering the droplet “Janus”. This AC field-driven droplet behavior is attributed to ICEP and electroosmotic flows, both of which can be modulated by the degree of surface coverage with nanoparticles. Such a system offers another degree of flexibility in active particle surface morphology and consequent motility.

Patchy microellipsoids have also received attention as simple AC field-driven asymmetric particles capable of motility on complex trajectories. Lee et al. recently developed PS ellipsoidal microparticles with Au patches formed through thermal evaporation. Due to the layering of particles during evaporation, the patch configurations range from simple lengthwise Janus to angled and fragmented, resulting in both translational and helical ICEP motion (Figure 3d) [63]. The motion patterns were shown to depend strongly on the degree of patch asymmetry along longitudinal and transverse axes. Another interesting study presented recently describes the motion of polyhedral particles based on Metal-Organic Frameworks (MOFs, [64]). These examples show how a multitude of EHD motion patterns can result from relatively simple asymmetric particles.

1.4.2. Doublets and multi-particle dynamic assemblies

Non-spherical particles come with many forms of anisotropy, such as dimers with two lobes. Many studies have reported directed assembly of symmetric/asymmetric doublets [80–84]. Wang et al. reported metal–organic hybrid dimers with various geometric variations and interfacial anisotropy [85]. EHD and ICEO flows control the self-propulsion of this dimer, with direction determined by solution conductivity (Figure 4a). For relatively high conductivities (1×10^{-4} M

KCl), ICEO dominates over EHD flow and linear motion was exhibited with polystyrene lobes facing forward (Figure 4a, left). However, at lower conductivities (e.g., deionized water), EHD overcomes the ICEO flow and consequently, the metallic lobe moved forward. For the case of a dimer with identical chemical composition and size, but differing zeta potential, the dimer was observed to move with the lobe of lower zeta potential facing forward.

Boymelgreen et al. described the orbital motion of metallodielectric JP doublets (Figure 4b, left) under a uniform AC electric field [77]. The orbital motion was shown to depend on the relative orientations of the metallodielectric interfaces of the constituent JPs that form the doublet. The experimental results were explained using a heuristic kinematic rigid body model. Wirth and Nuthalapati theoretically revealed the interactions between a doublet of asymmetric zeta potential and size [86]. The doublet was influenced by two forces: (a) a net vertical force, which depends on lobe size and asymmetry in zeta potential and (b) a net lateral force perpendicular to the electric field, which depends on lobe size asymmetry, difference in zeta potential, and inclination angle of the doublet. The lateral motion of the doublet resulting from the net force was also perpendicular to the electric field. Apart from these forces, a net torque generated rotation of the doublet. These dimers are only capable of propelling along a direction perpendicular to the applied electric field. An active system in which the direction of propulsion is restricted to a single axis is problematic in many applications, such as directed cargo delivery.

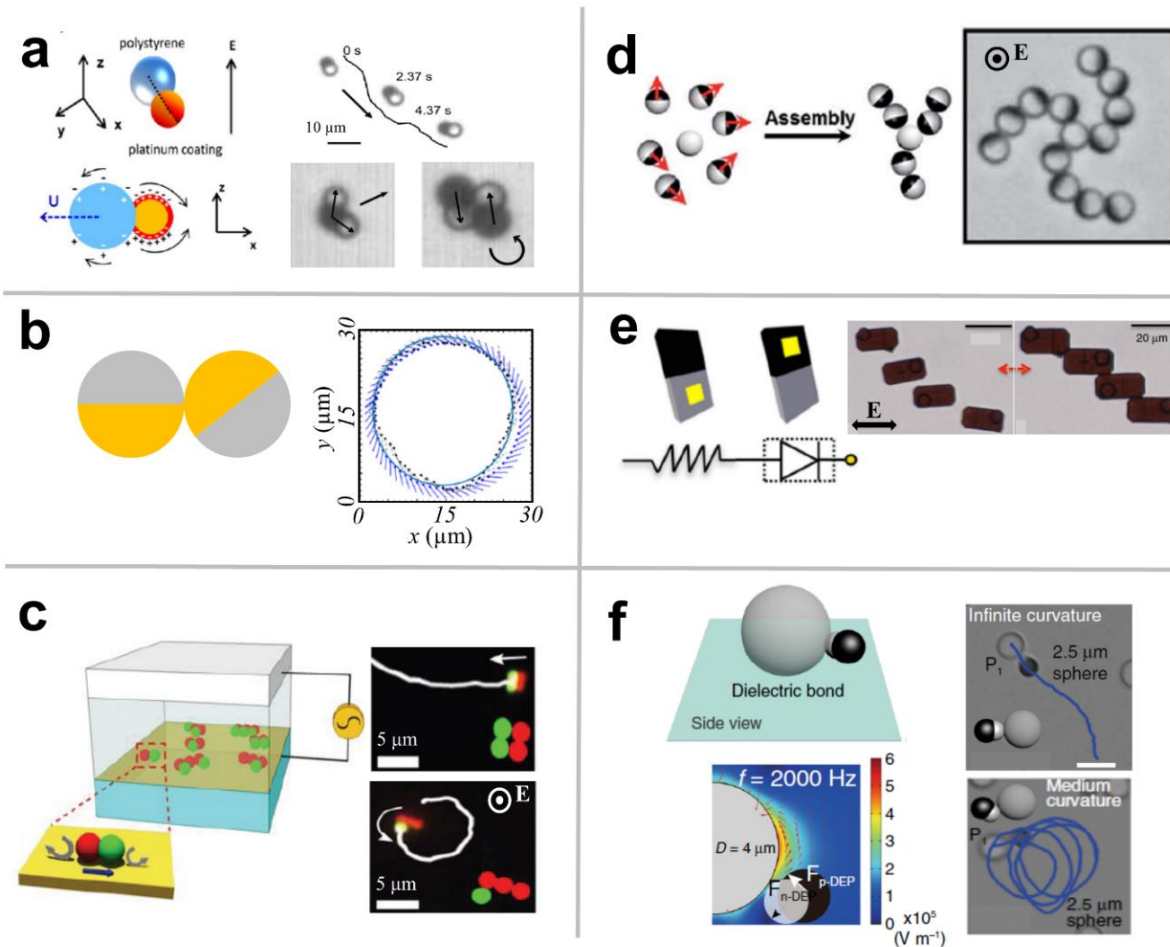


Figure 4. Examples of dynamic motion of colloidal dimers and assemblies under AC electric field actuation: **a**) ICEO flow is generated due to difference in the polarizability of bare and platinum-coated polystyrene lobes. Dimer moves with bare polystyrene lobe forward. Dynamic motion of dimer clusters: Propulsion of two dimers with one common metallic lobe and rotation of head-to-tail dimer doublets (bottom right) [85]. **b**) Schematic of a rigid body doublet. Results of kinematic model (solid blue lines) are compared to experimental data (dashed lines) [77]. **c**) Clusters fabricated by sCAPA. Inset depicts the configuration of colloidal molecules (CMs) with the direction of motion of surrounding fluid. Square-shaped cluster (top right) shows translation, while “L”-shaped cluster exhibits rotation (bottom right) [87]. Typical examples of multi-particle dynamic assemblies: **d**) Schematic presentation of templated growth of chiral cluster. Chiral pinwheel undergoes clockwise motion [11]. **e**) Demonstration of PN-I type semiconductor particle and its equivalent electrical circuit diagram. Assembly (at 1 kHz, right) and disassembly (100 Hz, middle) of 4 PN-I microparticles using electrical signal [88]. **f**) Formation of dielectric bond between central dielectric sphere and a patchy particle. Simulation shows that nDEP attraction leads to bonding between the sphere and the dielectric lobe and pDEP is responsible for metallic lobe bonding. Steering trajectories with infinite curvature (top right) and medium curvature (bottom right) of such colloidal molecules [89].

To address this concern, Zhu et al. investigated the motion of magnetic dimers synthesized under orthogonally applied AC electric and DC magnetic fields [90]. The magnetic field was used to orient the long axes of the dimers in the desired direction and concurrent application of an AC electric field was used to tune the speed. The combined actuation by magnetic and electric fields permits propulsion along a predefined complex trajectory with tunable speed. This strategy may allow future dynamic assembly of complex micromachines which exhibit controlled motion upon application of field gradients. Alapan et al. recently demonstrated the design and assembly of a modular micromachine frame with silica-gold Janus particle “actuators” [91]. The non-uniform electric field gradients around the JPs generate ICEP and sDEP motions. By tuning the frequency of the field, these propulsion methods can interchange with each other, which can be used to design reconfigurable micromachines with a high degree of mobility. The described frame was applied to make a “microcar”, in which different driving modes were made possible by altering the field parameters. This example suggests ways for modular design and multimodal control of future micromachines.

As mentioned earlier, multicomponent clusters show a high degree of broken symmetry which allows higher order tunability when compared with the propulsion and rotation of a single particle. Ni et al. fabricated clusters consisting of organic PS particles and inorganic TiO₂, SiO₂ particles using the sCAPA method [87]. These particle clusters showed complex translation, rotation, and circulation activated by asymmetric EHD flows (Figure 4c). The unbalanced EHD flows around a dumbbell-like colloidal molecule are shown in the inset of Figure 4c. Tuning the geometry and composition of the clusters enables pick-up and transport operations with a high degree of freedom and controllability.

Colloidal dimers can also form chiral clusters. Ma et al. reported how such chiral clusters can be formed by two/four in-plane dimers compacted closely with a central dimer on a conducting surface under an AC electric field [28]. Based on the theoretical analysis, induced dipolar interactions, which comprise (a) in-plane dipolar repulsive forces between the petals and (b) out-of-plane attractive forces between the surrounding petals and central dimer, determined the cluster configuration. Asymmetric chiral clusters generated net EHD flow around the lobes, which induced rotational motion perpendicular to the applied electric field corresponding to their handedness. However, rotation was not found for achiral clusters because they generate a balanced EHD flow. Zhang and Granick presented a chiral, spiral shaped assembly of spherical Janus and homogeneous colloids under an AC electric field [11]. The electric field generates a dipole moment in the center of the uncoated silica particles and each hemisphere of the Janus particles. JPs exhibited head-to-tail attraction between the metallic and silica halves and hence, uncoated silica particles are attached to the metal hemispheres. Upon applying the electric field, spiral structures were formed with a bare silica particle as the core and three or four arms of JPs emanating from the core particle depending on its diameter (Figure 4d). The chiral structure generates self-sustaining rotation.

Recently, Ohiri et al. reported a novel set of motile semiconductor microparticles with varying shape, size, patterned coatings, and polarizability, made by microcircuit fabrication techniques [88]. Figure 4e (left) depicts PN-I type semiconductor particles where electrical properties of the core silicon material were changed by diffusive patterning of a defined region. This process produces a p-n junction on a part of the particle. Under an AC electric field, a strong propulsive flow was generated toward the p-n junction and the metal contact due to combined effects of the rectifying junction and polarizable metal. The particle moved with the non-metal

side facing forward. The metal patch generated anisotropic polarizations on the particle surface and the particle could also be propelled through strong ICEO flow, similar to metallodielectric JPs [2]. At relatively high frequencies, well-organized staggered chains were assembled due to dipolar polarization interactions between the particles (Figure 4e, right). The structure reversibly disassembles at lower frequencies (Figure 4e, middle).

Another notable example is the controlled dynamic interactions of patchy particles reported by Wang and coworkers [89]. By manipulating composition, particle size, and shape, the authors coordinated and arranged the active particles into defined colloidal structures. Figure 4f shows a dielectrophoretic bond between a central dielectric sphere and a patchy particle. Positive DEP (pDEP) attraction is responsible for bonding the metallic lobe of the patchy particle, while negative DEP (nDEP) attraction favors the bonding between a dielectric sphere and dielectric lobe. When a metallodielectric patchy particle is bonded with the central dielectric sphere, the assembled doublet can swim and shows intriguing dynamics. For a bond angle of 90° , the patchy particle pushed the sphere and the assembly showed pure translational motion (Figure 4f, top right). However, when the bond angle was $< 90^\circ$, the direction of motion of the patchy particle did not pass the mass center of the central particle, resulting in a steering motion of the assembly (Figure 4f, bottom right). The curvature of steering depends on bond angle, frequency of the AC signal, and shape of the patch.

1.4.3. Particle actuation and control with asymmetric and multiple fields

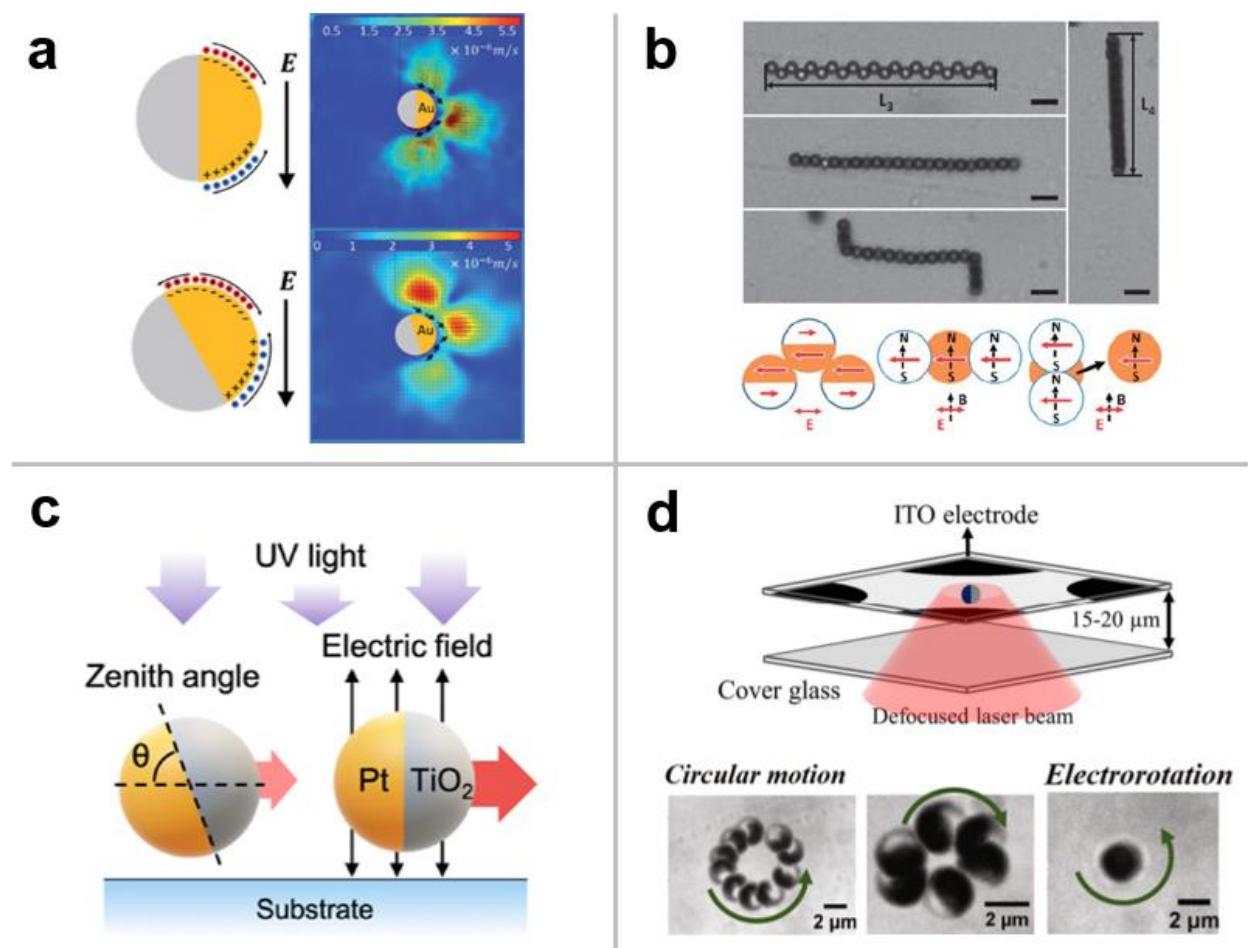


Figure 5. Recent examples of systems that can be controlled jointly by AC-EHD and other stimuli. **a)** Coplanar multifield control of superparamagnetic Au-PS Janus particle and a visualization of the ICEP flow patterns as the orientation of the particle is adjusted via magnetic field [15]. **b)** Chaining, bending, and reconfiguration of Fe₃O₄ Janus particles under combined AC electric and magnetic fields [64]. **c)** Schematic of Pt-TiO₂ Janus particle exposed to AC field and UV light. Concurrent application of stimuli results in significant increase of speed [92]. **d)** Synergistic Janus particle rotation controlled by a defocused laser beam and rotating AC electric field. Below are brightfield microscopy images capturing the particle motion for combined fields below 2 kHz (left), 4-6 kHz (middle), and only rotating AC field (right) [93].

As the field of active particles shifts from fundamental exploration to application-based development, researchers are exploring the emergent field of multifunctional particles that are responsive to multiple field stimuli. Such particles can be subjected to two or more stimuli, either consecutively or simultaneously, to achieve outcomes that would not be realizable with a single

field. These systems offer clear advantages over many current single-stimulus methods by increasing the particles' degrees of freedom and introducing new, nonlinear trajectories. To date, there is a diverse array of multifunctional particles that respond to chemical, biological, magnetic, acoustic, and light-based stimuli [94–99]. In this section, we will highlight key examples of multi-field driven particle systems in which one component is AC field (Figure 5). In both cases below, the secondary field is compatible with the AC field in that it can be fixed precisely through variation of prescribed parameters (e.g., frequency, wavelength, intensity), resulting in reliable particle behavior with an extra degree of control over the competition between the two stimuli.

Combined application of magnetic and AC electric fields is a common strategy for field-directed assembly. Depending on the particle composition, induced magnetic dipoles can persist after the field is removed, whereas electric dipoles do not. Simultaneous magnetic and electric fields can also be employed to control single active particles. One key example is the coplanar multifield control of superparamagnetic Au-PS Janus particles in which the Au film thickness varies (Figure 5a) [15]. It was found that 3 μm JPs with a thick, highly conductive and polarizable, Au shell (70 nm) demonstrated ICEP motion parallel to the electrodes, in contrast with previously reported thin-shell conditions. By introducing magnetic field manipulation of the particles' azimuthal orientation, Lin et al. were able to show the dependence of JP velocity with respect to the field on both coating thickness and dipole angle. Ruditskiy and coworkers reported results from Fe₃O₄-PS Janus particles under both parallel and perpendicular field geometry conditions (Figure 5b) [70]. Such JPs were observed to form chains and contract in the first case, while instead the chains rotated and stacked into two-dimensional sheets under the second condition. Further, it has been shown that chain structure and dynamics is affected by the order in which the fields are applied.

Light is a simple and efficient stimulus that can be applied in a wide range of active systems. Micromotor activity resulting from optical stimulation can be predictably controlled due to the direct relationship to well-defined parameters, namely, wavelength and intensity. Entirely optically-driven active particles have been shown to exhibit a rich variety of behaviors, such as controlled flocking, scattering, and translational behavior [69,100,101]. Hybrid optical and electric active particles have great potential in multi-stimuli controlled systems. Recently, Xiao et al. reported findings of the nonlinear ICEP response of Pt-TiO₂ JPs when the particles were subjected simultaneously to an AC field (EHD) and UV light (photocatalysis of water) (Figure 5c) [92]. It was observed that an individual particle's speed did not correspond to the sum of the speeds under single-stimulus conditions. This was attributed to the tilt rectification caused by the static AC field following the UV illumination. The combination of light and AC electric stimuli can not only affect particle velocity, but also trajectory. Chen and coworkers demonstrated a coupled multi-field effect in which circular motion of an Au-silica JP was modulated by concurrent application of a rotating AC electric field and a defocused laser beam [93]. Once subjected to a laser beam, these particles experience thermophoresis due to light absorption at the gold hemisphere. Combining this effect with a rotating AC electric field causes circular motion of the particles, as opposed to simple electrorotation (Figure 5d). Further, the rotation direction can be tuned by adjusting the frequency of the AC field signal. More recently, it was shown that navigation and steering of individual particles can be enhanced by including a focused laser beam to control orientation [102]. Such synergistic effects are excellent examples of the complex outcomes possible in multi-stimulus active systems.

1.4.4. AC Propulsion of engineered particles

By engineering the shape of particles through microfabrications, researchers have achieved high degree of control over multiple motion mechanisms of active colloids. Shields et al. used photolithography and metal deposition techniques to fabricate complex patchy microspinners (Figure 6a) that exhibited tunable direction, speed, and switchable inversion in a uniform AC electric field [30]. The combination of discrete metallic patches on the body and complex shape of this patchy spinner made switchable use of four mechanisms, i.e., ICEO, sDEP, EHD, and reverse EHD, based on the ranges of frequency of the electric field. Through a series of scaling analyses, authors found that the frequency-controlled inversion in the rotation of nonpatchy microspinners was due to reversal in EHD flows. In addition, patchy microspinners changed the direction of rotation two more times at higher frequency owing to occurrence of ICEP flow and sDEP. Interaction between spinners could result in complicated locking (assembly) and unlocking (disassembly) behavior (Figure 6a, bottom right). Such locking and unlocking operations are useful in many systems, such as studying phase transitions [103,104].

Another way to fabricate complex active particles is the cluster-encapsulation-dewetting method. This method was developed by Wang and co-workers to fabricate patchy colloids of low-symmetry shapes [105]. Particle geometry, size, and configurations of surface patches are key to underlying systems dynamics for controlled locomotion and assembly. Figure 6b (top row) shows a particle with two patches of different sizes located at the two ends of the particle [109*]. The ICEO flows generated from these patches act in opposition to each other. The stronger flow around the bigger patch pushes the particle forward. In such cases, the bigger patch generates the flow while the smaller patch acts as a brake. However, when patches are located asymmetrically, steering motion is generated due to semi-constructive ICEO flow of the two patches (Figure 6b,

bottom row). In such a case, eccentricity is generated for an anisotropic particle and movement of the particle is due to the bigger patch; the smaller patch generates the torque required for steering. The trajectory and direction of steering depend on the location of the small patch.

Semiconductor diodes also show self-propulsion by asymmetry of internal electrical conduction as already discussed previously. When an AC electric field is applied on the electrodes of millimeter-sized diodes, electro-osmotic flow is generated locally along the diode due to the rectification of the applied AC field [48]. The system was miniaturized by Calvo-Marzal and co-workers who used template electropolymerization and electrodeposition techniques to fabricate (PPy–Cd) nanowire diodes [107]. These authors showed the controllable propulsion of CdSe–Au–CdSe and PPy–Cd nanowire diodes driven by a uniform AC electric field. In using another set of effects in similar devices, Sharma and Velez reported how self-propelling microdiodes can be remotely controlled for on-demand steering (Figure 6c) [49]. The individual propulsion path of these electroosmotically driven diodes has been programmed electronically by modifying the applied AC signal. The steering was accomplished by incorporating a DC offset as a wave asymmetry into the AC signal, which generated electrostatic torque between the distribution of ionic charges and asymmetrically polarized diodes. The non-evenly distributed charges along the microdiode surface build up because of the capacitance of the double ionic layer. The authors present an equivalent circuit model and analyze the mechanism of the turning of a diode shown in Figure 6c. The use of a field-encoded DC offset as means of remote diode steering was analyzed and shown to work in a highly controllable and programmable manner [49].

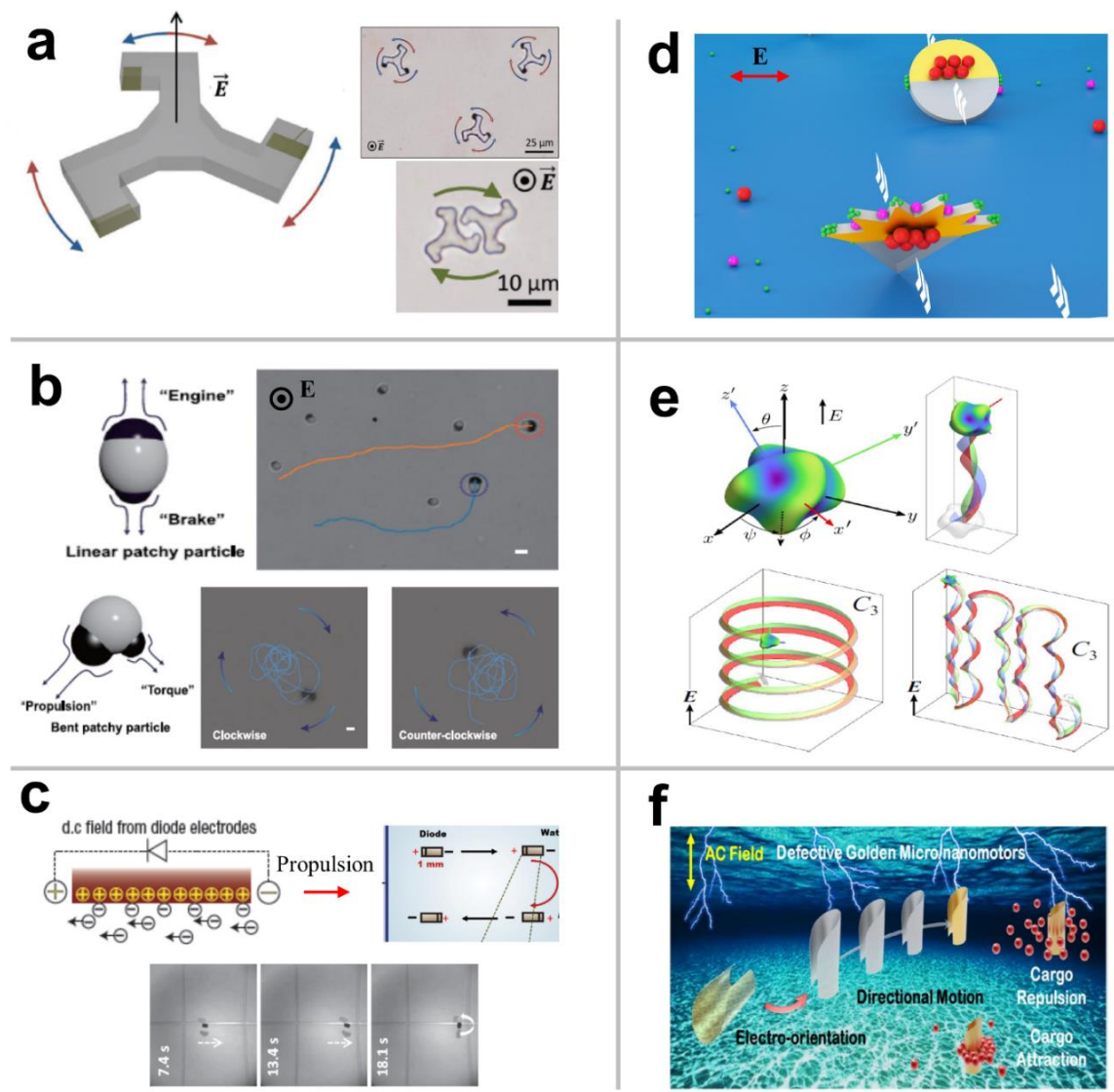


Figure 6. Representative examples of electrically powered engineered particles: **a)** Schematic of supercolloidal spinner of polystyrene with gold coating at the distal ends of three arms. These spinners perform rotational motion under a vertical electric field. The particles exhibit locking at low electric field strength and unlocking (disassembly) at high electric field strength [30]. **b)** Linear translation of big-small two patch particle (top row) under an AC electric field. The big patch serves as an “engine” while small patch acts as a “brake”. Steering of big-small two-patch particle (bottom row) [105]. **c)** Illustration of diode propulsion on water through electroosmosis generated due to DC voltage resulting from the rectification of applied AC field. Depiction of the process of diode steering (top right) and time sequences of diode propulsion and steering [49]. **d)** Illustration of spike and disk-shaped engineered particle with cargo transport through pDEP and nDEP mechanisms. External AC electric field generates strong ICEO flow around the gold coating for overall propulsion and nonuniform field gradients at sharp corners generate DEP forces for cargo loading [32]. **e)** A complex shape polarizable particle whose trajectory can be defined through alteration of its shape and symmetry. Helical trajectory of the complex particle (bottom left) and translation in a different direction of a wobbling cruiser (bottom right) [31]. **f)** Time sequences of the propulsion of a “defective” golden micromotor. It shows electro-orientation, directional motion, and cargo attraction/repulsion behavior [106].

The careful consideration of shape in designing engineered particles can significantly improve particle functionality and robustness. For example, in order to increase the number of cargo loading locations, Kunti et al. designed disk and spike-shaped engineered particles fabricated by a standard lithography process (Figure 6d) and actuated them using in-plane AC electric fields over an insulating substrate [32]. The spike-shaped active particles exhibited an enhanced cargo loading capability relative to the disk-shaped engineered Janus particles. In addition, the authors observed that varying the AC signal frequency and amplitude caused the particles to move tilt angle, reverse direction, and even flip. The tilt angle and flipping events are controlled mainly by ICEP and Maxwell stress tensor (MST) torques, where ICEP torque dominates in the lower frequency range and MST torque plays a major role at higher frequencies. The same group focused on modified metallodielectric pollen to enhance cargo loading capacity with different sizes of cargo [108]. Sharp corners of the pollen spikes generate sharp local gradients in the electric field and create multiple dielectrophoretic traps for cargo loading.

In a systematic study, Brooks et al. examined theoretically and numerically ICEP phenomena of particles with different symmetries (Figure 6e, top) and reported how particle shape can be used to program their numerous complex dynamic behaviors [31]. 3D analysis has been performed to identify translational and rotational trajectories allowed by symmetry. For each particular shape of a polarizable particle, the authors matched the specific dynamics using the numerical technique of boundary integral formulation containing hydrodynamic and electrostatic problems. Apart from circular, translation, and rotational motion, analysis presented helical motion, oscillatory trajectories, and complex periodic orbits of the particles with specific corresponding shapes. The authors have shown how the particle trajectories can be modified through changes in their shape and asymmetry. Figure 6e (bottom images) shows two different

trajectories: helical and zig-zag paths for a complex particle [31]. A helical trajectory was also seen for metallic and non-metallic microhelices in silicon oil media using a DC field [109]. This micromotor showed a cork-screw-type periodic rotation, the direction of which depends on its chirality (handedness).

Zhuang et al. investigated the dynamics of topologically defective asymmetric particles (Figure 6f) consisting of only one material (e.g., gold) [106]. Glancing angle deposition and membrane electrodeposition methods were used to fabricate active particles that circumvent the material constraints for the particle and substrate. Once the electric field is applied, this particle changes its orientation from horizontal to vertical and performs autonomous motion. Interaction between the electric field and the induced dipole on the thin coating (~50 nm) of the “defective” particle generate torque to align it along the field direction (vertical). The EDL around the particle is asymmetric because of its shape, resulting in a stronger EHD flow generated at the defect-free side as compared to the defective side in the ICEO regime. Such asymmetric particles can attract or repel various cargoes in a tunable way via altering signal frequencies.

1.5 An Overview of Chemically Driven Active Particles

The scientific field of active motile particles is at the cutting edge of present-day research due to the astonishing properties of the self-propelling particles. The key physical challenge in making such particle systems is introducing means for particle-centric motility. Particle propulsion at the microscale and nanoscale is opposed by the viscous forces, while inertial forces are governing movement only at much larger scales [110]. Overcoming the drag force is a key to motile energy dissipation on the microscale, requiring a continuous supply of energy for the particles’ movement. The techniques that may be used to supply the motile particles with external power include using

electric fields, magnetic fields, ultrasound, and light [53,76,111–113]. However, in many cases, external fields are not easily adaptable to larger scale applications, such as environmental remediation, or biological spaces that are difficult to reach. In such systems one may find that it is more strategic to employ chemically powered active particles.

Self-propulsion of chemically-driven active particles (CDAPs), also known as “micromotors”, is commonly achieved via production of the fuel “on site” through catalytic decomposition of hydrogen peroxide [114–118], glucose [119,120], or by photocatalysis [92,101]. The asymmetry in the direction of fuel discharge is essential, and typically is achieved through particle shape or surface anisotropy, such as when using Janus particles [71,72]. The non-uniformity introduces a gradient in the concentration of one species in the vicinity of the particle. Some active systems have been considered as a basis of compelling applications, such as water cleanup and environmental remediation [34,95,121,122]. However, such applications usually require the presence of reactive species in the medium (typically H_2O_2), which makes such applications challenging to implement in the real-world scale. In some cases, the particles can carry and release their own “fuel” [123] such as ethanol [124–126], or an ionic liquid [127]. The motility of the particles driven by Marangoni flows can reach impressive velocities when the “fuel” is an asymmetrically released surface active agent [128,129].

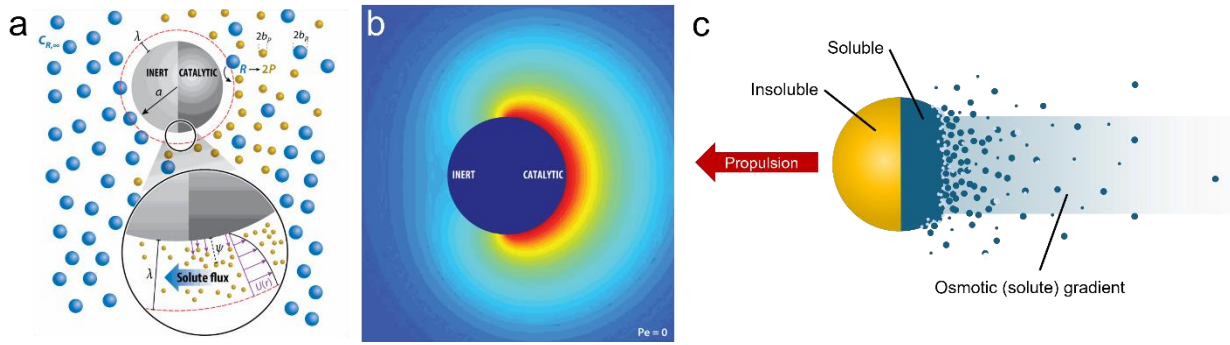


Figure 7: **a)** Schematic depicting concentration gradients of one reactant (blue) and one reaction product (yellow) as colloidal particles surrounding a larger spherical particle with inert and catalytic hemispheres. Accumulation of the reactant product drives migration of those particles towards the inert hemisphere, resulting in self-diffusiophoresis of the larger particle [130]. **b)** Numerical solution of the solute concentration profile around a half inert-half catalytic active particle. Red indicates the reaction products and blue the bath reactant [131]. **c)** Schematic illustrating the direction of particle propulsion with reference to the accompanying osmotic gradient.

The primary phenomenon by which these particles experience self-propulsion is known as “self-diffusiophoresis” and is based on the concentration gradient of the decomposition products in the system (Figure 7) [130,131]. Particle-particle and particle-fluid interactions for these systems are best described by three dimensionless parameters: the Damkohler (Da), Péclet (Pe), and Reynolds (Re) numbers. The Damkohler number represents the ratio of reaction rate to the rate of mass transport:

$$Da = ka/D \quad (3)$$

in which k is the reaction rate constant, a is the particle size, and D is the diffusivity of the solute [132]. The Péclet number describes the relationship between advection and diffusion, which for a particle of radius a moving with directional velocity U is:

$$Pe = aU/D \quad (4)$$

where D is again the diffusivity of the solute [133]. For $Pe \rightarrow 0$, the dissolution will be diffusion-controlled and the self-propelled motion of the particles will be negligible. For finite Pe , the transport will be given by the convective diffusion equation:

$$\mathbf{v} \cdot \nabla C = D \nabla^2 C \quad (5)$$

where C is the concentration of the dissolving species. The Reynolds number relates the inertial and viscous forces in a system:

$$Re = av\rho/\eta \quad (5)$$

for a particle of size a moving with velocity v in a solvent with density ρ and viscosity η [134].

In general, asymmetric catalytic motors show self-diffusiophoretic motion. A high local concentration of the decomposed products near one side of the particles gives rise to an imbalance in osmotic pressure and generates the motion of the motor in the opposite direction of the catalyst. Figure 7 shows three representations of the osmotic gradient around a Janus-style catalytic particle with the resulting direction of motion. Although self-diffusiophoresis can be studied in isolation within theoretical models, experimental studies can rarely decouple the role of this effect from concurrently occurring phenomena such as bubble propulsion [122] and electrokinetics [114]. Such combinations of effects lead to the rich and complex propulsion patterns of CDAPs. In our system, we are exploring this effect in the context of collective motion. The emergence of collective phenomena in systems of interacting active particles is one of the most intriguing aspects of active systems to date [135–138]. Large ensembles of motile particles demonstrate fascinating

phenomena of self-organization and spontaneous pattern formation, as a result of the hydrodynamic and mechanical interactions between the motile entities. This dissertation focuses on the development of an ultrasimple motile particle system that moves while using as a “fuel” the soluble material of the particle itself. We avoid complex fabrication techniques by harnessing a combination of self-diffusiophoresis, chemical reactivity, bubble propulsion, and collective behavior to drive a rapidly propelling, “superdiffusive” pellet. We expand on the background of these effects in the following sections.

1.5.1 Bulk-Operating CDAPs

The vast majority of CDAPs are designed to be used in the bulk phase, where the particle is fully immersed in the solvent, which often also serves the role of a reactant. One of the most commonly used techniques to generate propulsion is the asymmetric catalytic decomposition of H_2O_2 by Pt [98,117,121,139,140] or Ag [141], which was pioneered by Paxton and coworkers in 2004 [114]. One end of a micro- or nanorod containing Pt oxidizes the surrounding medium to produce O_2 , 2H^+ , and 2e^- (Figure 8a). While originally thought to be driven solely by locally generated gradients of O_2 , it was later proposed that diffusiophoresis was coupled with electrokinetic effects due to the production of charged species, and in some cases, bubble propulsion as well.

Bubble propulsion of CDAPs is more frequently achieved through a rigorous reaction between Mg and water [75,95,122,142–144]. These particles contain a small patch of Mg (Figure 8b) which self-sustains movement in water once the passivation layer is removed. Although particle trajectories can be difficult to control, this simple mechanism conveniently obviates the need for complex or potentially toxic fuel sources. Dong et al. reported bubble propulsion arising

from UV-activated CO emission from diphenylcyclopropanone (DHCP) “fuel” that was asymmetrically loaded onto a particle (Figure 8c) [123]. While this system does not require any reaction with the surrounding medium, CO production may be considered detrimental in biological or environmental applications.

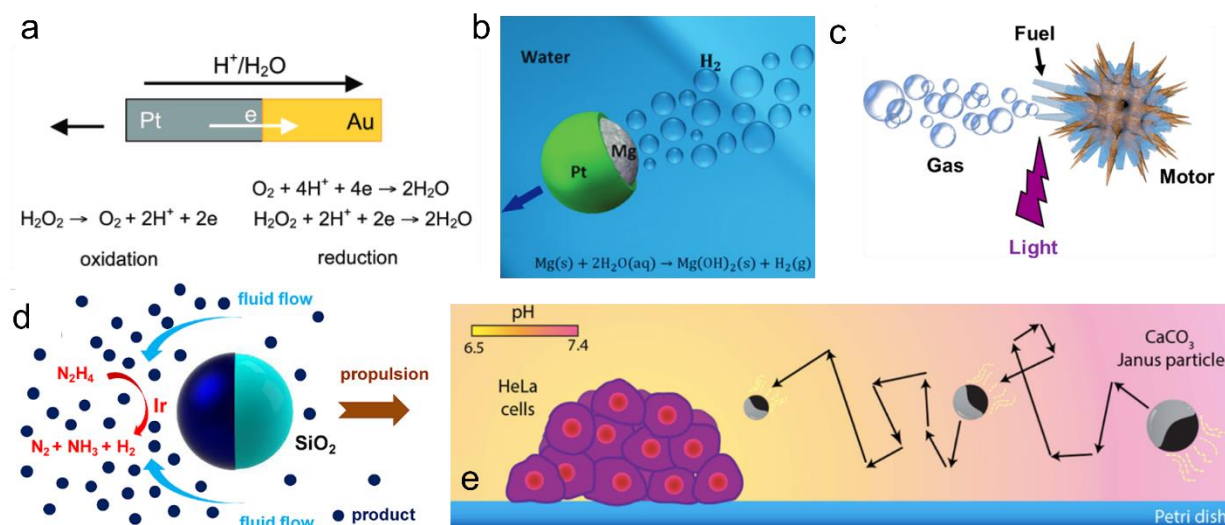


Figure 8: Examples of CDAPs designed to operate primarily in bulk solvent conditions. **a)** Schematic of an Au-Pt bimetallic nanorod propelled by catalytic decomposition of the surrounding hydrogen peroxide medium. The particle is driven by phoretic as well as electrokinetic effects [145]. **b)** Mode of operation of a Pt-Mg active particle. Mg reacts violently with water to yield hydrogen gas (H_2) bubbles. The ejection of these bubbles results in rapid self-propulsion of the particle [122]. **c)** Photochemical micromotor powered by diphenylcyclopropanone (DHCP), a self-sustaining fuel that is activated by UV light. Asymmetric loading of the fuel onto the particle creates imbalanced bubble production, leading to directional motion [123]. **d)** An Ir-SiO₂ Janus particle efficiently decomposes bulk hydrazine at micromolar concentrations to drive propulsion with the SiO₂ hemisphere forward. The primary mechanism of movement for this system is increased osmotic pressure from nonionic decomposition species [72]. **e)** A calcium carbonate (CaCO₃)-Co Janus particle is designed to move selectively towards more acidic bulk areas generated by tumor cells through a simple acid-base reaction coupled with diffusioosmotic flows of the decomposition products [71].

Catalytic micromotors can also experience self-propulsion whose primary mechanism is increased osmotic pressure from decomposition products without the presence of bubbling (Figure 8d and e). Gao et al. demonstrated propulsion of an Ir-SiO₂ Janus particle through decomposition of micro- to nanomolar concentrations of bulk hydrazine [72]. These experiments are unique in

that the reaction products are uncharged, following theoretical predictions of self-diffusiophoresis of “neutral” solutes [130,131]. Systems avoiding the mass generation of bubbles, and thereby bubble bursts, are preferable for internal medical applications, where such forceful disruptions can lead to discomfort and complications. Guix and coworkers reported the selective motion of (CaCO₃)-Co Janus particles along the pH gradient generated by tumor cells [71]. Although the CaCO₃ hemisphere was dissolved in the process, the application of this system at nanomolar bulk concentrations prevented the development of bubbles.

1.5.2 CDAPs Powered by Interfacial Tension Gradients

Another class of CDAPs is those that operate at interfaces, breaking symmetry through surface tension gradients and propelling with the aid of Marangoni flows. Figure 9 summarizes key examples of systems that use these principles to attain self-propulsion. Manjare et al. reported self-assembly of Pt-SiO₂ Janus particles around an oxygen bubble formed by catalytic conversion of surrounding H₂O₂ [146]. Evaporation at the interface induces thermal gradients, which then drives Marangoni flows around neighboring particles, pulling them into the vicinity of the bubble (Figure 9a). CDAPs have also been shown to create and travel along surface tension gradients while partially submerged (Figure 9b-d). Chen et al. showed that an aniline droplet propels due to a combination of surface spreading and the resulting differential surface tension gradients between the front and rear of the droplet (Figure 9b) [129]. A numerical and computation model was developed by Imamura and Kawakatsu to describe CDAP behavior at the air-liquid interface, using the example of a surfactant-propelled particle and analyzing the roles of hydrodynamic, capillary, and Marangoni effects in motility (Figure 9c) [147]. Such effects can also persist on the millimeter scale. Sharma and coworkers demonstrated the self-propulsion of milli-tubes through the

continued release of ethanol from one end (Figure 9d) [128]. Interfacial flows around the particle carry away the “fuel”, leading to oscillatory patterns of propulsion.

Interfacial gradients can also be induced through solubilization of oil in a surfactant medium. Biphasic Janus droplets consisting of dibromooctane and fluorosilicone travel via differential rates of solubilization and gradients between oil “hemispheres” in a non-ionic surfactant solution (Figure 9d) [148]. Izri et al. reported similar self-propulsion of pure water droplets as they are solubilized by reverse micelles in a surfactant medium (Figure 9e) [149]. These seemingly simple systems take advantage of fundamental colloidal interactions to drive a rich variety of active particle propulsion patterns.

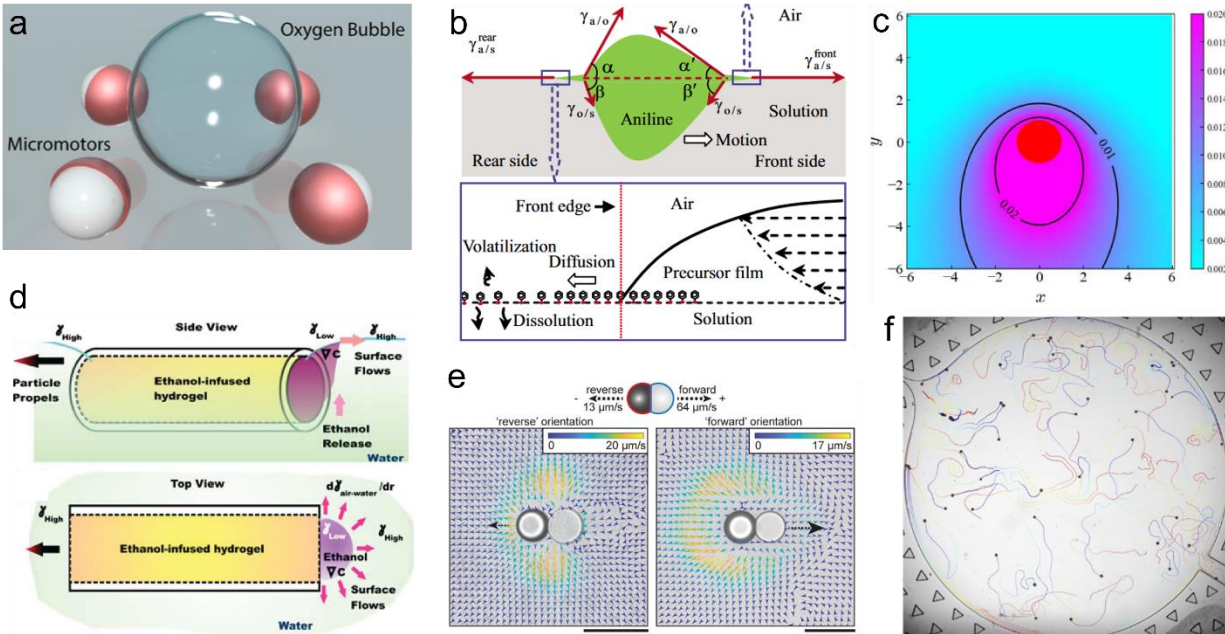


Figure 9: Key examples of CDAP systems propelled by interfacial tension gradients. **a)** Illustration of the attraction of Pt-SiO₂ Janus particles to an oxygen bubble formed by decomposition of H₂O₂. Contrary to diffusiophoresis, the particles travel with their catalytic hemisphere upfront [146]. **b)** Schematic of an aniline droplet self-propelling along an air-solution interface due to differential surface tension gradients between the rear and front of the droplet as well as droplet spreading [129]. **c)** Numerical solution showing surfactant concentration around a CDAP operating at the air-liquid interface. Red indicates a high concentration [147]. **d)** Schematic of a hydrogel “boat” particle that propels due to the continued release of ethanol at the air-water interface, with oscillatory behavior corresponding to cyclical Marangoni flows [128]. **e)** Fluid flow profiles around dibromooctane (red) and fluorosilicone (blue) Janus droplets. The propulsion of the droplets is driven by interfacial tension gradients from oil solubilization in the surfactant solution [148]. **f)** Micrograph of self-propelling water droplets traveling due to solubilization and reverse micelle formation in an oil-surfactant medium [149].

1.5.3 Collective Behavior of CDAPs

Taking inspiration from nature, researchers have for long been fascinated by the self-forming clusters and assemblies seen in groups of active particles. Although there are fewer examples of such chemically-driven systems, this section serves to highlight the mechanisms by which such behaviors are achieved. Switchable attractive and repulsive interactions between microparticles occur most commonly as a result of combined diffusiophoretic and electrokinetic flows during the production and movement of charged decomposition species (Figure 10a-c). Duan et al. reported clustering and dispersion of Ag₃PO₄ microparticles in the presence and evaporation, respectively,

of NH_3 solution [150]. Catalytic conversion of the solvent by the particles produces charged species, which in turn gives rise to competing electrophoretic and electroosmotic effects (Figure 4a). Evaporation of the solution shifts the prevailing mechanism and results in clustering.

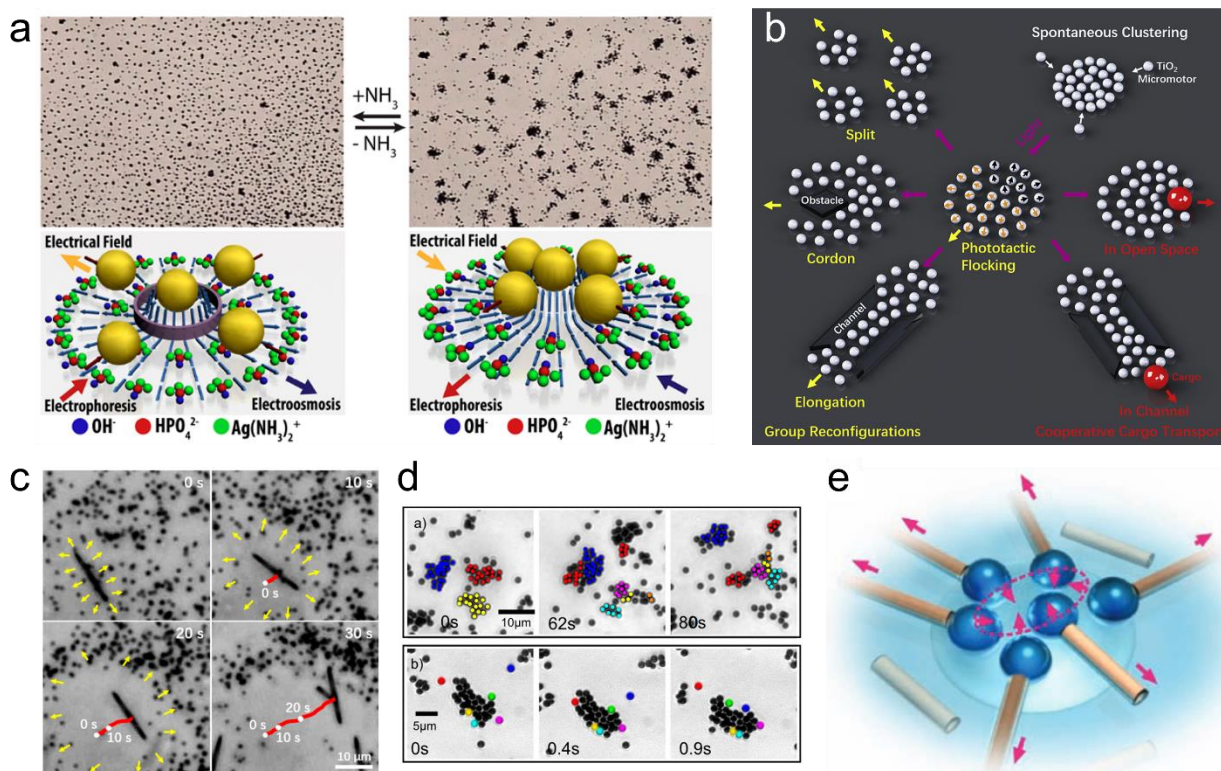


Figure 10: Examples of collective behavior observed in CDAP systems. **a)** Dispersion and clustering behavior of Ag_3PO_4 microparticles in response to the presence and absence, respectively, of NH_3 . Direction of particle motion is influenced by a combination of electrokinetics and self-diffusiophoresis due to the nonredox reaction between the particles and solvent [150]. **b)** Schematic illustrating various collective behaviors demonstrated by photochemically-driven hydroxyl-enriched TiO_2 microparticles in different solutions [101]. **c)** Micrographs showing the chasing-escaping dynamic between passive TiO_2 microparticles and a ZnO microneedle in pure water. Catalytic decomposition between the particles and water generates charged species that interact with each other, leading to combined diffusiophoretic and electrokinetic effects [151]. **d)** Au-Pt Janus particles in H_2O_2 experience clustering behavior due to combined diffusiophoretic flows and attraction between decomposition products [152]. **e)** Attraction between bubbles on the ends of Ti/Cr/Pt catalytic microtubes causes clustering in H_2O_2 [153].

Similar flocking behavior was observed in groups of hydroxyl-enriched TiO_2 microspheres irradiated with UV light in the presence of water, and separately, H_2O_2 [101]. The combination of

light and catalytic behavior allowed enhanced control of particle flocking (Figure 10b), and the clustering/dilation was attributed to a combination of diffusiophoresis and electrokinetic flows. These combined effects are once again harnessed to drive a chasing and escaping pattern between passive TiO_2 microparticles and ZnO microneedles in pure water (Figure 10c) [151]. Conversion of water by TiO_2 and ZnO into their respective charged species leads to intraspecies attraction and repulsion, causing TiO_2 particles to swarm and be repelled by the ZnO microneedle. Particle swarming can be likened to the clustering of bacteria due to gradients of attractive chemical species, such as in the case of Au-Pt Janus particles in H_2O_2 (Figure 10d) [152]. Solovev and coworkers also demonstrated the self-assembly of Ti/Cr/Pt catalytic microstriders in H_2O_2 , where particles were attracted to each other not by catalytic byproducts, but rather by capillary force between bubbles attached to one end of each microtube.

1.6 Dissertation Outline

The rational design of electrically and chemically driven active particle systems can enhance both versatility and efficiency by leveraging the fundamental principles of symmetry breaking. Chapter 2 presents a thorough analysis of microparticle self-propulsion under a temporally asymmetric AC field. We demonstrate how symmetry breaking of the electric signal time characteristics leads to reversible field-colinear motion of homogeneous dielectric microspheres, which we term *Asymmetric Field Electrophoresis (AFEP)*. Particle behavior is characterized as a function of key field parameters and supported by theoretical and numerical models of asymmetric ionic concentration-polarization.

In the third chapter, we discuss the collective active propulsion of simple salt and acid particles that undergo a neutralization reaction. We explore the spreading behavior of single- and bi-component pellets in three bulk conditions. The pellets demonstrate rapid radial spreading outwards at a rate that far exceeds that of molecular diffusion and is hence termed *superdiffusive pellet*. Four mechanisms of propulsion are analyzed, and it is determined that particle motility is primarily governed by advection from rapid gas production and Marangoni flows arising from the use of surface-active compounds. We suggest an optimized ratio of components to maximize spreading efficiency.

The final chapter provides a summary of the findings in this dissertation and suggestions for future directions in which these studies can be extended. AFEP shows promise as a particle separation technique to be integrated into lab-on-a-chip systems. Preliminary results are shared for the application of our superdiffusive pellet in the area of biomedical disinfection. Through this dissertation, we have shown how the simplest forms of symmetry breaking can lead to highly flexible active particle systems with diverse patterns of motility.

CHAPTER 2

Active microparticle propulsion pervasively powered by asymmetric AC field electrophoresis

2.1 Introduction

The particle motility induced by directed energy conversions on a particle level, leading to “self-propelling”, or “active” particle systems, has emerged as a major focus of research activity and interest. Active particles have taken the center stage in colloidal and soft matter research, addressing a number of topics such as biomedical manipulation [143,144,154–157], environmental remediation [95,122,158–162], and nanofabrication [163–165]. A variety of methods to induce such motility have been examined, including application of magnetic, electric, acoustic, optical, biological, and chemical fields. Of specific focus here are externally applied AC electric fields, which give rise to a rich variety of effects of microparticle electrostatics that have been widely investigated and continue to be explored. The use of AC electrophoretic effects enables self-propulsion of microparticles that is rationally designed and precisely controlled. One of the simplest ways to achieve such propulsion is to use particles or media with some type of an asymmetric polarization pattern. Our group reported earlier how an AC-field induced-charge electrophoretic (ICEP) effect emerges when the symmetry of particles is broken in systems of Janus metallodielectric microspheres [2]. It has also been demonstrated that active motility can be imparted by having particles with asymmetric internal conductance, exemplified by microdiode internal current rectification [48,49,107], local gradient effects from wall proximity [52,166], electrohydrodynamic (EHD) flows around particles with asymmetric shapes [27,30,63,167], or by breaking the symmetry of the medium by using liquid crystals [168] or asymmetric electrolytes [169,170]. Another way of inducing directional (but not “active”) motion in particle systems includes the use of potential wells and interdigitated or patterned electrodes, known as ratcheting and traveling wave dielectrophoresis, respectively. Such experiments employ pulsed

rectangular signals with a DC bias to produce a spatially asymmetric potential, which then drives directional motion of particles [171–173].

We present and analyze here another basic effect of symmetry breakdown and particle motility driven by a time-asymmetric AC field. The particles initially used in these experiments are common spherical polystyrene latexes of micron size. The dilute particle suspension is confined in a thin chamber filled with deionized (DI) water. The electric field originates from two planar electrodes on the sides (Figure 1). This electrode configuration, similar to our earlier studies [2], creates an electric field that is homogeneous across the chamber and is tangential to the substrate. The “reference” AC signal provided to the electrodes has a symmetric triangular waveform, typically in the frequency range of 1 to 10 kHz and 30 to 300 V/cm in amplitude. The temporally asymmetric field can be either in the form of a “forward” sawtooth signal that is characterized by a rapid decrease in voltage followed by a slow increase, or a “reverse” sawtooth signal that comprises a rapid increase in voltage followed by a slow decay. These signals are easily programmed and changed on demand by the signal generator. They are characterized here by an asymmetry parameter λ , defined by the expression $2\lambda = 1 - 4t_1/T$ for the “forward” asymmetric signal and $2\lambda = 4t_1/T - 1$ for the “reverse” asymmetric signal, where t_1 represents the time of the first rise/fall of the waveform during a half cycle such that $T/4 > t_1 > 0$ over the period T . Note that $-1/2 < \lambda < 1/2$ such that for a “forward” sawtooth signal ($t_1 = 0$), $\lambda = 1/2$ and for a “reverse” sawtooth signal ($t_1 = 0$), $\lambda = -1/2$ (see Figure 1c) It is also important to note that all signals result in a net zero average time-integrated voltage.

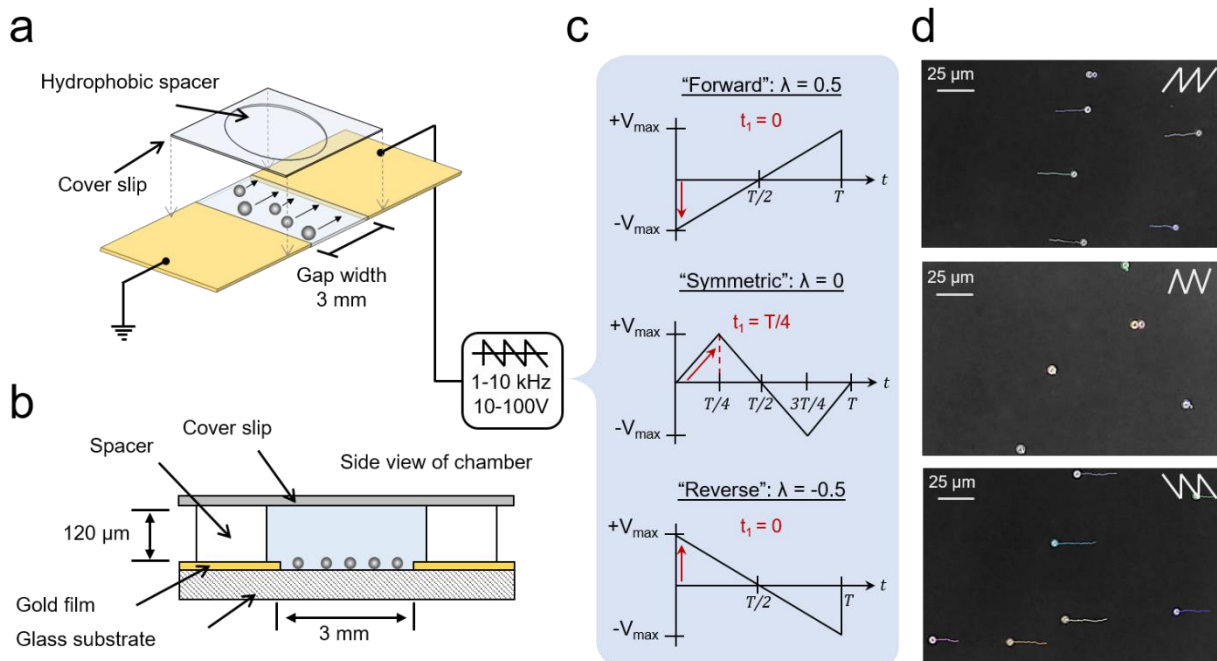


Figure 1: **a)** Top-down schematic and **b)** side view depicting the experimental cell with input ranges of asymmetric signal frequencies and voltages indicated. **c)** Main variations of asymmetric signal, characterized by an asymmetry parameter λ : A “forward” sawtooth signal is characterized by a gradual increase in voltage followed by a sharp drop, a “symmetric” signal is a symmetric triangular waveform, and a “reverse” sawtooth signal comprises a sharp increase followed by a gradual decay. All signals result in a net zero average potential. **d)** Experimental particle tracking screenshots showing tracked particle motion resulting from each corresponding signal over 45 seconds of exposure in DI water.

2.2 Materials and Methods

2.2.1 Preparation of electrodes and particles

The experimental chamber was composed of a standard glass slide onto which two parallel electrodes had been deposited by first evaporating 10 nm of Cr and then 100 nm of Au. Surfactant-free sulfate-modified polystyrene (PS) latex microspheres (Fisher) of three sizes - 1.8, 5.0, and 9.4 μm - were washed via centrifuging at 5000 g several times for 5 minutes each. Highly dilute suspensions of these latexes were prepared with ultrapure deionized water ($\sigma = 1 \mu\text{S}/\text{cm}$, $\text{pH} = 6.1$). The Ag-PMMA (Cospheric LLC) and metallodielectric particles were prepared in a similar fashion with the addition of 0.1 wt% Tween-20 (Sigma-Aldrich) to mitigate aggregation and

adsorption of particles to the electrode surface. In the case of electrolyte experiments, particles of all three sizes were washed three times and finally suspended in a 7×10^{-5} M KCl electrolyte solution ($12 \mu\text{S}/\text{cm}$, pH 5.5). In all cases, a 50- μl suspension of particles was placed into a 120- μm tall hydrophobic spacer (Fisher) on the glass slide. A coverslip was placed over the assembly to enclose the suspension in the form of a thin layer.

2.2.2 AC Signal and motion capture

The AC signals provided to the electrodes were generated by an Agilent 33120A 15 MHz function generator (Agilent Technologies, Inc.) connected to a TEGAM 2340/2350 High Voltage Amplifier (TEGAM, Inc). An AC ramp function was applied in the range of 1 kHz to 10 kHz and 30 to 300 V/cm in both “forward” and “reverse” directions (Figure 1). The voltage and frequency of the resulting signal were measured using an Agilent 34405A digital multimeter and Agilent DSO3202A oscilloscope. A 2 μF capacitor was connected in series in the circuit to remove any direct current component of the applied signal. Combined AFEP-ICEP experiments were conducted on 10 μm Au-PS Janus particles. The particles were exposed sequentially to AC waveforms in this order: square signal (300 V/cm, 1 kHz), forward sawtooth (216 V/cm, 4 kHz, $\lambda = 0.5$), square signal (300 V/cm, 1 kHz), and reverse sawtooth (216 V/cm, 4 kHz, $\lambda = -0.5$). Each signal was maintained for 15 seconds before switching to the next. Particle motion was observed and recorded using an Olympus BX-61 optical microscope. Primary objectives used were 20 \times and 50 \times . The motility measurements were performed in the central area of the experimental cell in order to avoid disturbances from dielectrophoretic, electrohydrodynamic and electrothermal effects that could emerge at the edges of the planar electrodes. Particle velocities were measured

by tracking particle trajectories with Fiji image processing software and the Mosaic Suite plugin [174], followed by processing in MATLAB.

2.3 Results

2.3.1 Velocity dependence on signal asymmetry

The particles subjected to a symmetric triangle signal showed little to no directional motion. That reveals that neither common DC electrophoresis (EP), nor AC dielectrophoresis (DEP) are significant phenomena driving particle motion, suggesting that the spatial electric field gradients in these cell conditions are negligible. Upon application of a temporally asymmetric “sawtooth” signal, the latex microspheres began to move in a direction colinear to the electric field. The direction of motion of the particles was reversed when the shape of the sawtooth was reversed. Full temporal asymmetry sweeps at fixed field strength and frequency revealed the symmetric velocity profile for 5.0 μm particles as the signal shifted from a forward-skewed sawtooth to a symmetric triangle and finally to a reverse-skewed sawtooth. The particles showed peak velocities at the extreme asymmetric sawtooth signal in either direction. These velocities decreased approximately linearly to a minimum at the symmetric signal case. Figure 2 shows the normalized experimental particle mobilities compared with theoretical and numerical results discussed in a later section. These findings are plotted against the signal asymmetry parameter λ , where -0.5 and 0.5 correspond to the reverse and forward sawtooth signals, respectively, and 0 represents a perfectly symmetric, triangular waveform. The experimental results thus obtained, are validated by an analytic solution obtained for the mobility (including reversal) of freely suspended dielectric particles (low-frequency range), obtained by means of a Laplace transform and considering the effects of surface conductance and concentration polarization under the assumption of a “weak”

field and thin EDL [175,176], as well as by axisymmetric 2D COMSOL simulations. Given that we identify the time-dependent asymmetric signal as the main origin of the bi-directional motility, we call this effect *Asymmetric Field Electrophoresis* (AFEP). The effect originates from dynamically induced local asymmetry of the ionic gradients on each individual particle, leading to subsequent motility, broadly similar to the ICEP effect, where the asymmetry is embedded in Janus particles. Thus, AFEP also fits to the definition of “active” or “self-propelling” particles [33].

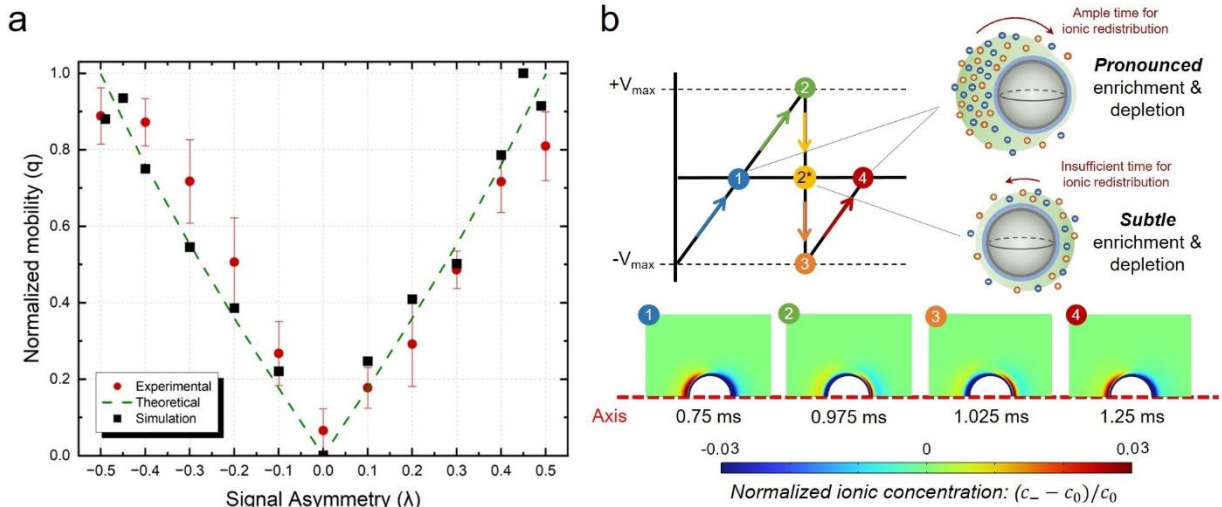


Figure 2: **a)** Normalized 5.0 μm particle absolute velocity data as a function of signal asymmetry at 2 kHz and 183.3 V/cm in DI water. Forward and reverse sawtooth signals correspond to λ of 0.5 and -0.5 and result in active motility in opposite directions. The data are presented as mean particle velocity ± 1 standard deviation (SD) ($n=122$). Mobility measurements show a good qualitative agreement with the theoretical model (see eq. 16 in Appendix B) and COMSOL numerical simulations. **b)** Illustrative snapshots from semi-qualitative axisymmetric 2D COMSOL simulations capturing time-dependent ion concentration corresponding to the phases (1-4) of the applied sawtooth signal ($\lambda = 0.4$, details in Appendix A). Most notable is the residual concentration polarization despite full reversal of the signal polarity. The particle-ion schematics in b depict the ion concentration gradient around the particle at the zero-voltage points (1, 2*, and 4).

2.3.2 Velocity dependence on field strength

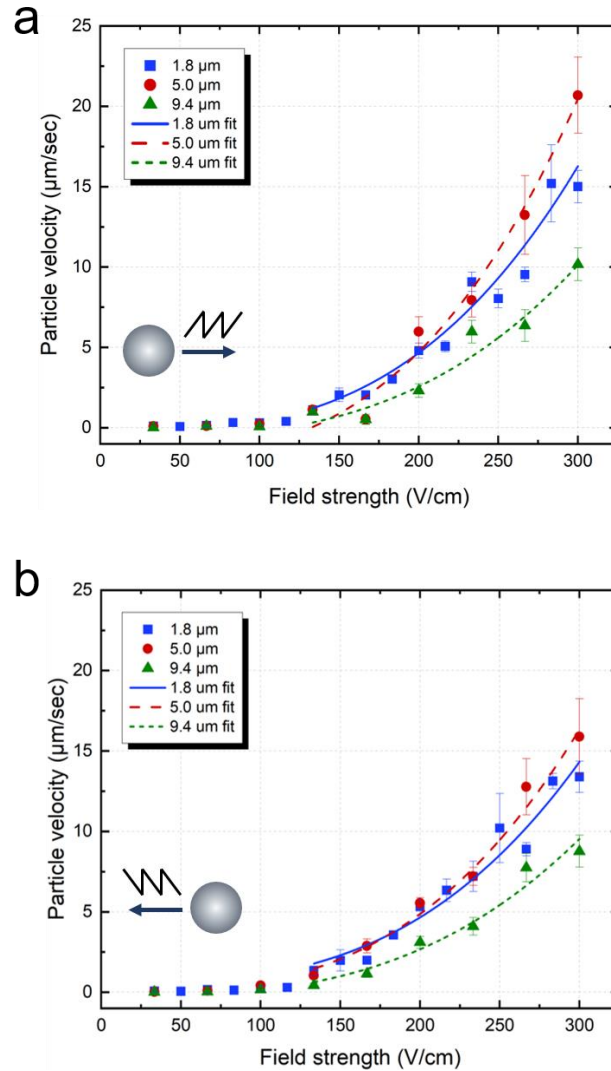


Figure 3: Particle velocity data were collected as function of field asymmetry, strength (30-300 V/cm), at 2 kHz in DI water. **a)** Forward velocity ($n=169, 133, 151$ for 1.8, 5.0, and 9.4 μm respectively). **b)** Reverse ($n=130, 146, 142$ for 1.8, 5.0, and 9.4 μm respectively) asymmetric AC signals with thresholded cubic fits. The motilities in both directions are similar in magnitude with a general inverted relationship between particle size and velocity. The data are presented as mean particle velocity ± 1 SD for each condition.

Interpreting the dependence of the microparticles' AFEP velocity and direction of motion on the electric field is key in understanding the physical mechanisms of their induced directional motility.

The correlation between particle size and velocity is also important in evaluating the ionic relaxation phenomena. A systematic voltage sweep in the range of 30–300 V/cm was performed

at 2 kHz on three sizes of latex spheres with both the forward and reverse AC ramp signals and as expected the velocity rapidly increases with the field. The data point to significant differences in the motility of particles based on size (Figure 3). Across field strength and high frequency conditions, a general inverted trend is observed between particle size and velocity, as the 9.4 μm particles move more slowly than the smaller particles. The difference in the velocity between 5.0 and 1.8 μm particles is less obvious.

The common expectation for the correlation between the field, E , and velocity, U for phoretic effects involving induced-charge motility is a quadratic relationship, $U_{ICEP} \propto E^2$ [2,177]. The E^2 dependence approximately describes the velocity data magnitude but predicts that the motility takes place only in one direction, as determined by e.g., the orientation of a Janus metallodielectric sphere [2], and hence does not explain the motility reversal. Further, when fitting the $U_{AFEP}(E)$ data with an E^2 dependence, we found that the fit is significantly worse than a fit of $U_{AFEP} \propto E^3$ dependence. Statistically, the cubic fit agrees well with the experimental data from all three sizes. A series of nonlinear curve fits was assessed on the field strength data for three particle sizes using OriginLab software. The table below contains the representative ANOVA test results for 5.0 μm spheres driven by an AC signal of 2 kHz under a ‘forward’ sawtooth ($\lambda=0.5$). Fits were evaluated on the overall balance between R^2 values, sum of residuals, and F and p values. The F value reflects the ratio of variance between groups to variance within the group. Practically, the larger the F value, the more likely that results are statistically significant and not simply a product of chance. Conversely, the p value represents the likelihood that a more extreme F value can be observed and supports the idea that results can be attributed to chance [178]. Greater weight was assigned to a model that showed both a high R^2 and F value and a low p value. In all cases, the null hypothesis was a zero value for at least one coefficient. Across the six fits that were tested,

the best R^2 values and lowest residual sums resulted from cubic, linear + cubic, linear + quadratic + cubic, and allometric models. However, the quality of F and p values for the former far exceeded those of the rest. Consequently, a cubic approximation was employed to analyze the field strength data.

Table 1: Table summarizing the fitting results determined by using OriginLab for six models that were applied to the field strength data.

Type of fit	Equation	R^2 value	Sum of residuals	F and p values (confidence 5%)
Quadratic	$U(E) = 1.963 \times 10^{-4} E^2$	0.86838	1054.45	F = 1418.08 p = 1.79×10^{-72}
Cubic	$U(E) = 7.334 \times 10^{-7} E^3$	0.95241	381.25	F = 4155.14 p = 1.21×10^{-101}
Linear + cubic	$U(E) = -0.01148E + 8.847 \times 10^{-7} E^3$	0.96479	282.09	F = 2809.64 p = 2.64×10^{-108}
Linear + quadratic + cubic	$U(E) = 0.007E - 1.906 \times 10^{-4} E^2 + 1.325 \times 10^{-6} E^3$	0.97859	265.16	F = 1980.24 p = 0
Allometric	$U(E) = 6.816 E^{3.828}$	0.96616	271.13	F = 2925.87 p = 1.97×10^{-109}
Thresholded linear (applied after 150 V/cm)	$U(E) = -18.53 + 0.1252 E$	0.90533	528.77	F = 784.136 p = 9.77×10^{-44}

The average particle velocities, standard error, and corresponding cubic fits under forward and reverse sawtooth signals are plotted in Figure 3. Due to very low particle mobility at small field strengths and possibly some degree of adhesion between the particles and substrate, the particle mobilities at low field strengths are below the range of reliable measurement, and the fits have been applied to data above a threshold of 133 V/cm, marking the first indication of directional motion.

2.3.3 Velocity dependence on signal frequency and particle separation

Finally, we examined how particle motility changes across a range of AC field signal frequency (denoted by f) at fixed field strength and asymmetry. When the measurements were performed within the intermediate to high frequency range between 1 kHz and 10 kHz, the particle velocities decayed steadily with increasing frequency (Figure 4a). Velocity data across all three particle sizes show a strong agreement with the theoretical prediction $U_{AFEP} \sim 1/\sqrt{f}$ of the asymmetric-mobility (see equation 15 in Appendix B), which is determined through the application of a Laplace transform to an asymmetric triangular AC signal by accounting for surface-conductance induced polarization. In comparison, for a typical ICEP process with a relaxation time associated with the formation of an induced-charge electric double layer (EDL) the frequency dispersion of the velocity (at moderately high frequencies) generally scales as $U_{ICEP} \sim 1/f^2$ [50].

One further parameter domain of unexpected particle behavior was revealed at low frequencies below 1 kHz (Figure 4c). First, we observed the existence of peak velocities at ≈ 250 Hz for the larger particles and ≈ 1 kHz for small particles, which is characteristic of most EHD effects when the period of the applied frequency becomes much larger relative to the relaxation time of the ionic charges around the particles, which cannot keep pace with the switching field polarity. Second, we observed an unexpected *size-dependent reversal of the direction of particle motion* in the 10-300 Hz range. Particles of 1.8, 5.0, and 9.4 μm reversed the direction of lateral movement at frequencies below approximately 250, 100, and 30 Hz, respectively (Figure 4c). As common for microparticles, the motility is driven by ionic migration, without particle inertial effects, as the Reynolds number, Re , is $\sim 10^{-8}$. The estimated ionic concentration polarization relaxation times were determined using the relation $\tau_{CP} = a^2/D$, where a is particle radius and D ($=5.3 \cdot 10^{-9} \text{ m}^2 \text{ s}^{-1}$ [179]) is the ion diffusivity. The resulting frequencies from this calculation are

~1041, 135, and 38 Hz for 1.8, 5.0, and 9.4 μm , respectively, which matches the general trend seen in Figure 4b and provides an accurate estimate for the larger particles. We hypothesize that the low-frequency reversal, which is broadly similar to “particle ratcheting,” originates from the imbalance between electrophoretic motion of the particles and the intermittent electroosmotic motion of the aqueous medium in the cell during the two phases of the sawtooth signal. Thus, the crossover results from the superposition of the “field-synchronous” ratcheting motion and dynamic AFEP at higher frequencies. Further investigation is necessary to determine the exact origin of this effect and the role of fluid flow, particle surface charge, and wall gradients. Electrode edge and wall conductivity effects have been reported as influencing other AC-EHD phenomena to various extents [2,52,166] and could also be a topic of more comprehensive future studies.

The low frequency experiments were also replicated using 7×10^{-5} M KCl [52] as the bulk solution due to the “ideal” symmetric nature of this electrolyte (Figure 4d). Previous studies of AC field-driven systems have reported the occurrence of EHD phenomena resulting from differential ionic diffusivity [180], which can be suppressed through the use of electrolytes with ions of equal mobility [169,170]. Velocities for all three sizes were markedly less than those measured for particles in DI water, presumably due to the smaller Dukhin number due to the increased KCl solution conductivity relative to that of DI water. However, the general trends remain, and a full direction reversal is observed. Larger particles (9.4 and 5.0 μm) exhibit reversal at slightly higher frequencies than the DI water case (50 and 200 Hz respectively), while 1.8 μm particles show reversal up to 1 kHz. It appears that the use of a symmetric electrolyte does not suppress the AFEP effect, which was present in all studied systems.

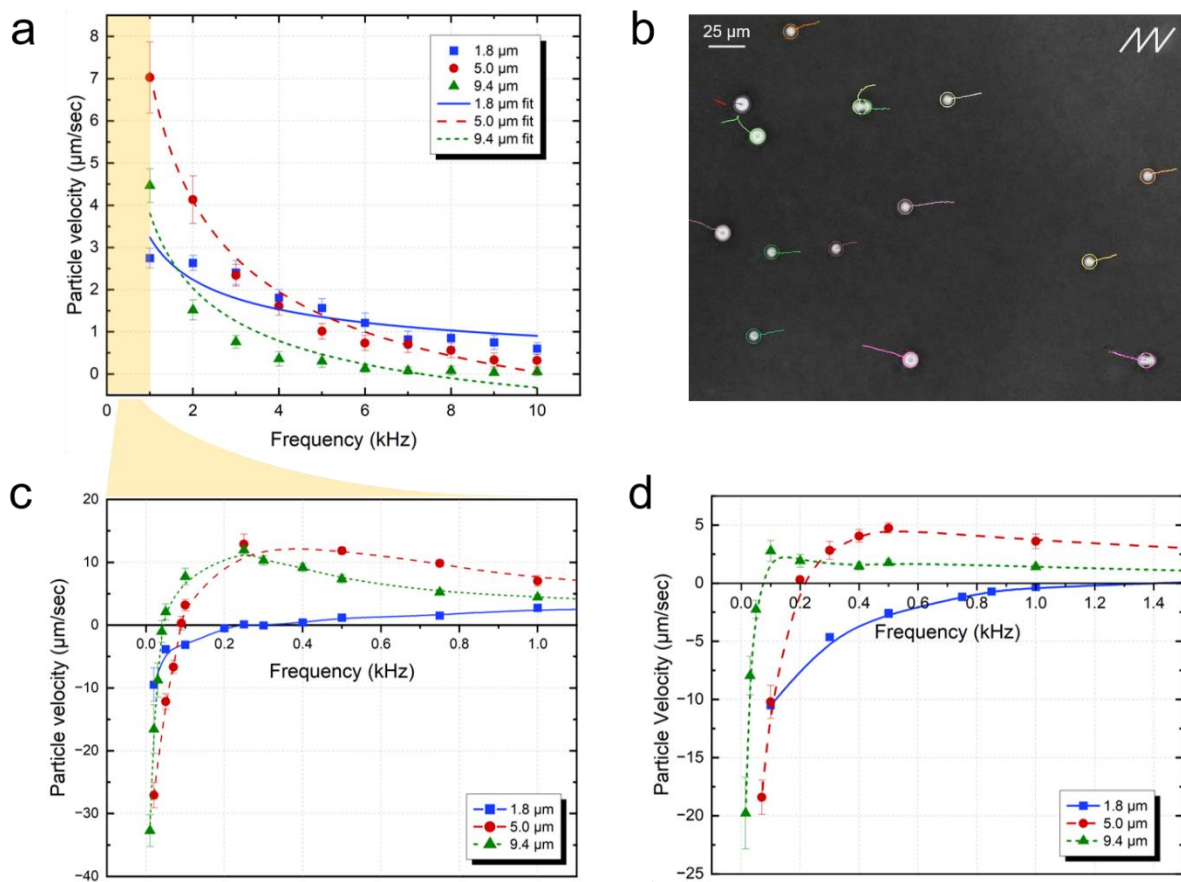


Figure 4: **a)** Combined forward and reverse particle velocity data for 1.8, 5.0, and 9.4 μm latex particles in DI water as a function of frequency (1-10 kHz) at 183.3 V/cm with fits of $1/\sqrt{f}$ ($n = 2\times$ for 142, 138, 192 for 1.8, 5.0, and 9.4 μm respectively). **b)** Experimental particle tracking screenshot showing 5.0 and 9.4 μm particles moving in opposite directions under a forward sawtooth signal of 50 Hz, 183.3 V/cm. **c)** Combined forward and reverse low frequency particle velocity data taken at 183.3 V/cm showing direction reversal (crossover) for 1.8, 5.0, and 9.4 μm latex particles below 250, 100, and 30 Hz, respectively ($n = 2\times$ for 100, 146, 112 for 1.8, 5.0, and 9.4 μm respectively). **d)** Combined forward and reverse particle velocity data for 1.8, 5.0, and 9.4 μm latex particles in the low frequency range with a bulk solution of 7×10^{-5} M KCl ($\sigma = 12$ μS/cm, pH = 5.5, $n = 2\times$ for 82, 77, 55 for 1.8, 5.0, and 9.4 μm respectively). Particles demonstrate direction reversal even with the use of this symmetric electrolyte. Curves in c and d were added to guide the eye. All data are presented as mean particle velocity ± 1 SD for each condition.

The existence of size-dependent crossover frequencies, where the particle motion changes its direction is an unusual and interesting finding that may be of large consequences with regards to development of processes for particle sorting and separation on a chip. The conventional particle separation by DC electrophoresis achieves separation based on surface charge. According to the

Helmholtz-Smoluchowski equation, the electrophoretic (EP) mobility μ of a particle is expressed as $\mu = ((\varepsilon \varepsilon_0)/\eta)\zeta$ [181], where ε is the relative permittivity of the suspending liquid, ε_0 is the electrical permittivity of vacuum, η is the dynamic viscosity of the liquid, and ζ is the zeta potential. Notably, μ does not depend on particle diameter. Further, the measured ζ for all three particle sizes showed minor variations and thus the EP velocity difference is unlikely to be the driving factor in separations. In addition, the emergence of electroosmotic flows in DC electrophoresis largely complicates the EP separations. Separations by particle polarization, which may depend on size, are possible by DEP, but this typically requires complex electrode configurations and microfluidic flow devices due to the limited DEP displacement resulting from its short-range application ($\sim r^{-3}$ [182], where r is the radial distance from the electrode's edge). In contrast, we found that the temporally asymmetric signal in AFEP can be used as a facile tool to separate particles on the basis of size without the use of microfluidic channels or sophisticated electrode designs. This possibility was demonstrated in experiments where samples of mixed 5.0 and 9.4 μm particles were separated by size by applying a signal at 60 Hz, such that the smaller particles were propelled to the left and the larger ones migrated to the right (Figure 5). The microscope images in Figure 5 show the experimental chamber before and after separation and the size distributions demonstrate near complete separation at opposite ends of the chamber. Notably, this new type of opposite motility separation could be much more efficient than conventional electrophoresis, where particles of similar charge move in one direction with different velocities.

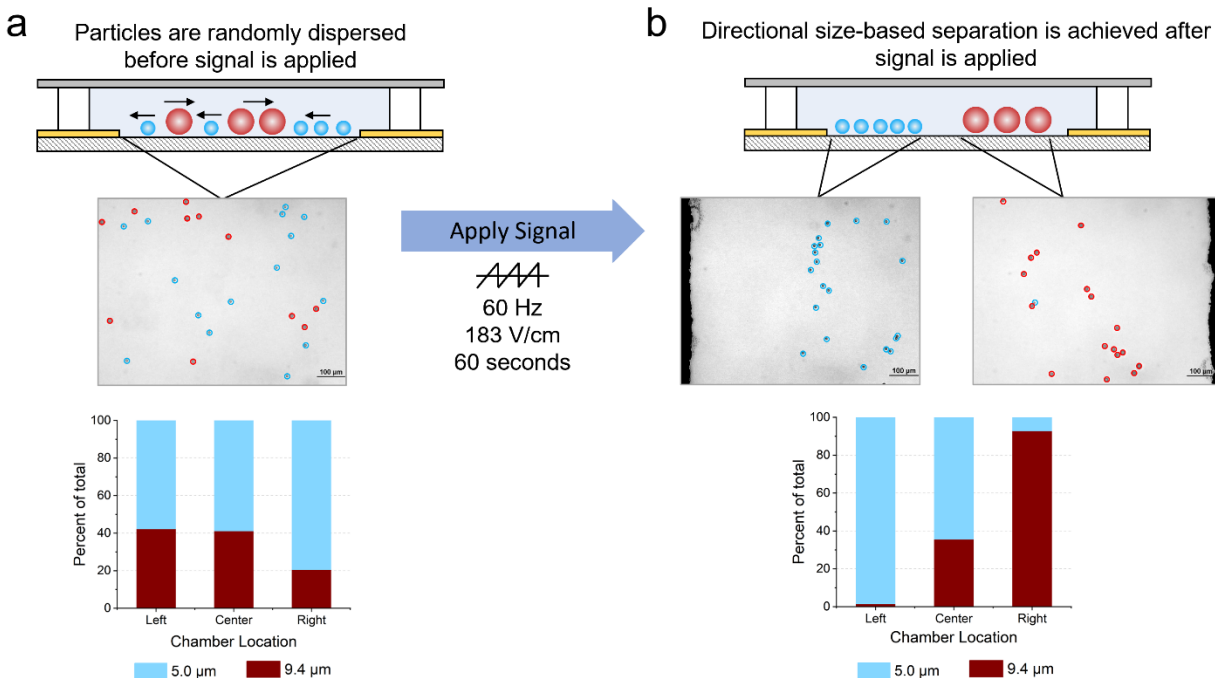


Figure 5: **a)** Schematics with marked locations of small and large particles before and after application of the signal, accompanied by micrographs. Large particles are driven to the right and small particles are driven to the left. **b)** Bar chart of measured 5.0 and 9.4 μm particle concentrations before and after application of the signal across three locations in the chamber. There is a distinct difference in particle distribution by size after the signal has been applied for only 60 seconds.

2.3.4 AFEP motility of metallic and metallodielectric particles

The AFEP effect seems to be universally present in any particle class in water. In addition to dielectric particles, we observed persistence of the AFEP effect with uniformly silver-coated poly(methyl methacrylate) (Ag-PMMA) microspheres. A suspension of Ag-PMMA particles was prepared with the addition of 0.1 wt% Tween-20 to prevent adsorption to the glass substrate. The sample was exposed to both forward and reverse ramp signals under a range of field strengths and frequencies. The Ag-PMMA particles responded to the field similarly to the dielectric particles, moving along the field lines and switching direction when the waveform was inverted (see Appendix C for velocity data). One notable difference, however, is the magnitude of the velocities measured between the samples. Under all conditions, Ag-PMMA beads moved at considerably

higher velocity despite being up to 4 times larger. This can be attributed in part to the higher polarizability and larger induced ionic charge on the metallic coating, which in turn may evoke stronger electro-convective flows [2,181]. Further investigation is needed to understand the effect of the critical field parameters on metallic particles under an asymmetric AC signal. It is likely that multiple types of remarkable AFEP phenomena will be observed in non-aqueous systems, however, given the complexity of the AC EHD effects in such systems, they are beyond the scope of this study.

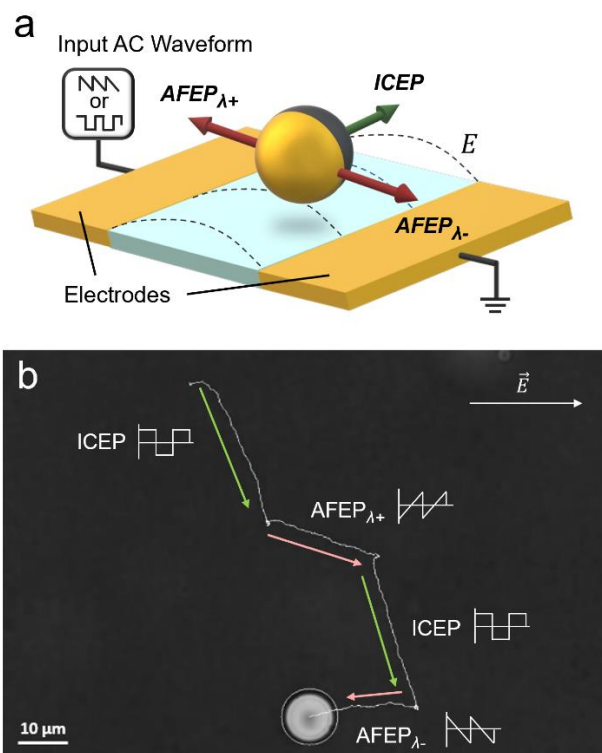


Figure 6: Independent driving of metallodielectric particle motility in two directions via the combined effects of AFEP and ICEP. **a)** A schematic summarizing the directions and origins of the multi-axial control. **b)** Particle tracking snapshot of experimental results using a $10 \mu m$ Au-PS Janus particle.

Finally, preliminary experiments were also conducted with the aim of evaluating the possibility of concurrently and independently powering particle mobility by combining

asymmetric and square AC signals, thereby combining AFEP with ICEP (Figure 6a). We used metallo-dielectric Au-coated polystyrene Janus particles to demonstrate the multi-axial control enabled by field signal encoding. The particles were sequentially exposed to alternating square and sawtooth signals for 15 seconds at a time. Notably, in this configuration the two effects lead to particle motility in two perpendicular directions (Figure 6b). The particles remained highly responsive to field changes without noticeable lag during the experiments. These results pave the way for additional exploration into the underlying effects driven by AC fields and boost the versatility of AC fields as a means of powering and multi-directionally controlling the motility of complex particles and microdevices in the future.

2.4 Discussion

2.4.1 Origins of polarization and motility

The system studied here is simple, strongly responsive, easy to implement and universal. However, very few investigations of such systems have been reported to date. A cubic relationship $U \propto E^3$ has been first suggested by Dukhin and coworkers who investigated the effects of *aperiodic* and *nonlinear electrophoresis* [183,184]. Many of the experiments associated with their work employed unbalanced pulsed square waves, in some cases at high field strengths [185–187]. Shibata et al. reported an experimental study where Au colloids and Si microrods exhibit bidirectional motion under a sawtooth AC signal [188]. Most recently, Hashemi et al. reported that an asymmetric AC waveform is inducing a net steady flow toward either the grounded or powered electrode which in turn results in net AC electrophoretic mobility [189]. Still, the physical origins and universality of particle motility via temporal asymmetry does not seem to have been reported earlier. It is tempting to suggest that the particle motion is a result of the

difference in time asymmetry as the signal switches polarity – that is, the field is changing slowly in one direction and rapidly in the other. However, as the time integrals (areas under the sawtooth waveform) are equal in both field directions, the motion of the particles cannot be a result from direct imbalance of the electrophoretic mobility. Instead, we hypothesize that this phenomenon originates from the dominating surface over bulk conductance (i.e., as described by the dimensionless Dukhin number $Du = K_S/\sigma a$ [190] relating surface conductance K_S and bulk σ conductivities, where a is the particle radius). For a typical surface conductance value of polystyrene beads $K_S \sim 1$ nS [191,192] and DI water conductivity $\sigma \sim 1$ μ S/cm [179], Du in the range of 2-10 is obtained for particle diameter of ~ 2 -10 μ m. This effect is maximal at the points at which the electric field is the strongest ($+V_{\max}$ and $-V_{\max}$ on Figure 1) because these peaks mark time points of discontinuity where the sawtooth waveform rapidly changes from a ramp function to a step function. The induced concentration-polarization ionic cloud oscillates through every successive half-cycle in response to the temporally changing field, with increased asymmetry following the asymmetric signal, thereby maintaining a preferential induced surface concentration gradient that favors one side of the particle. This redistribution of the ionic cloud as a response to the surface conductance induces an asymmetric concentration-polarization dipole across the particle, which interacts with the electric field. This drives directional motion to produce a secondary effect [2,168,186], manifesting as the field-colinear motion that we observe. The concentration polarization from this sudden change likely results in a skewed enrichment/depletion of the counterionic cloud around the particle, which has been recently shown to produce fluid flow as a result of surface conductance [176,193].

Due to the multiple sources of complexity in the diverse motile systems driven by AFEP (temporal asymmetry, wall effects, double layer mobilities and capacities, non-linear field

response), it is challenging to identify one sole electrokinetic mechanism as the dominant one. Statistical analysis of field strength data suggests a cubic dependence with increasing applied voltages, which may be attributed only in part to the Stotz-Wien effect, which is most commonly observed at high field strengths (generally considered as 10^6 - 10^7 V/cm for 1-10 mM electrolyte concentration – outside of the parameter space of this study) [181,186].

2.4.2 Numerical correlation of motility to field parameters

The precise interpretation for the experimentally found $U \propto E^3$ dependence, is generally associated with the effect of surface conductance (finite Dukhin number) [185] and will require further theoretical advances. However, under the assumption of a small Peclet number, it is relatively straightforward to apply a linearized theory to derive a simple scaling relationship that describes the particle mobility as a function of the asymmetry parameter λ by taking the Laplace transform of a triangular wave and treating the transient flow problem following the time-dependent concentration polarization electro-osmosis (CPEO) formulation by Calero et al. [193]. We introduce a simplified linear relationship between the normalized particle mobility q , and the asymmetry parameter λ , $q(\lambda) = \pm 2\lambda$, where the parameter λ can vary between 0 (symmetric triangular waveform) and $\frac{1}{2}$ (extreme sawtooth). The \pm signs stand for the forward and reverse direction of the signal, respectively, as depicted in Figure 1. It could be expected that the mobility will be suppressed ($q = 0$) for systems with particle zeta potential $\zeta = 0$, however such aqueous systems are encountered rarely only at isoelectric point conditions. A complete derivation of the resulting expression can be found in Appendix B. The model shows excellent agreement with the experimental data.

A qualitative two-dimensional axisymmetric COMSOL simulation was also conducted for a charged dielectric cylinder in a time-varying field via the solution of the fully coupled Poisson equation for the electric potential, Nernst–Planck and continuity of ions equations for the ion fluxes and concentrations, and the Stokes equations for fluid flow (for more details on the numerical simulations and theoretical model see Appendix A and B, respectively). The results shown in Figure 2 indicate the formation of ionic concentration-polarization layer around the particle due to its dominating surface conductance as well as the residual concentration-polarization upon the step-wise change of the electric field which in turn results in non-zero time-averaged mobility upon signal asymmetry as seen in Figure 2a. Essentially, for applied frequencies larger than that corresponding to the relaxation time (τ_{CP} as described below) of the ionic concentration process, a residual ionic concentration-polarization exists within a period of the applied electric field and biased in the direction of the electric field immediately following the step function.

2.5 Conclusions

We have demonstrated that temporally asymmetric AC electric signals can serve as a means of inducing electrohydrodynamic motility of particles in aqueous medium, by an asymmetric field electrophoresis. The “pervasive” newly recognized AFEP effect is universally encountered with any dielectric particle type and operates across a large range of frequencies and particle sizes. The direction of motion is completely reversible with the degree of temporal asymmetry of the signal and thus can be precisely controlled by electronically programming the signal shape. The particle-centric (active) propulsion is driven by a secondary interaction between the electric field and asymmetric concentration-polarization dipole induced across the particle by the asymmetric

waveform signal. We characterized the particle behavior as a function of field strength, frequency, and signal asymmetry. Interestingly, an uncommon cubic relation was found to best fit the velocity dependency on the electric field, while an inverse dependency on the squared frequency was found. Further, we found that at low frequencies (<500 Hz), the particles undergo a reversal of motion at a size-dependent crossover frequency. We show that this reversal can be used to simply and efficiently separate particles on the basis of their size, obviating the need for complex microfluidic chambers or electrode designs.

To our knowledge, this is the first investigation characterizing the behavior of particles with respect to the degree of an AC- field time-based asymmetry and a frequency range including size-dependent crossover. It shows that this type of motility is operating on any type of microparticles as a result of the local ionic concentration-polarization and particle-centered dissipative flows. In contrast to other AC field-driven active particle systems, which require particles with special characteristics [2,27,30,48,49,63,107,167], AFEP can be induced in any particle. The universally encountered motility driven by particle-centric ionic gradients is in correspondence with the definition of “active” or “self-propelling” systems. Thus, we envision that this pervasive effect could add to the toolbox of AC EHD effects, by enabling another convenient way to control and manipulate an extremely broad range of AC field-driven active particle systems including future autonomous devices and microbots. Notably, the AFEP propulsion can be independently controlled and combined with previously reported sources of motility such as ICEP and AC dielectrophoresis for driving of more complex metallodielectric, shape-engineered and microcircuit-containing devices.

CHAPTER 3

Superdiffusive pellet from active particles driven by collective effervescent phenomena

3.1 Introduction

The rapidly developing and evolving field of active particles has been a subject of intense interest in the last two decades. A broad circle of researchers have designed and reported a number of intriguing engineered particles within the chemically driven active particle (CDAP) space [72,139,153,194,195]. At its core, an active particle is propelled by the breaking of symmetry on the particle level, which leads to localized chemical potential gradients [33]. CDAPs generally break symmetry through particle shape, coating, or material composition to induce selective reactive change of the chemical potential at the individual particle level [130]. One very common means of initiating active particle propulsion is the catalytic conversion of hydrogen peroxide medium using platinum, titania, or silver [34,101,141,145,196]. Another popular active motility method is using bubble-propelled magnesium particles in water [75,95,122,142].

Recent years have seen an increase in the complexity of particle composition and fabrication techniques in an effort to introduce more diverse and creative methods of symmetry breaking. Metal-based CDAPs are often fabricated through electroplating [145], photolithography [140], atomic layer deposition [139], or physical vapor deposition [72], sometimes requiring multiple iterations to manufacture the finished product [121,159]. Magnesium particles may require addition or removal of a passivation layer to ensure correct timing of the reaction [75]. Some particles with patches undergo a series of chemical treatments to be manufactured in their final form [165]. In many cases, the increased complexity can imply an increase in the cost of the active particle system.

Here we introduce a novel, ultra-simple active particle system composed of salt and acid particles that harnesses an acid-base reaction to drive collective rapid radial dispersal of the particles contained in a pellet once they get in contact with water. The particle body serves as the

“fuel” and the motility of the particles continues until their complete dissolution, leaving no trace behind. The acid particles used are also surface-active, further enhancing the speed and extent of dispersal. These effects result in its spreading and penetration at a rate that is much faster than the diffusion rate of immobile constitutive particles alone. Thus, we call the resulting millimeter-scale tablet “superdiffusive pellet”. In the following sections, we present our findings on the collective motility and behavior of this simple, cost-effective active particle system.

We conducted a systematic study of single- and bi-component superdiffusive pellets in acid, base, and pure water bulk conditions. Area coverage was measured to investigate the transition between surface and bulk activity and better understand the role of pellet and bulk composition on the rate of spreading. Two polyprotic surface-active acids were used in varying ratios to identify an optimal composition for bi-component pellets. We present our experimental findings accompanied by simple scaling relationships to describe the main mechanisms governing propulsion of the superdiffusive pellet particles. Finally, we discuss the potential for our active particle system to be employed in biomedical applications for disinfection.

3.2 Materials and Methods

3.2.1 Particle and solution preparation

The superdiffusive pellets were prepared using native ammonium bicarbonate (AB), citric acid (CA), and succinic acid (SA) crystals (Fisher) in the range of 300-500 μm . A small amount of fluorescein isothiocyanate (FITC) dye was dissolved into saturated solutions of each compound. The particles were coated with a few drops of the respective saturated solution and left to dry overnight (Figure 1a). The FITC-coated particles were then uniformly redispersed and stored with desiccant. Single-component pellets were prepared by mixing either AB or CA with 18% w/w

microcrystalline cellulose (MCC) (Fisher) as a binder. Two-component pellets were prepared using various ratios of AB:CA or AB:SA with the addition of 22% w/w MCC. A 0.02 g sample of the final formulation was loaded into a 3-mm diameter die and punch (Figure 1b). Each pellet was compressed with a 10-lb weight for 60 seconds before being released from the press.

3.2.2 Experimental set up

The experimental cell was composed of an open 47-mm diameter Petri dish (Fisher). The three main systems that were investigated are shown in Figure 1. They include an acid pellet dispensed into base bulk solution, base pellet dispensed into acid bulk solution, and mixed acid-base pellet dispensed into pure water (Figure 1c). AB and CA solutions were prepared in six concentrations (0.01, 0.03, 0.05, 0.07, 0.1, and 1 M) and 5 ml were dispensed for each experiment. All experiments were performed at room temperature (20°C). Videos of the dynamics of pellet dispersal were recorded using a Google Pixel 6a camera in a black photo box with a 365-nm UV light (Alonefire SV003) for visualization of FITC release. Surface area coverage was measured manually through frame-by-frame image analysis.

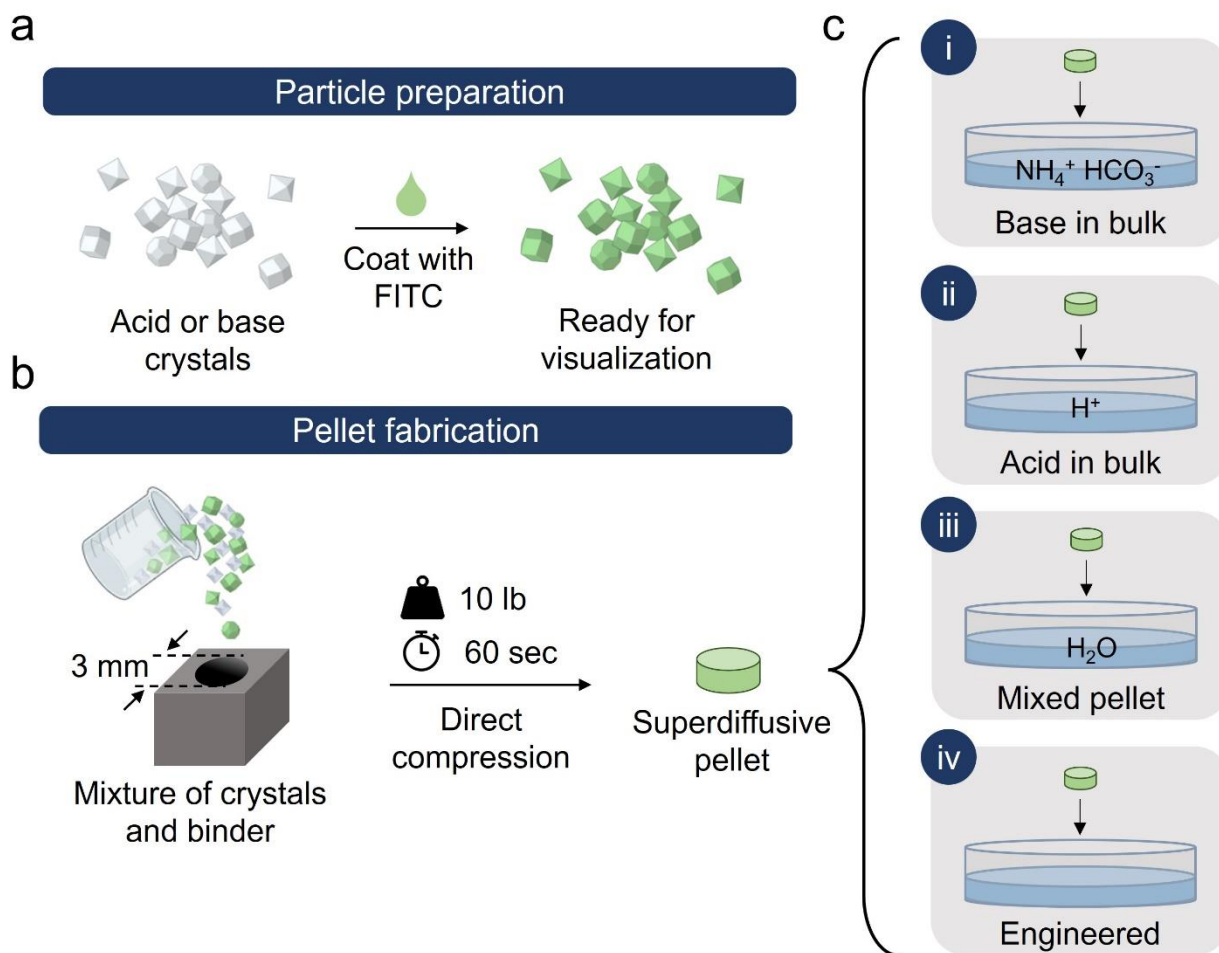


Figure 1: Schematic outlining the experimental set up and systems studied. **a)** Particles are prepared for visualization by mixing them with a FITC solution. **b)** Pellets are fabricated by loading the FITC-coated particles into a die and punch and compressing the assembly under 10 lb for 60 seconds. **c)** Three systems were investigated in this study: (i) acid pellet dispensed into base bulk solution, (ii) base pellet dispensed into acid bulk solution, and (iii) mixed acid-base pellet dispensed into pure water. Case (iv) represents the opportunity to build additional functionality and complexity into our versatile system.

3.3 Results

3.3.1 Spreading behavior of a single-component pellet

Two single-component pellets of AB and CA were tested in bulk solutions of the other counterpart (i.e., AB pellet in CA solution and vice-versa) to assess the rate and degree of solute coverage as well as the role of phase (solid or liquid) on dispersal of the pellet. AB and CA pellets were dispensed individually into 6 concentrations of CA and AB solutions, respectively, as well as DI

water. Figure 2 shows the rate of percent area coverage of the experimental cell accompanied by image snapshots for both systems. Upon contact with the bulk solution, AB and CA pellets demonstrated three general dispersing patterns: surface spreading, bulk activity, and bubbling. CA pellets primarily followed the surface spreading pattern, ejecting a few small particles at low bulk concentrations and generating spiraling, surface-level advective flows of dissolved CA and FITC. Liberated particles appeared to “dance” on the surface of the surrounding liquid.

The diameter of these flows and number of propelling particles increased significantly with the increasing concentration of bulk AB solution. At concentrations of 0.07 M AB and above, CA pellets exhibited bulk activity through rapid expansion and reaction with the surrounding medium, ejecting fragments and individual particles upwards and outwards to the perimeter of the dish where they disintegrated quickly. From 0.05 M to 0.1 M AB, CA pellets left behind a small number of bubbles adhered to the Petri dish after dissolving completely.

AB pellets appeared to demonstrate bulk activity at all concentrations of the bulk CA solution. At low molarities of CA, AB pellets swelled slowly but steadily until the AB particles had been loosened from the pellet body. No surface flows were observed to emanate from the pellet under any condition. At higher bulk CA concentrations, AB particles spread much further than at lower concentrations, but were quickly consumed below the surface of the surrounding liquid and converted to a large number of bubbles. For both AB and CA pellets, abundant foaming was seen at the 1 M bulk solution condition. Both system composition variations were generally fast-acting and steady-state behavior was observable within 2-3 seconds of contact between the pellet and bulk solution. CA pellets dispensed into AB solution demonstrated rapid surface coverage, reaching an average of 35% even in the lowest three concentrations of AB solutions, and attaining a maximum of roughly 86% at 0.1 M AB. Although strong advective flows were

observed around the perimeter of the expanding front, the CA pellets remained largely intact in the low concentration range.

Conversely, AB pellets began to swell and react with the CA solution almost immediately, but the dissolving material released by them spread relatively slowly within the first 3 seconds, reaching a maximum coverage of only 26% at 0.01M CA. A significant amount of bubble generation was seen at 0.03 M CA and above. In both cases, surface coverage was substantially higher in 1 M bulk solution, with the CA and AB pellets reaching over 92% and 81% of the vessel area, respectively, presumably due to the vigor of the acid-base reaction at this high concentration.

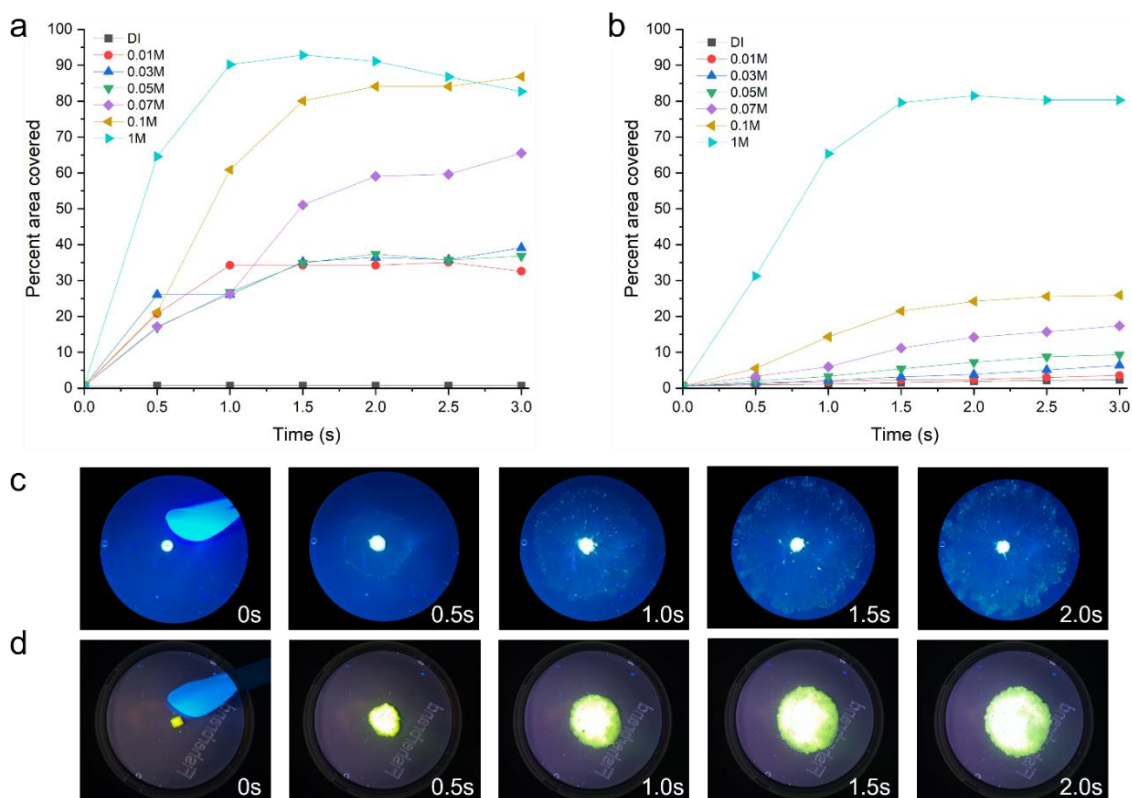


Figure 2: Area coverage data were collected for two systems: (a) CA pellet dispensed in AB solution and (b) AB pellet dispensed into CA solution at varying solution concentrations over a 3-second period. Snapshots in (c) and (d) show the progression of spreading of CA in 0.1 M AB and AB in 0.1 M CA, respectively. The surface-active nature of the CA in the pellet drives Marangoni flows throughout the cell, enhancing the speed with which the solute front reaches the extents of dish, even at lower bulk AB concentrations.

3.3.2 Surface vs bulk activity

To better elucidate the transition between surface and bulk activity, we measured the expansion and disintegration of the CA bolus across the seven conditions shown in Figure 2a. Upon introduction to the bulk solution, all CA pellets undergo an initial surface-active period during which a corona of FITC forms and spreads radially around the pellet. Figure 3 shows the swelling and disintegration data for CA pellets as a function of bulk AB concentration. Between 0.01 and 0.05 M AB, CA pellets exhibit some swelling from liquid entering the pores of the pellets. However, due to the low molar strength of the surrounding reactant, the CA pellet does not undergo intense reaction, and instead we observe a continuous stream of gently dissolving CA and FITC circulating away from the bolus for the entirety of the measuring period. Cross-referencing data from Figure 3 with that in Figure 2a shows that in most cases, the timescale of surface area coverage is 3-5 times faster than that of CA pellet disintegration, which suggests that the impressive coverage seen for 0.01 – 0.05 M AB in Figure 2a arises from the *surface* activity of the pellet, and not the *bulk* activity. Significant pellet expansion is seen over the first 6 seconds for the 0.05 M AB condition, which can be attributed to increased internal pressure from liquid seeping in and reacting to produce gas at the pellet's center. After this point, the increased surface area of contact between CA and AB drives steady consumption of the CA pellet through the acid-base reaction.

At concentrations above 0.05 M AB, this surface-active period lasts for a very short time before spreading is dominated by the vigorous bulk reaction activity and gas production. The magnitude of the reaction overwhelms the system and particles are propelled towards the perimeter of the dish at a much faster rate than what is observed when only surface flows dominate. Measured pellet area data in Figure 3 serves to help identify the threshold at which bulk reactivity begins to

dominate in the CA pellet case. This is not the case for AB pellets dispensed into CA solution, as AB pellets begin reacting and dissolving into the expanding front almost immediately. There is no observable period during which the AB pellet remains intact while particles or dye are circulated outward radially. It is important to note that at low solution concentrations, the timescale to reach bulk reactivity in this system is at least an order of magnitude higher than that of surface activity, suggesting that a pellet composed of both salt and acid particles in the right ratio can minimize the time required to achieve maximum coverage of the cell.

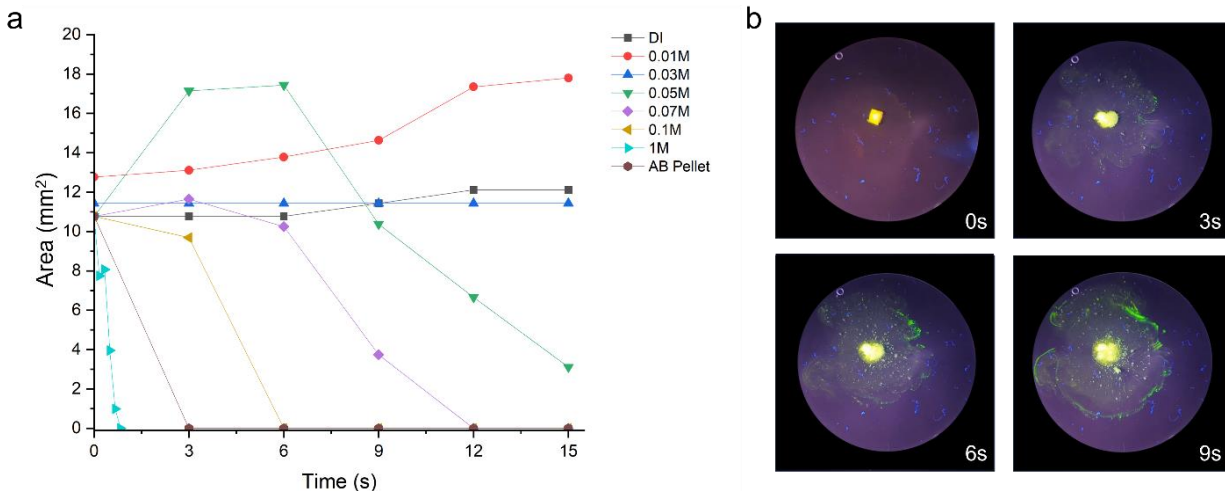


Figure 3: **a)** Solute front spreading data for CA pellet dispensed into AB solution for a range of concentrations. At low concentrations of AB, the CA pellet expands very slightly but remains whole. At 0.05 M AB and higher, the CA pellet first expands before rapidly disintegrating and becoming consumed by the reaction. For all AB pellet experiments, the pellet was immediately consumed and converted into the expanding front. **b)** Snapshots of a CA pellet in 0.05 M AB expanding and reacting over 9 seconds.

3.3.3 Spreading behavior of a mixed-component pellet

Two sets of mixed-component pellets were prepared for three molar ratios each of AB:CA and AB:SA. Each pellet was introduced into pure water and the resulting spreading data are summarized in Figure 4, accompanied by snapshots of 1:1 AB:CA and 1:1 AB:SA taken periodically over two seconds after pellet introduction. All mixed-component systems reached full

surface coverage within 3 seconds, far surpassing single-component pellet systems in spreading speed and degree. For both AB:CA and AB:SA, the most efficient ratio was 1:1 and by comparison, the slowest were the stoichiometric ratios (3:1 AB:CA and 2:1 AB:SA). This is likely because the chemical potential within the pellet in the latter case was very high, allowing the reaction to run to completion internally. Although the substantial bulk activity maintains relatively localized to the original pellet location, the combination of bulk-reacting and surface-active components allows for swift coverage of the entire cell at appr. $870 \text{ mm}^2/\text{s}$.

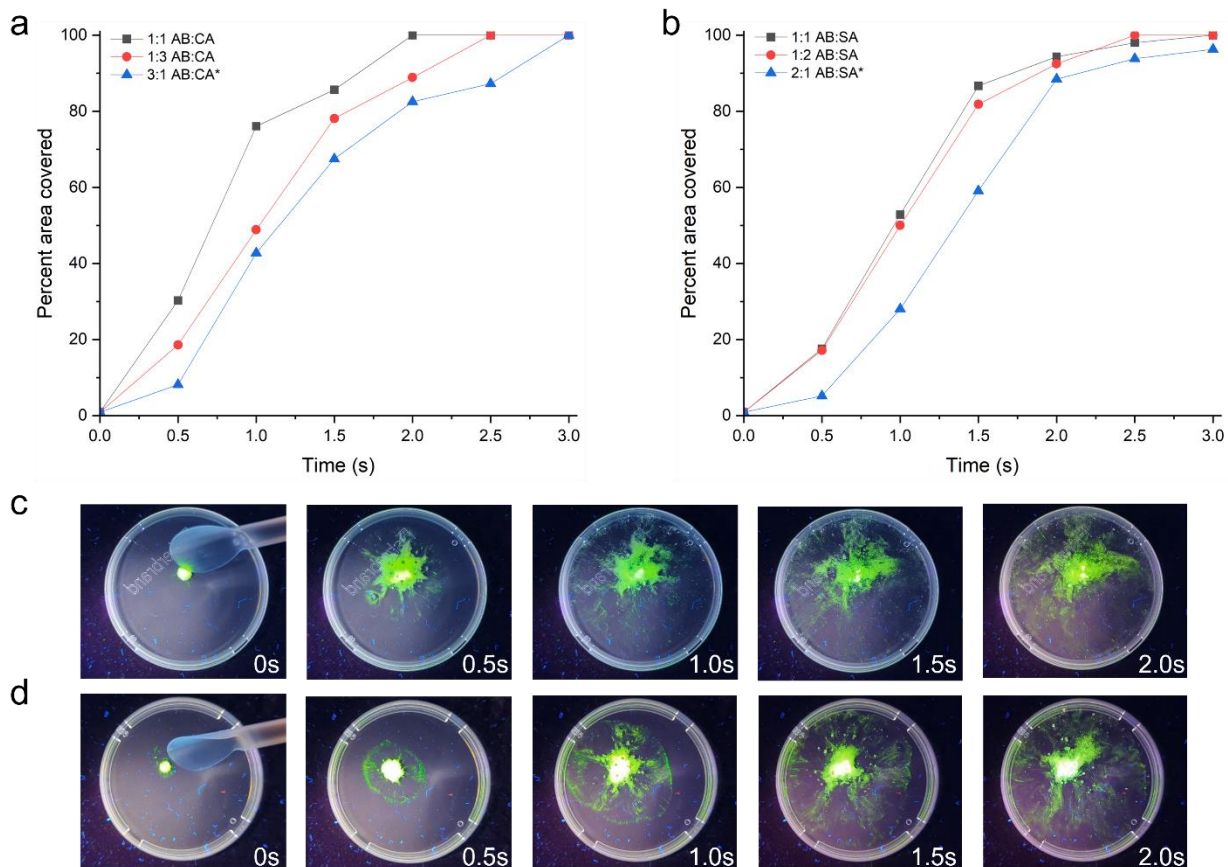
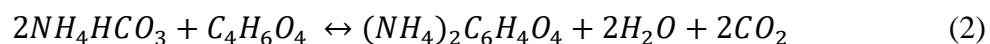
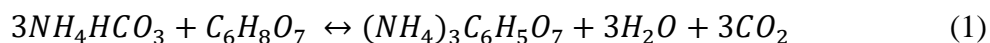


Figure 4: Area coverage data collected for two mixed-pellet systems dispensed into pure water: (a) AB-CA pellet at molar ratios of 1:1, 1:3, and 3:1 (stoichiometric ratio) and (b) AB-SA pellet at molar ratios of 1:1, 1:2, and 2:1 (*stoichiometric ratio) over a 3-second period. Snapshots in (c) and (d) show the progression of spreading for 1:1 AB:CA and 1:1 AB:SA, respectively. Although the highest concentration of material remains partially localized, FITC dye is seen at the perimeter of the dish as quickly as 2 seconds after the pellet is dispensed.

3.4 Discussion

3.4.1 Mechanisms driving collective particle propulsion

Propulsion of acid and salt particles in this system can be attributed to multiple mechanisms due to the complexity of the intraparticle and particle-fluid interactions (Figure 5b). AB readily reacts with CA and SA through a gas-producing neutralization reaction, commonly known as effervescence [197,198]. The reaction products can be generally predicted using the following reaction schemes:



CA and SA are both weak acids, with CA donating three protons ($pK_{a1} = 3.15$, $pK_{a2} = 4.78$, and $pK_{a3} = 6.40$ [199]) and SA donating two ($pK_{a1} = 4.61$ and $pK_{a2} = 5.61$ [200]). The bicarbonate ions from AB are converted to CO_2 . At high molar concentrations of AB, the acid-base reactions result in a very vigorous “explosive” production of CO_2 , rapidly driving up pressure within the superdiffusive pellet and propelling the constituting particles radially outward. For CA bulk concentrations of 0.05 M and higher, the AB pellet is converted almost immediately into a foam. Although bubble propulsion is a widely used mechanism for many chemically driven active particles [95,122,142], intense bubble production, and subsequent bubble nucleation and growth on the Petri dish, hinder propulsion of the breakout particles in this system. At this stage, mass transport of reactants and products is primarily dependent on molecular diffusion of the solutes around the particles, which is insufficient to create large enough tangential gradients to maintain motility.

Spreading of the superdiffusive pellet is also strongly influenced by Marangoni flows arising from the surface-active nature of CA and SA. The presence of dissolved CA and SA reduces the surface tension of the surrounding liquid, leading to an asymmetry in surface tension tangential around each particle or pellet fragment. As each particle is of a different shape, the dissolution pattern is inherently unbalanced. This change in the local surface tension leads to interfacial fluid flow towards areas of higher surface tension, which is known as the “Marangoni effect” [147,201–203]. The surface tension gradient is amplified by the clustering of CA or SA particles in the pellet; the area of lowest surface tension is directly above the pellet and strong flows towards the outside propel the individual particles outward (Figure 5a, (iii)). Figure 5c shows reported surface tension values of CA and SA as a function of concentration [204]. Overall, the change in the surface tension of water caused by CA and SA is small compared to that of traditional surfactants, ranging from appr. 2 to 6 mNm^{-1} . Since the pellets are composed of pure CA and SA crystals, the local concentrations around partially dissolved particles would be very high, suggesting that the surface tension change would also be at the higher end of the reported range. This can help explain the trend seen in Figure 1, in which CA pellets spread consistently more than AB even under low bulk molarity conditions.

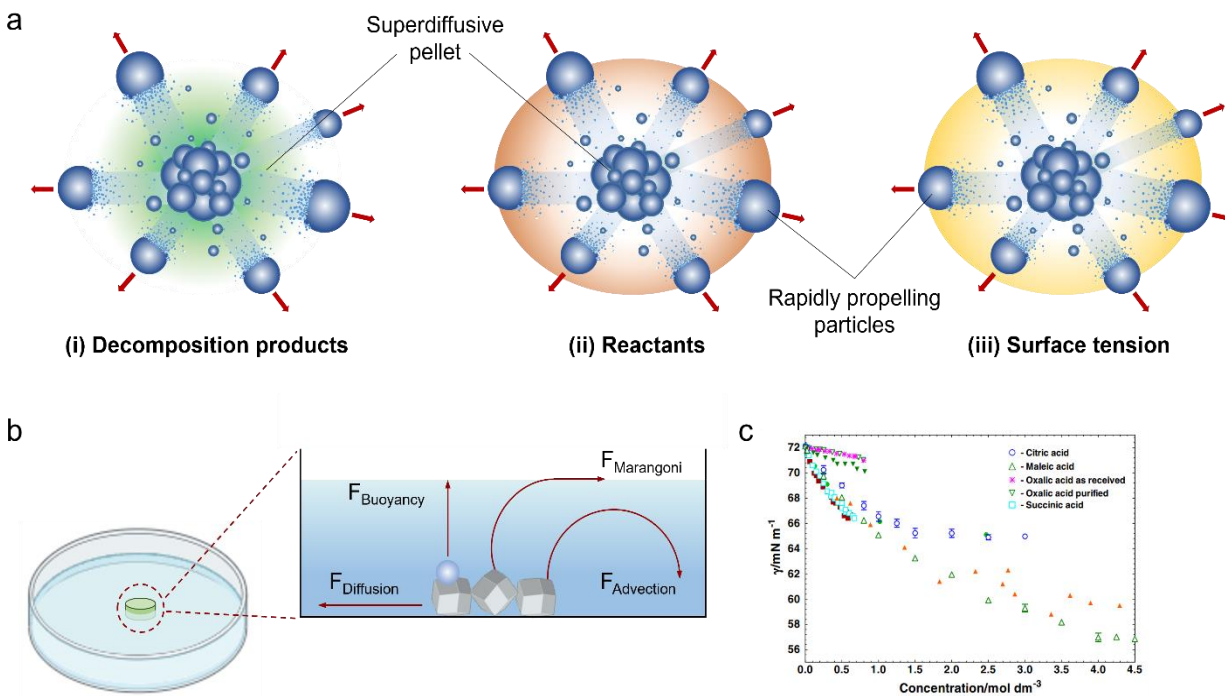


Figure 5: Mechanisms of superdiffusive pellet dispersion. **a)** Illustrations of the rapid radial propulsion of constituent particles in the superdiffusive pellet. (i) Pressure from the expanding osmotic gradient of decomposition products helps propel the particles further outward. (ii) Consumption of reactants at the center of the bolus drives a concentration gradient outward. (iii) Surface tension reduction by CA or SA particles produces a strong surface tension gradient radiating outward from the pellet. Particles are propelled outward by the Marangoni effect. **b)** Schematic outlining the four main forces acting on salt and acid particles as they contact the bulk solution. **c)** Reported surface tension data from measurements of four surface-active organic acids as a function of concentration [204]. CA (open blue circles) and SA (open cyan squares) both show a significant drop in surface tension.

There are several possible mechanisms explaining this self-dispersion behavior, which are summarized in Figure 5b. The first is a basic interpretation of the reaction kinetics from (1). For every mole of CA, 3 moles of AB are required to carry the reaction to completion. In the case of a CA pellet dispensed into AB solution, the CA particles rapidly consume the surrounding AB. The excess CA moves away from the high concentration of decomposition products (Figure 5a (i and ii)) towards the source of unreacted AB, i.e., outwards. As the reaction takes place at higher concentrations of both reactants, vigorous advective flows are generated around the cell. These dissipative flows appear to be correlated to the force and speed with which gas is expelled from

the bolus, serving not only to expand the pellet and increase access to reaction sites, but also to circulate fluid in the vessel and transport dye along with reaction products.

Concurrently with gas release, the contact between CA particles and the surrounding water drives asymmetric surface tension gradients around the particle body, which is already nonuniform in its native form. Marangoni flows, which are generated as a result of localized surface tension gradients, have been reported to induce self-propulsion in droplets [127,129,148,149], particles near a bubble [146], and even millimeter-scale gel boats [128]. Asymmetry along an air-solution interface pushes the particle towards areas of higher surface tension and drives propulsion as long as the particle continues to release the surface-active solute and the surface has not been saturated. For a surfactant driven system, the ratio of the driving solute gradient to the viscous friction force can be expressed through the following dimensionless quantity, termed the *Marangoni number* [147]:

$$Ma = \frac{\alpha AR}{\mu D^2} \quad (3)$$

where α is the rate of reduction of interfacial tension, A is the emission rate of surfactant, R is the radius of the particle, μ is the viscosity of the medium, and D is the diffusivity of the surfactant. For a single-particle system, a high rate of surfactant emission coupled with a high rate of interfacial tension reduction will comprise the dominating mechanism of propulsion. For many-particle systems in which the particles operate within a close vicinity to each other, Marangoni flows can lead to a repulsive effect in which high surface tension regions between particles push them away from each other [147].

This phenomenon supports the notion that the high concentration of CA in the form of particles in the pellet further results in the generation of a strong interfacial tension gradient at the center of the bolus, causing the particles to propel outward. Finally, as mentioned above, gas production causes the formation of visible bubbles in the cell. While the bubbles seem to cluster primarily on the surface of the dish, it is possible that a fraction of the much smaller bubbles attach to CA particles and assist them in traveling outward and upwards. As each particle of CA contains its own asymmetry in shape and size, the dominant mechanism, and thereby the localized gradient, may vary from one particle to the next. This synergistic combination of effects results in a simple superdiffusive pellet with significantly enhanced ability to spread across a large area in a matter of seconds.

Microcrystalline cellulose (MCC) could be used in this system as an inert dry binding agent with the additional benefit of lubrication in the tableting die. MCC is commonly used as a pharmaceutical excipient in the direct compression of tablets due to its excellent properties as a diluent, lubricant, and glidant while also exhibiting plastic deformation under stress [205–207]. In our system, MCC serves also to absorb excess moisture during mixture preparation and prevents the premature reaction of bi-component pellets. MCC provides another notable benefit during tablet manufacturing: improved disintegration. Owing to its high intraparticle porosity, MCC promotes swelling of the tablet through enhanced water permeation into the inner matrix [206]. This behavior can facilitate the timely dispersion of therapeutic agents in rapid-release formulations. A 2015 study examined the swelling and disintegration patterns of pure MCC tablets by varying tablet porosity and bulk water temperature [208]. Tablets with porosities of 10% and 15% swelled by 0.5 to 1 mm within the first 15 seconds of immersion in water. The rate of expansion increased with increasing water temperature.

Although MCC demonstrates enhanced transport of bulk solvent into the tablet matrix, the magnitude of its role in the spreading of our superdiffusive pellet is unclear. Tablets used in the study were thinner and much wider (1.5×10 mm) than ours, which would increase the available surface area of contact between the pellet and bulk liquid. In addition, the tablets were formulated at 100%, 98%, and 95% wt MCC compared to 18% used in our system. Tablets at 40% porosity fractured and disintegrated within 15 seconds, while those at 15%, 10%, and 5% porosity did not disintegrate at all. The timescale of disintegration for the 40% porosity case overlaps with that of the pellet expansion data in Figure 3, suggesting that the contribution from MCC is primarily in facilitating access to reaction sites within the pellet body. However, advection from gas production and surface activity from Marangoni flows dominate the overall rate of spreading. Further investigation into pellet porosity and excipient formulation is necessary to determine the precise effect of MCC inclusion on the superdiffusive pellet dispersal.

3.4.2 *Scaling of particle velocity with driving forces*

The results conclusively demonstrate that use of “effervescent” particle self-propulsion allows very rapid spreading of the solute over the large area of the dish. The rate of spreading can be estimated by considering the diffusivities of both particle and molecule forms of the solutes. The diffusion coefficient D for spherical microparticles with radii of $a = 200 \mu\text{m}$ in water can be calculated from the Stokes–Einstein equation [209] to be $D = 1.075 \times 10^{-15} \text{ m}^2 \text{ s}^{-1}$. By evaluating the average displacement as $x = \sqrt{2Dt}$, it can be readily concluded that it takes nearly 1.3×10^5 hours for a 400 micrometer-sized particle to diffuse 1 mm. The rate of molecular diffusion can be estimated using $D_{\text{NH}_4^+} = 1.980 \times 10^{-9} \text{ m}^2 \text{ s}^{-1}$ [210], $D_{\text{HCO}_3^-} = 1.170 \times 10^{-9} \text{ m}^2 \text{ s}^{-1}$ [211], and $D_{\text{C}_6\text{H}_8\text{O}_7} = 6.570 \times 10^{-9} \text{ m}^2 \text{ s}^{-1}$ [212]. For the same 47-mm Petri dish, citric acid and ammonium

bicarbonate would take appr. 73 and 306 hours, respectively, to cover the surface by the mechanism of molecular diffusion alone. In contrast, our system of self-propelling particles covers the entirety of the 47-mm cell in only two seconds. Figure 5b summarizes the key mechanisms by which the particles in our system could propel. Although it is challenging to identify exactly the contributions from each mode of motility, we derive a few scaling relationships by which we estimate the magnitude of each mechanism. First, we expect that the velocity of the particle scales according to the sum of the forces, as all of them aid in the spreading of the particles:

$$U_{particle} \propto F_{Advection} + F_{Marangoni} + F_{Diffusion} + F_{Buoyancy} \quad (4)$$

Based on our previous estimate, we have established that the time and length scales for particle and molecular diffusion are very slow. Given the small size of the attached bubbles, it is unclear if buoyancy is playing any significant role in particle propulsion. For this reason, we primarily consider the contributions of $F_{Advection}$ and $F_{Marangoni}$. The force of advection originates from the rapid evolution of gas as a result of the neutralization reaction. It is challenging to measure experimentally the pressure gradient inside the bolus in real time during the reaction. As the rate of reaction is essentially a marker of the speed and quantity of gas production, we can write:

$$F_{Advection} \propto k[AB]^x[CA]^y \quad (5)$$

where k is the rate constant, and x and y define the order of the reaction. We can try to estimate the propulsion resulting from Marangoni flows following the expression from Sharma et al. [128], which relates surface tension change and flow rate:

$$F_{Marangoni} \propto \frac{\Delta\gamma_{CA}}{\Delta Q_{CA}} \quad (6)$$

The flow rate is dependent on the amount of CA available in our system, which changes based on the rate at which the reaction is taking place. Based on the timescales shown through plots in Figures 2 and 3, Marangoni spreading dominates at low bulk concentrations of AB and bulk reactivity at high concentrations. At low concentrations of AB, (5) can be expressed as:

$$F_{Advection} \propto k[AB]^x[CA_0 - Q_{CA}\Delta t]^y \quad (7)$$

in which Δt is the time elapsed between pellet contact with the bulk and the onset of pellet disintegration. Using the stoichiometric ratio to delineate “low” and “high” concentrations, we obtain the following expressions:

$$U_{particle} \propto k[AB]^x[CA_0 - Q_{CA}\Delta t]^y + \frac{\Delta\gamma_{CA}}{\Delta Q_{CA}} \quad \text{for } \frac{[AB]}{[CA]} < 3 \quad (8)$$

$$U_{particle} \propto k[AB]^x[CA]^y \quad \text{for } \frac{[AB]}{[CA]} \geq 3 \quad (9)$$

With this understanding, the ideal superdiffusive pellet is composed of an optimized ratio that maximizes contributions from both bulk-acting reactivity and surface-active spreading. Spreading data of bi-component pellets dispensed into DI water show that pellets containing an excess of CA reach full coverage at the highest rate (Figure 4). However, a pellet containing only CA in DI water does not reach the full extent of the Petri dish (Figure 2a). It appears that the optimal ratio allows for sufficient gas production to drive up pressure within the pellet to accelerate fragmentation in

combination with enough surface-active material to bring these fragments to the surface and encourage the development of Marangoni flows. Figure 4a suggests that the optimal ratio is between 1:1 and 2:1 AB:CA. Further investigation of intermediate ratios is necessary to determine the exact effect of bi-component pellet composition on spreading.

3.5 Conclusions

We present findings on the swift radial spreading of a novel, ultra-simple superdiffusive pellet driven by rapidly reacting salt and acid particles in aqueous medium. Rates of spreading were measured for two single-component and two bi-component pellets and showed an accelerated dispersion at several orders of magnitude higher than “passive” diffusion. Pellets containing surface-active citric acid or succinic acid exhibited superior particle propulsion due to Marangoni flows combined with powerful advection arising from gas production. We characterized the spreading behavior as a function of phase, pellet composition, and bulk vs. surface activity. Interestingly, the primary mechanism of spreading shifts from surface activity at low reactant concentrations to bulk reaction-driven expansion at higher concentrations. Analysis of varying ratios of acid to base in bi-component pellets suggests that optimized spreading occurs in pellets containing an excess of surface-active acid.

We have demonstrated how collective propulsion of simple salt and acid granules leads to extremely swift spreading and penetration of large volumes of liquids. The simplicity of our system makes it highly adaptable towards application-specific functionality and complexity. The high rate of surface coverage paired with complete dissolution can be useful in facilitating self-cleaning of fabrics or systems of branched channels without concern for collecting the particles afterwards. Strong advective and Marangoni flows in our system can turn the pellet into a micro- or milli-scale

agitator to enhance mixing of droplets or rehydrated media. Such mixing pellets can also be used to improve reaction outcomes in catalytic applications where mass-transport of products is inefficient and results in blocked reaction sites. Finally, therapeutic agents can be easily loaded into our pellets for rapid and thorough dispersal across the target area. In Chapter 4, we elaborate on how our superdiffusive pellet can significantly improve the efficiency of dermal wound disinfection.

CHAPTER 4

Summary and Outlook

The focus of this dissertation is to explore two new methods of symmetry breaking in active particle systems with emphasis on simplicity and adaptability while answering fundamental questions on the role of AC-electrohydrodynamic (EHD) effects, collective gradient-driven phenomena, and the rational design of active particle systems. We have introduced a new mode of AC field-driven active particle propulsion that is pervasive across multiple classes of microparticles. We have also identified a versatile, highly efficient system of collective spreading capable of swiftly penetrating large volumes of liquids. Through our work, we hope to influence the progress of the active particles field towards a more accessible and robust future.

Chapter 1 introduces methods of powering active particles with a focus on AC field- and chemical gradient-based stimuli. The most fundamental principles of symmetry breaking are discussed to analyze the ways in which engineered active particle systems demonstrate richly diverse patterns of motility. The four basic AC electrokinetic effects, EHD flow, induced-charge electrophoresis (ICEP), self-dielectrophoresis (sDEP), and voltage rectification, ultimately arise from a combination of unbalanced ion and fluid flow. This imbalance is induced by breaking the particle symmetry through shape, composition, and collective interactions. We also discuss the fundamental symmetry-breaking principle allowing for propulsion of chemically-driven active particles (CDAPs). Often catalytic, these particles are designed with a reactive and an inert hemisphere or patch and asymmetry is induced through shape and composition. CDAPs have been shown to operate primarily as individual particles in bulk environments, with a few notable examples of those particles propelling at an air-liquid interface and even fewer showing collective behavior. Overall, Chapter 1 serves to review and summarize the current state of the field and highlight gaps in knowledge that this dissertation seeks to fill.

In Chapter 2, we investigate the use of temporally asymmetric AC waveforms to drive active propulsion of homogeneous dielectric microspheres. The particles move colinear to electric field lines, reversing direction of motion with the reversal of signal asymmetry. We characterized particle behavior as a function of key field parameters – field strength, frequency, and asymmetry – and found that the particles experience size-dependent motion reversal at low frequencies. Further, this effect, which we termed *Asymmetric Field Electrophoresis* (AFEP), was found to persist for metallic and metallodielectric particles as well as dielectric ones. Regardless of the type of particles exposed to sawtooth AC signals, the unevenly induced polarization of the ionic charge layer leads to a major electrohydrodynamic effect of active propulsion. Experimental findings were supported by numerical simulations and a theoretical model.

Here, we offer additional theoretical insights and analysis related to the results discussed in Chapter 2. Particle velocity data as a function of field strength were evaluated against 6 fits using OriginLab software (Table 1, Chapter 2). Based on the R^2 , F, and p-values from these fits, we determined that a cubic function represents the best model. Nonetheless, a power law dependence – referred to as “allometric” in OriginLab – also showed potential, with the expression $U(E) = 6.816 E^{3.828}$. Our initial assumption was based on prior electrokinetic studies suggesting that the exponent for E would be an integer [2,50], with many early studies supporting a cubic relationship [183,185,187]. However, a theoretical analysis by Schnitzer and Yariv showed that for high field strength conditions, high Péclet number, and small Dukhin number ($Du \ll 1$), particle velocity scales $U \propto E^{3/2}$ [213]. Taking a particle velocity of 10×10^{-6} m/s, radius of 2.5×10^{-6} m, and diffusivity of 5.3×10^{-9} m²/s, we estimate $Pe \approx 4.7 \times 10^{-3}$ for our system. Although our current experimental conditions do not fully align with the assumptions of this model, further exploration of field strength-dependent behavior in latex microspheres of intermediate sizes would

enhance our understanding of this phenomenon. The study in this dissertation focuses on beads with diameters of 1.8, 5.0, and 9.4 μm . In many cases, 1.8 and 5.0 μm particles behave very similarly. Expanding the dataset to include additional particles between 5.0 and 9.4 μm would facilitate a more detailed prediction of particle behavior relative to key field parameters.

AFEP is an effective means of propulsion for all types of microparticles due to local ionic concentration polarization and particle-centered dissipative flows. We anticipate that this widespread effect could enhance the suite of AC EHD effects, offering a new and versatile method to control and manipulate a wide array of AC field-driven active particle systems, including future autonomous devices and microbots. At the end of Chapter 2, we demonstrated the multiaxial control of Au-polystyrene (PS) Janus particles (JPs) using the combined effects of AFEP and ICEP. The motility of metallodielectric JPs is due to the electroosmotic slip around the differently polarizable hemispheres of the particle, resulting in motion that is perpendicular to electric field lines [2]. In our report, we control JPs using square pulses of 300 V/cm at 1 kHz and sawtooth signals of 216 V/cm at 4 kHz (forward and reverse). The difference in operating frequencies between the two signal types is due to the appearance of a frequency-dependent angle of trajectory. Preliminary experiments conducted on JPs at varying sawtooth signal frequencies showed a significant change in the angle of motion (Figure 1). JPs moved colinear to electric field lines at higher frequencies (≥ 4 kHz) and shifted towards a more perpendicular trajectory at lower frequencies (1 kHz). Characterization of JP behavior as a function of asymmetric signal frequency as well as degree of signal asymmetry would provide further insight into the role of surface conductance on AFEP motility. We expect that the combined use of asymmetrically polarizable particles in a temporally asymmetric electric field can break new ground in the fundamental understanding of the electrokinetic effects of colloidal particles.

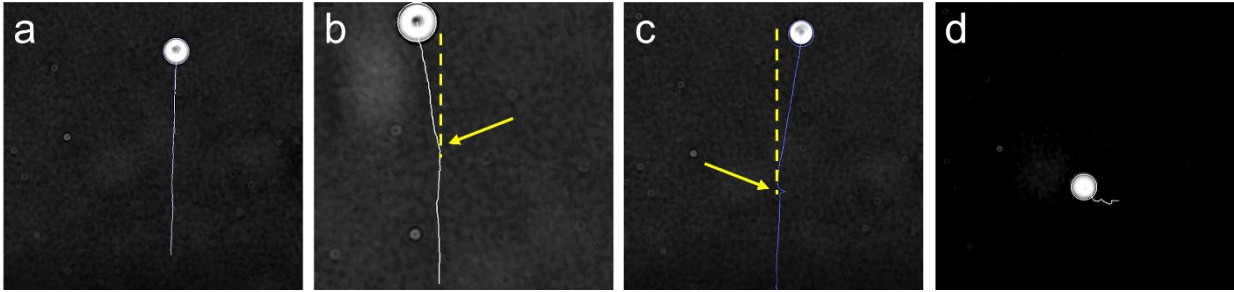


Figure 1: Particle tracking snapshots of 10 μm Au-PS JPs responding to square and sawtooth signals under the following conditions: **a)** 300 V/cm, 2kHz square, **b)** 300 V/cm, 2kHz square to 150 V/cm, 2 kHz reverse sawtooth, **c)** 300 V/cm, 2kHz square to 150 V/cm, 2 kHz forward sawtooth, and **d)** 116 V/cm, 4 kHz reverse sawtooth. The electric field lines span left to right. Yellow arrows in **b)** and **c)** indicate the point of switching from square to sawtooth waveforms. Yellow dotted lines in **b)** and **c)** mark the line that is perpendicular to field lines. **a)** Under a square wave, the JP moves directly perpendicular to field lines. When the signal is switched to a sawtooth waveform at the same frequency, the particle angles slightly to the **b)** left or **c)** right according to signal asymmetry. **d)** When the sawtooth signal frequency is increased further, the JP moves colinear to field lines.

The collective behavior demonstrated by AC field-driven particles is fascinating and in many cases one can observe intricate self-assemblies with unique patterns of motility [11,28,62,81,214]. We have collected preliminary data (Figure 2) with semi-concentrated latex microspheres that shed light on the larger scale transport of particles in an AC electric field. We observed that when 1.8 μm latex particles in a semi-concentrated suspension are exposed to a square wave of 193 V/cm at 500 Hz, the particles assemble into discrete groups of short chains and unbound, individual particles. When this square wave is switched to an asymmetric signal (193 V/cm, 1 kHz), these groups of chains assemble into periodic columns, and over a span of 10-15 minutes, these columns experience macroscopic translation colinear to the electric field (Figure 2a). When the direction of the asymmetric signal is reversed, the direction of the column motion correspondingly reverses.

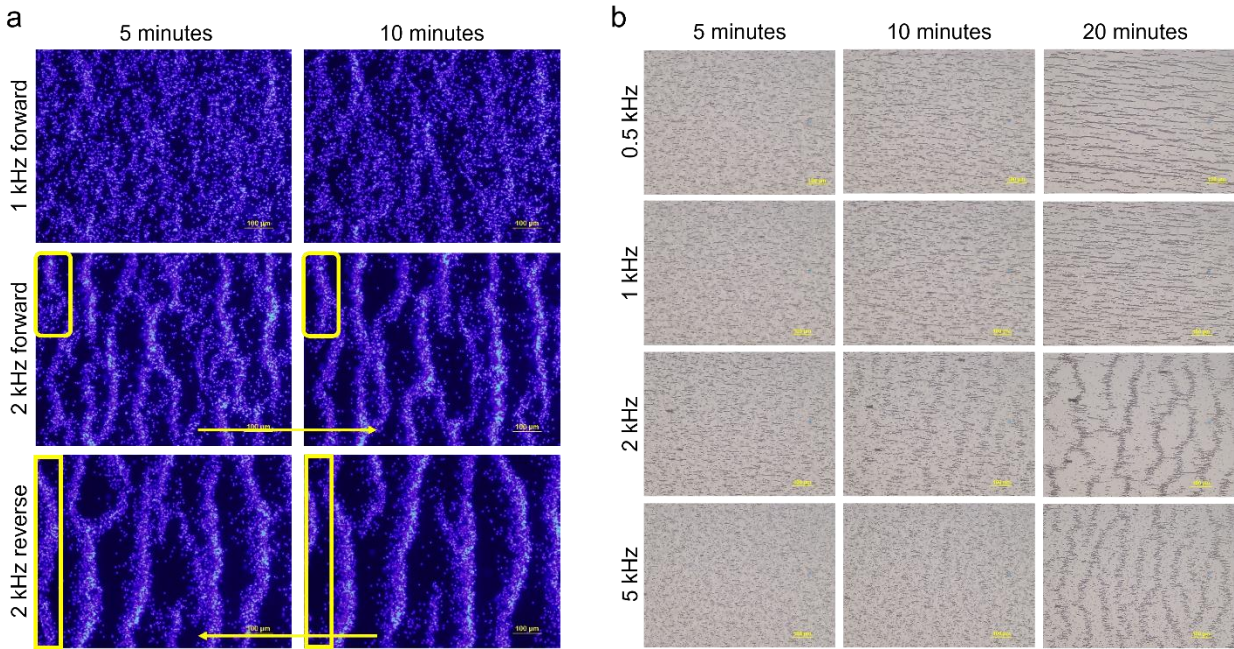


Figure 2: Micrographs of 1.8 μm latex particles in a semi-concentrated suspension upon extended exposure to **a)** square signal and sawtooth signal in sequence and **b)** sawtooth signal only. Fluorescent blue tracer particles were added to the samples in a) to enhance visibility. The samples in a) were first assembled using a square wave of 193 V/cm at 500 Hz for 30 seconds. The signal was then switched to a sawtooth at varying frequencies and macroscopic translation was observed over the 10-minute period. Samples in b) were not assembled using a square waveform. Periodic column formations were observed over a span of 20 minutes for four frequencies.

Although dilute enough to prevent the formation of colloidal crystals, this system is still sufficiently concentrated to induce interactions between the particles, which results in collective motion. Further, there is evidence to suggest that the frequency of the applied sawtooth signal and the duration of signal application influence the number and spacing of self-assembled columns (Figure 2b). A future systematic study covering a range of field strengths, frequencies, and application times would shed light on the collective behavior of dielectric particles under AFEP.

Our present experimental set up involves the use of a gold-coated coplanar electrodes in which the electric field lines extend horizontally across the cell. This configuration allows for ease of visualization through microscopy and image processing as particles travel in a colinear pattern. One drawback to this method, however, is that the particles sediment quickly and maintain contact

with the substrate, or “wall”, throughout the experiments. Electrode edge and wall conductivity effects have been reported as influencing other AC-EHD phenomena to various extents [2,9,52,166,215], and the role of such effects in our system is unclear. We suggest that future experiments can be conducted using a vertical field setup (Figure 3) in which the particle suspension is sandwiched between two ITO-coated glass slides [77]. Application of the sawtooth signal would result in particles moving along the z-axis and can even be used to “hold” the particles in a fixed position when the electrophoretic force is in balance with gravity. While such a setup brings its own experimental and methodological challenges, namely electrical insulation and visualization in the z-axis, vertical field experiments can reveal the role of the substrate in the motility of particles under AFEP. This is especially relevant for the case of low-frequency size-dependent motion reversal.

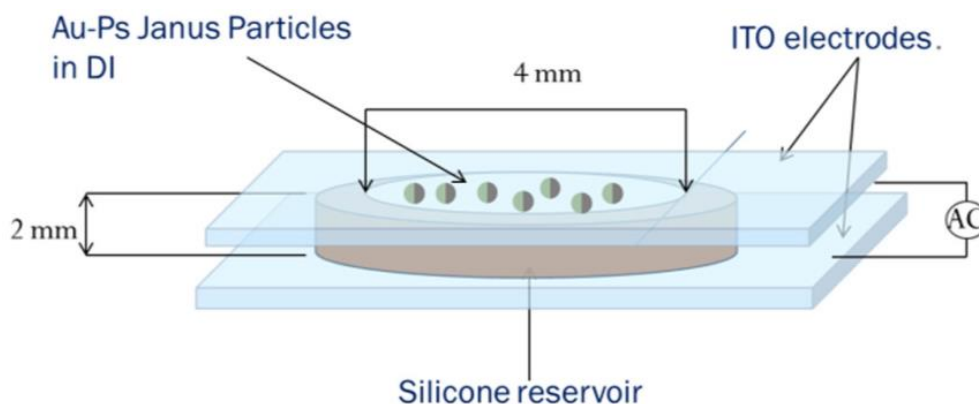


Figure 3: Example of a proposed vertical field setup. Two ITO-coated glass slides form the opposing electrodes in this system. A suspension of particles is placed within a hydrophobic spacer between the slides. Adapted from [77].

Reversal of particle motility in the low frequency regime allowed us to demonstrate proof of concept of a swift size-based particle separation using the coplanar electrode setup. The application of these findings can be extended by integrating AFEP separation principles into more

complete lab-on-a-chip systems for continuous separation of cells or other colloidal particles on the basis of their sizes. As modern microfluidic devices have become more complex, the advanced manufacturing techniques required for their production have escalated their costs [216]. This has spurred the development of a new generation of devices designed to lower costs and improve accessibility in resource-limited settings [217–220]. Lab-on-a-chip devices are primarily fabricated using photolithography, soft lithography, screen printing, 3D printing, and micro- and nanomachining [221]. Current techniques for particle separation include the use of fluorescence tagging and scanning, magnetic particle binding, and selective binding to antibodies or antigens [222]. Due to the size-based dependence on field frequency, AFEP can be tuned to separate at least 3 sizes of particles at once, sending large particles to one electrode, small particles to the opposite electrode, and keeping intermediate particles in between. Even more comprehensive separations can be accomplished by multi-stage separations while continuously changing the frequency. Additional studies are required to identify the resolution of separation for a heavily heterogeneous sample. We hope that the simplicity of our method can reduce the need for complex fabrication and improve the efficiency and ease of access of such devices.

In Chapter 3, we discussed the collective propulsion of a superdiffusive pellet driven by a neutralization reaction between ammonium bicarbonate (AB) and citric acid (CA) or succinic acid (SA). We reported the rate of spreading for single- and bi-component pellets. The single-component systems that were evaluated included: (i) CA pellets dispensed into AB bulk and (ii) AB pellets in CA bulk. Next, bi-component pellets composed of varying ratios of AB:CA and AB:SA were dispensed into water. Particle propulsion in these systems is governed primarily by advection from rapid gas evolution and Marangoni flows arising from the surface activity of CA

and SA. We proposed an optimal ratio of components to maximize contributions from the main driving forces and achieve extremely rapid surface coverage.

This work has the potential to be extended in numerous ways. While we offered our suggestion for an ideal operating ratio of the superdiffusive pellet components, there remain many variables in both system formulation and dispersible pellet fabrication that can significantly change its spreading behavior. Mahiuddin et al. reported the surface tension behavior for four organic acids in water (Figure 4) [ref], two of which were investigated in Chapter 3. In this study, the magnitude of surface tension reduction is reported as: oxalic acid < citric acid < succinic acid < maleic acid.

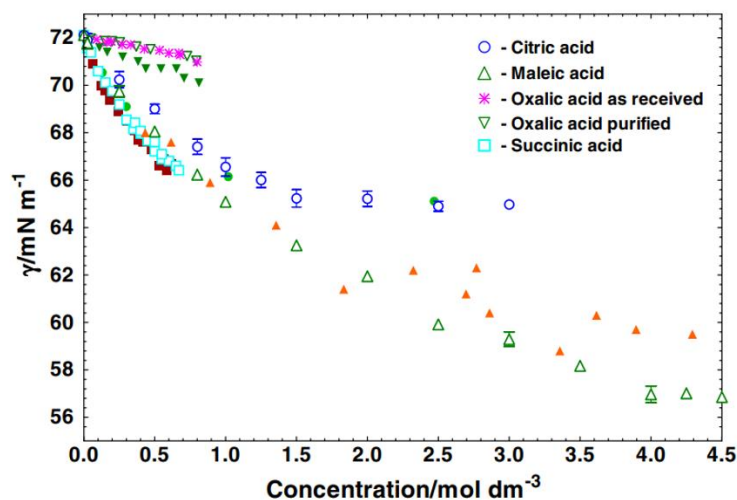


Figure 4: Reported surface tension measurements for four surface-active organic acids [204]. Oxalic acid shows the smallest reduction in surface tension, while maleic acid shows the greatest surface activity.

Preliminary experiments were conducted using oxalic acid (OA) in a bi-component formulation with AB, following the method outlined earlier. Figure 5 shows snapshots of the pellet spreading in water at the 1-second mark for three ratios. Although faint, the signature green corona indicating surface activity is visible in all three cases. The pellet with the 1:1 AB:OA formulation

appears to have the greatest surface spreading, which curiously follows the same trend seen for the AB:CA and AB:SA pellets. In all cases, AB:OA spreading is less pronounced than that of AB:CA or AB:SA pellets, which may be due to the lower surface activity of OA. It remains to be seen how the use of maleic acid may alter the dynamics of particle propulsion in this superdiffusive pellet. This work would benefit from a complete systematic study of all four surface-active acids in pellets formulated with varying ratios with AB. Addition of a dissolvable coating of the acid particles may also enable multiple stages of spreading for more complex applications.

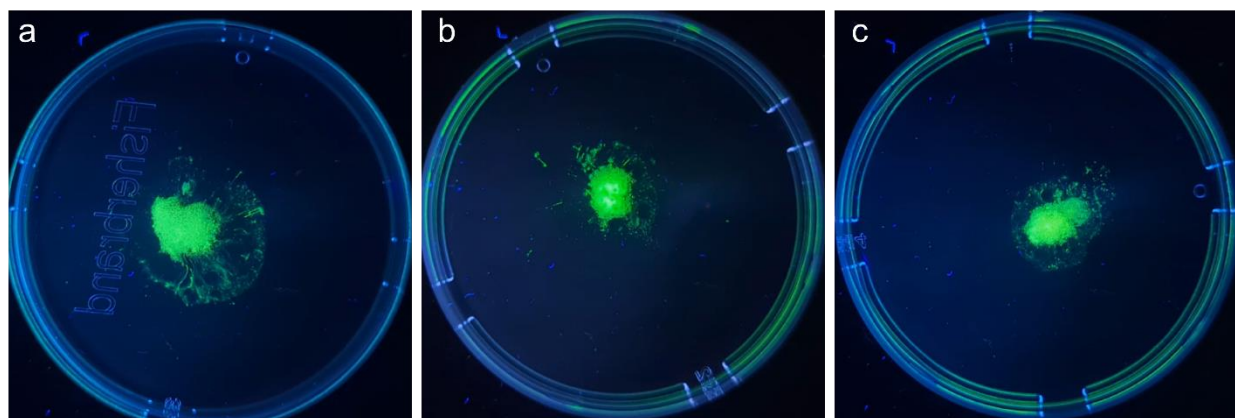


Figure 5: Snapshots taken 1 second after contact with the bulk solution for **a)** 1:1 AB:OA, **b)** 2:1 AB:OA (stoichiometric ratio), and **c)** 1:2 AB:OA. The green ring extending outwards from the bolus shows the degree of surface spreading of the oxalic acid.

Tablet density is a critical parameter influencing disintegration speed [208] and, in our case, particle motility as well. Experiments were performed on highly compressed, finely ground AB and CA pellets at ratios of 1:1 and 6:1 AB:CA. Upon contact with water, both pellets began to move along the air-water interface, dissolving and reacting as they propelled. Figure 6 shows snapshots of the pellets at various stages of propulsion. The lateral motility was maintained for appr. 15 seconds until the pellets were fully consumed by the reaction. The pellets appeared to maintain a circular, almost spiraling trajectory until contact with the Petri dish walls. To our

knowledge, there have been no reports of similar active micro- or milli-particles driven by surface-active organic acids.

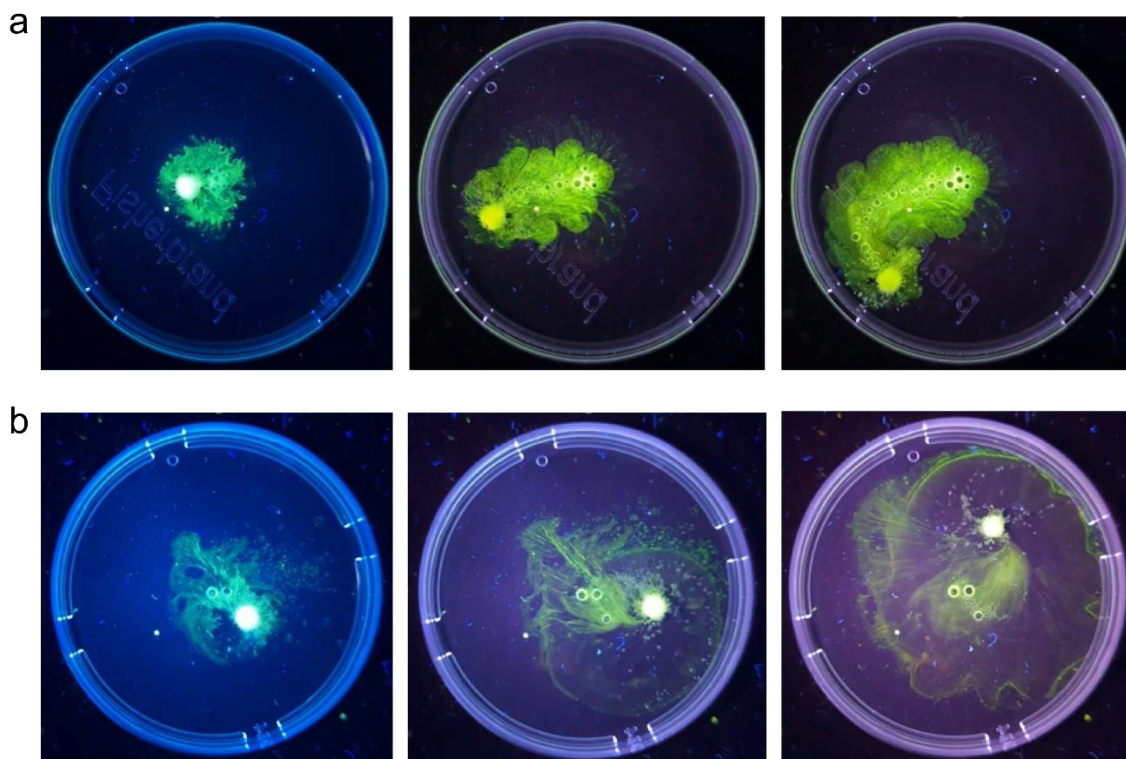


Figure 6: Snapshots of highly compressed **a)** 6:1 and **b)** 1:1 AB:CA pellets traversing across the air-water interface. The pellets disintegrate very slowly, which allows them to travel further as a single unit.

This system opens the door to explore a number of fundamental questions relating to active particle propulsion driven by Marangoni flows combined with self-diffusiophoresis and bubble production. Additional patterns of motility may be induced by incorporating asymmetry in the pellet shape and composition. Propulsion time can be increased by using a more surface-active acid, such as maleic acid. Figure 7 provides some examples of potential engineered superdiffusive pellets. One final aspect warranting further investigation is the size of the pellet. The dimensions of the pellets used for this work are appr. 1.5 mm radius \times 3 mm height. They were composed of

particles 300-500 μm in size. At this size scale, inertial forces must be taken into consideration. For example, when taking a particle size of 200×10^{-3} m, average velocity of 23.5×10^{-3} m/s, density of 1 kg/m^3 , and viscosity of 10^{-3} Pa·s, we evaluate $Re \approx 4.7$. Many active particles operate under very low Reynolds numbers [65,110,223]. Reducing pellet size to the sub-millimeter range may reveal new insights into reaction behavior and particle speed at that scale.

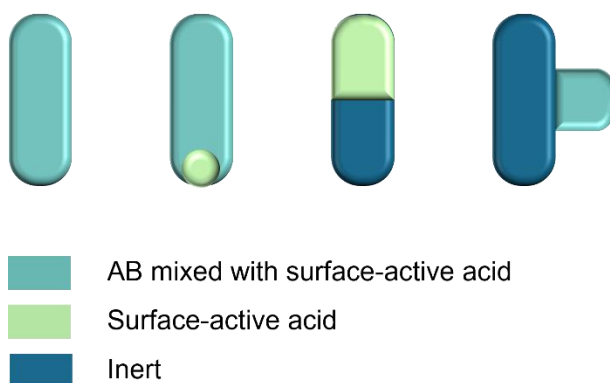


Figure 7: Examples of the possible design patterns of engineered superdiffusive pellets using various configurations of active and inert mixtures.

As research on active particles transitions from basic studies to application-driven development, scientists are investigating multifunctional particles that respond to multiple stimuli. These particles can be activated by two or more stimuli either consecutively or simultaneously, achieving functionality that is unattainable with a single propulsion mechanism. This approach offers notable advantages over single-stimulus methods by enhancing the particles' versatility and introducing new, nonlinear behaviors. Currently, there is a wide range of multifunctional particles responsive to chemical, biological, magnetic, acoustic, and optical stimuli [92,94,97,224,225]. One way to introduce a higher degree of control to our superdiffusive pellet is by incorporating photoacid generators (PAGs). PAGs are compounds that irreversibly produce acids upon

irradiation with light, usually in the UV region [226]. In the case of the most common PAGS, which are diaryliodonium and triarylsulfonium salts, absorption of light results in cleavage of the carbon-sulfur or carbon-iodine bonds. Anions and free radicals liberated in this process combine with a hydrogen-donating solvent to produce acids [227].

Traditionally, PAGs have been used for photolithography, chemically amplified photoresists, and photoinitiation of polymerization, with very few biomedical applications due to the generally toxic nature of the compounds and their byproducts. However, recent years have seen an increase in the development and use of PAGs for tumor treatment, disinfection, and even enzyme activation [228,229]. On the basis of these background systems, we have identified two water-soluble PAGs to adapt into our system: 8-Hydroxypyrene-1,3,6-trisulfonate trisodium salt (HPTS) and 2-nitrobenzaldehyde. Figure 8 shows the reaction schemes by which these two compounds generate acids. These PAGS could be added to the bulk solvent or packed directly into the solid pellet. Exposure to UV light would allow us to selectively “activate” the superdiffusive effect locally. While 8-HPTS is fully soluble in water, 2-nitrobenzaldehyde is only partially so, dissolving more readily in alcohol. Further modifications may be necessary to integrate these compounds into our superdiffusive pellet system.

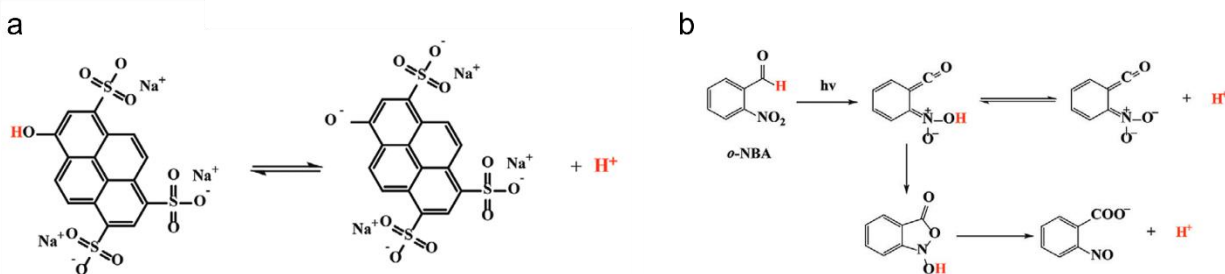


Figure 8: Reaction mechanisms for **a)** 8-Hydroxypyrene-1,3,6-trisulfonate trisodium salt (HPTS) and **b)** 2-nitrobenzaldehyde [228].

The self-motile dissolvable particle system presented in Chapter 3 is remarkable in its simplicity and ease of fabrication. Nevertheless, it should be recognized that the initial practical applications of active particle systems should be one of large importance to humans and society to justify the increased complexity and costs. Following research on such systems, as well as contacts and discussions with medical researchers, we have identified the area of medical disinfection, and specifically dermal wound disinfection as being an ideal target of high importance. Wound management continues to be a challenging issue faced by modern healthcare [230–233]. Chronic wounds are often the result of a bacterial infection and are difficult to treat due to a protective layer of extracellular polysaccharides secreted by the bacteria, known as a biofilm [231]. Biofilms protect the encased bacteria from therapeutic agents as well as the body's immune system [234,235], making it increasingly important to find methods of biofilm disruption. A recent study conducted by Villa et al. showed that a combination of the antibacterial properties of TiO_2 , generation of reactive oxygen species (ROS), and bubble production from decomposition of H_2O_2 disrupted dental biofilms [139].

We suggest that a similar approach can help in the disruption of dermal biofilms towards more efficient mitigation of bacterial infection. Figure 9 provides a schematic of the proposed disinfection strategy, in which therapeutic agents are loaded into the pellet mixture before compression. Application of the pellet into a wound with a small amount of fluid will cause the rapid spreading of the disinfecting agent all around.

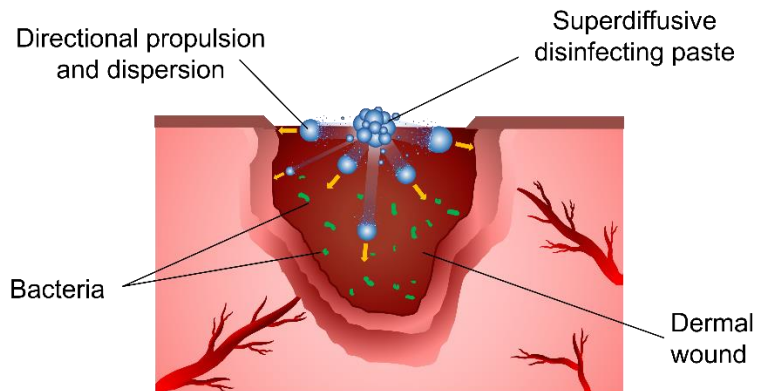


Figure 9: Illustration of the mode of operation of our superdiffusive pellet while treating a dermal wound.

Preliminary experiments were conducted to assess the spreading and disinfecting capabilities of 5-aminolevulinic acid (5-ALA) and methylene blue (MB). Both 5-ALA and MB were evaluated as being suitable water soluble, light-activated, medically established disinfecting agents [232,232,236–242]. 5-ALA has a broad absorption range: at 465 nm, the compound emits red light and can be used as a diagnostic tool; at 635 nm, the compound generates ROS and becomes cytotoxic [239]. Upon exposure to 635 nm light, MB also becomes cytotoxic [232]. Towards the goal of studying pellet penetration with respect to dermal wounds, we developed preliminary simplified models of skin infiractures on which to test our system. Four representative dermal wound models that are commonly used in biomedical studies were identified: abrasion, laceration, incision, and puncture [243,244]. We modeled these wounds in-vitro by shaping in corresponding ways porcine gelatin discs (Figure 10).

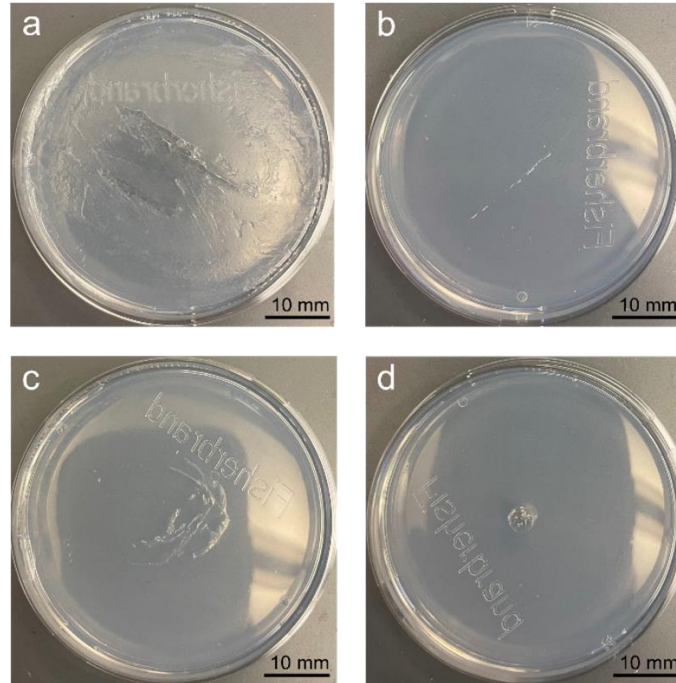


Figure 10: Four types of model dermal wounds produced on porcine gelatin discs: **a)** abrasion, **b)** incision, **c)** laceration, and **d)** puncture. Active and passive pellets were applied to these representative models to assess spreading capacity on rough surface morphologies.

Passive and active pellets were applied to each model wound. Inconsistencies and variations in the wound shaping process necessitated a modified, consistent wound pattern. We designed a thin acrylic mold to produce a narrow channel or “trench” in the gelatin. A thin layer of phosphate-buffered saline (PBS) was applied to the trench to simulate the release of fluids in a flesh wound. Figure 11a and 11b show the penetration results of active and passive pellets in two neighboring trenches shaped in the same gelatin disc. The active system, composed of AB and 5-ALA, traversed the length of the channel twice as fast as the passive system, which contained only AB.

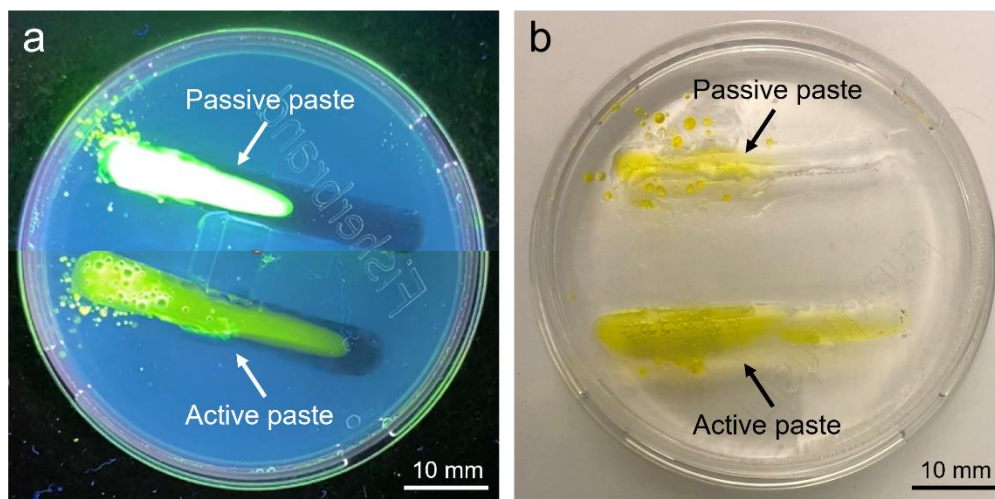


Figure 11: Results of pellet spreading and penetration in gelatin trench model experiments. **a)** Snapshots under fluorescence of active (2:1 AB:5-ALA) and passive (AB) pellets taken at the 30-second mark. The materials released for the active pellet successfully traverse the length of the channel twice as rapidly as the passive paste. **b)** Post-experiment images of the active and passive pellets in their respective trenches.

Contact assays were completed for 6 conditions in duplicate. Two main active formulations were used: (1) AB with 5-ALA and (2) AB with CA and MB. The positive controls were: AB, MB, 5-ALA, CA, and light (no added reagents). The negative control system contained *E. coli* with no added antibacterials. Our active pellet was tested in 2 different ratios of salt to acid. All samples were exposed to 630 nm light for 30 minutes. Results following serial dilutions for these assays are shown in Figure 12a and 12b. MB and 5-ALA demonstrated a high degree of bacterial killing efficiency as expected. However, the active formulations did not prove to be as effective, only showing signs of disinfection in the 10^7 range. There are two reasons why this may be the case. The first is a reaction between 5-ALA and AB. The mechanism by which 5-ALA operates is complex, as the amino acid is a precursor in the heme biosynthesis pathway and leads to the formation of the photosensitizer Protoporphyrin IX (PpIX), which is then activated by red light [236,237]. Even minor interference with this process can render the final product inactive. We believe that AB may be attacking functional groups on 5-ALA, limiting the production of

PpIX, and ultimately resulting in a very low rate of cell death. In the case of MB, there is a muted effect due to binding with CA. MB works by binding to acidic components of cells and producing singlet oxygen upon exposure to red light, which results in cell apoptosis [232,241]. However, because CA is a strong acidic component in this system, it appears that MB is predominantly bound to the CA and bacterial cell death is not achieved.

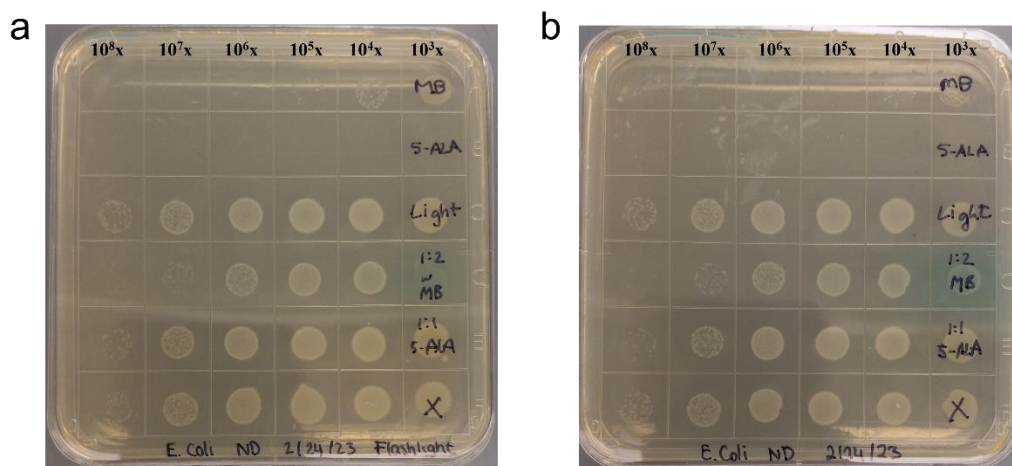


Figure 12: E. coli contact assays were conducted in duplicate to assess the disinfecting capacity of the active paste formulation. **a)** and **b)** show the serial dilution results after an 8-hour incubation period. The active components used were MB and 5-ALA at varying ratios. The corresponding dilution factor is indicated in the top row. Positive controls were MB and 5-ALA, which were very effective as expected. MB showed bacterial death in the lower dilution range (10⁵-10⁴), while 5-ALA eliminated all bacteria. Negative control is indicated in the bottom row. Active formulations only showed signs of disinfection in the range of high dilution (10⁷-10⁸).

In addition to evaluating the disinfecting capabilities of our active therapeutic pellet, we assessed the rate the spreading between various ratios of active formulations in comparison to that of their individual components. The fundamental idea we sought to investigate was focused on the degree to which active superdiffusion outperforms the molecular diffusion of some typical disinfection compounds. Five conditions were examined in PBS: 3 ratios of AB:5-ALA along with AB and 5-ALA individually. The results from this study are shown in Figure 13, where snapshots

were taken 10 seconds after the pellet was dispensed. It is clearly seen that in all cases, the active system coverage (a-c) is significantly greater than the individual components (d-e), with the 2:1 ratio reaching roughly 10 times the surface area of only 5-ALA. Thus, the utility of the study was twofold: we confirmed that the disinfecting compound alone cannot alone attain the efficiency of spreading that we see in the active pellet, and we also gained insight into the optimized ratio for the formulation.

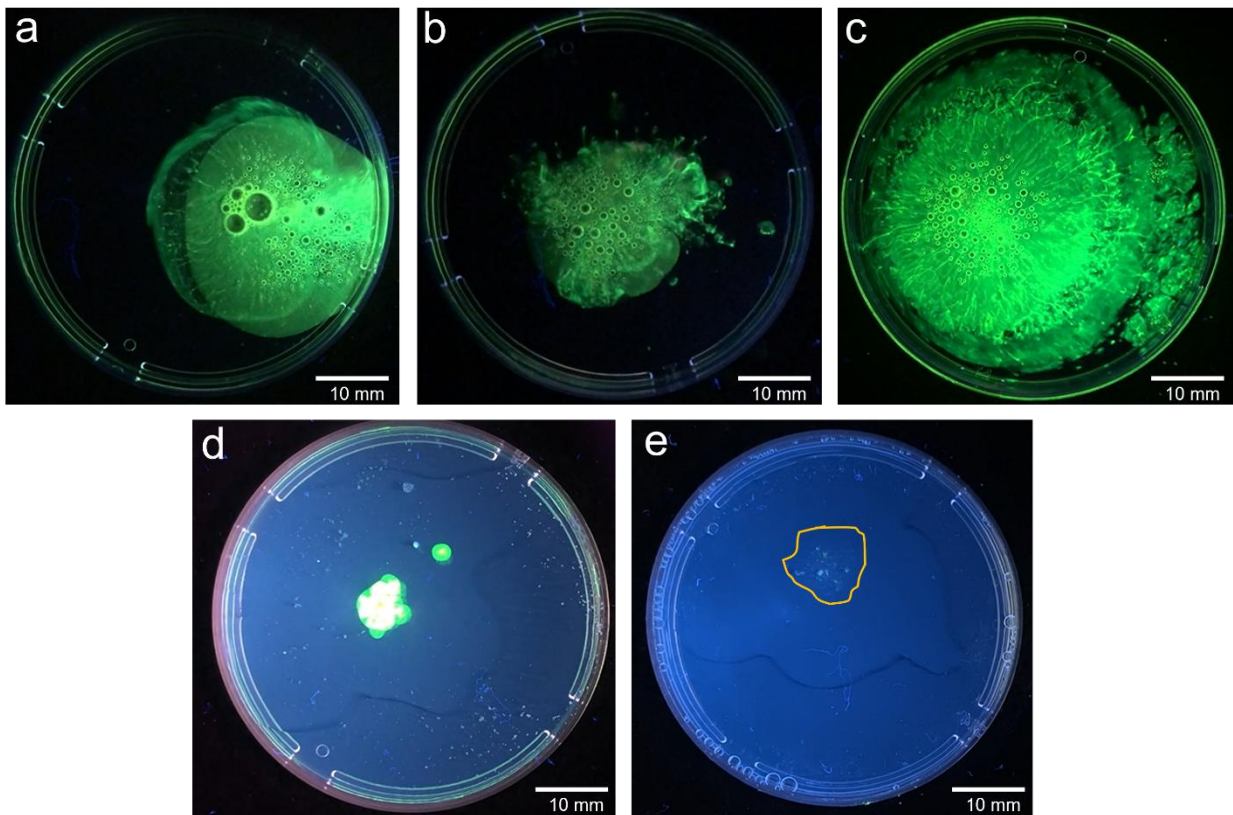


Figure 13: Snapshots showing the progression of spreading for the following systems: (a) 1:1 AB:5-ALA, (b) 1:2 AB:5-ALA, (c) 2:1 AB:5-ALA, and (d) AB in PBS. The boundary for pure 5-ALA is shown in (e). Each snapshot was taken 10 seconds after the paste was dispensed. The optimized ratio was determined to be 2:1 as it showed the greatest coverage in the shortest time. In all cases, the active system spreading (a-c) is significantly greater than molecular diffusion of individual components (d-e).

We have optimized the ratio of acid to salt to produce the desired superdiffusive spreading effect. However, due to the interactions between components of our pellet, the disinfecting effect was compromised. Analysis of experimental results showed that stronger propulsion comes at the cost of reduced antimicrobial activity. During the studies of our contact assays (Figure 12), we examined several different ratios in an attempt to resolve this discrepancy. Still, further work will need to be done to achieve an acceptable level of disinfection with agents that are more compatible with our formulation.

We have reported in this dissertation research progress in two novel directions from which we can address the current challenges in the field of active particles. Both of these studies could have a transformative impact on the field of active particles by answering fundamental questions on the role of AC-EHD effects, collective gradient-driven phenomena, and the rational design of active particle systems. Through our interdisciplinary research on these topics, we aimed to enrich the knowledge in this rapidly developing research field.

REFERENCES

1. A. Walther and A. H. E. Müller, *Janus Particles: Synthesis, Self-Assembly, Physical Properties, and Applications*, Chem. Rev. **113**, 5194 (2013).
2. S. Gangwal, O. J. Cayre, M. Z. Bazant, and O. D. Velev, *Induced-Charge Electrophoresis of Metallo-dielectric Particles*, Phys. Rev. Lett. **100**, 058302 (2008).
3. A. M. Boymelgreen and T. Miloh, *A Theoretical Study of Induced-Charge Dipolephoresis of Ideally Polarizable Asymmetrically Slipping Janus Particles*, Physics of Fluids **23**, 072007 (2011).
4. T. Mano, J.-B. Delfau, J. Iwasawa, and M. Sano, *Optimal Run-and-Tumble-Based Transportation of a Janus Particle with Active Steering*, Proceedings of the National Academy of Sciences **114**, E2580 (2017).
5. L. Zhang, Z. Xiao, X. Chen, J. Chen, and W. Wang, *Confined 1D Propulsion of Metallo-dielectric Janus Micromotors on Microelectrodes under Alternating Current Electric Fields*, ACS Nano **13**, 8842 (2019).
6. X. Huo, Y. Wu, A. Boymelgreen, and G. Yossifon, *Analysis of Cargo Loading Modes and Capacity of an Electrically-Powered Active Carrier*, Langmuir **36**, (2020).
7. S. Park and G. Yossifon, *Micromotor-Based Biosensing Using Directed Transport of Functionalized Beads*, ACS Sens. **5**, 936 (2020).
8. Y. Wu, A. Fu, and G. Yossifon, *Active Particles as Mobile Microelectrodes for Selective Bacteria Electroporation and Transport*, Science Advances **6**, eaay4412 (2020).
9. A. Boymelgreen and G. Yossifon, *Observing Electrokinetic Janus Particle-Channel Wall Interaction Using Microparticle Image Velocimetry*, Langmuir **31**, 8243 (2015).
10. D. Nishiguchi and M. Sano, *Mesosopic Turbulence and Local Order in Janus Particles Self-Propelling under an Ac Electric Field*, Phys. Rev. E **92**, 052309 (2015).
11. J. Zhang and S. Granick, *Natural Selection in the Colloid World: Active Chiral Spirals*, Faraday Discuss. **191**, 35 (2016).
12. J. Zhang, J. Yan, and S. Granick, *Directed Self-Assembly Pathways of Active Colloidal Clusters*, Angewandte Chemie International Edition **55**, 5166 (2016).
13. J. Yan, M. Han, J. Zhang, C. Xu, E. Luijten, and S. Granick, *Reconfiguring Active Particles by Electrostatic Imbalance*, Nature Mater **15**, 1095 (2016).
14. D. Nishiguchi, J. Iwasawa, H.-R. Jiang, and M. Sano, *Flagellar Dynamics of Chains of Active Janus Particles Fueled by an AC Electric Field*, New J. Phys. **20**, 015002 (2018).

15. C.-H. Lin, Y.-L. Chen, and H.-R. Jiang, *Orientation-Dependent Induced-Charge Electrophoresis of Magnetic Metal-Coated Janus Particles with Different Coating Thicknesses*, RSC Adv. **7**, 46118 (2017).
16. A. F. Demirörs, F. Eichenseher, M. J. Loessner, and A. R. Studart, *Colloidal Shuttles for Programmable Cargo Transport*, Nat Commun **8**, 1872 (2017).
17. G. Loget and A. Kuhn, *Bulk Synthesis of Janus Objects and Asymmetric Patchy Particles*, J. Mater. Chem. **22**, 15457 (2012).
18. D. Rodríguez-Fernández and L. M. Liz-Marzán, *Metallic Janus and Patchy Particles*, Particle & Particle Systems Characterization **30**, 46 (2013).
19. I. Kretzschmar and J. H. (Kevin) Song, *Surface-Anisotropic Spherical Colloids in Geometric and Field Confinement*, Current Opinion in Colloid & Interface Science **16**, 84 (2011).
20. J. G. Lee, A. M. Brooks, W. A. Shelton, K. J. M. Bishop, and B. Bharti, *Directed Propulsion of Spherical Particles along Three Dimensional Helical Trajectories*, Nat Commun **10**, 2575 (2019).
21. W. Li, H. Palis, R. Mérindol, J. Majimel, S. Ravaine, and E. Duguet, *Colloidal Molecules and Patchy Particles: Complementary Concepts, Synthesis and Self-Assembly*, Chem. Soc. Rev. **49**, 1955 (2020).
22. E. Bianchi, B. Capone, I. Coluzza, L. Rovigatti, and P. D. J. van Oostrum, *Limiting the Valence: Advancements and New Perspectives on Patchy Colloids, Soft Functionalized Nanoparticles and Biomolecules*, Phys. Chem. Chem. Phys. **19**, 19847 (2017).
23. S. Ravaine and E. Duguet, *Synthesis and Assembly of Patchy Particles: Recent Progress and Future Prospects*, Current Opinion in Colloid & Interface Science **30**, 45 (2017).
24. Z. Rozynek and A. Józefczak, *Patchy Colloidosomes – an Emerging Class of Structures*, Eur. Phys. J. Spec. Top. **225**, 741 (2016).
25. M. J. Solomon, *Directions for Targeted Self-Assembly of Anisotropic Colloids from Statistical Thermodynamics*, Current Opinion in Colloid & Interface Science **16**, 158 (2011).
26. J. Zhang, E. Luijten, B. A. Grzybowski, and S. Granick, *Active Colloids with Collective Mobility Status and Research Opportunities*, Chem. Soc. Rev. **46**, 5551 (2017).
27. F. Ma, X. Yang, H. Zhao, and N. Wu, *Inducing Propulsion of Colloidal Dimers by Breaking the Symmetry in Electrohydrodynamic Flow*, Phys. Rev. Lett. **115**, 208302 (2015).
28. F. Ma, S. Wang, D. T. Wu, and N. Wu, *Electric-Field-Induced Assembly and Propulsion of Chiral Colloidal Clusters*, PNAS **112**, 6307 (2015).

29. A. M. Brooks, M. Tasinkevych, S. Sabrina, D. Velegol, A. Sen, and K. J. M. Bishop, *Shape-Directed Rotation of Homogeneous Micromotors via Catalytic Self-Electrophoresis*, *Nat Commun* **10**, 495 (2019).
30. C. W. Shields, K. Han, F. Ma, T. Miloh, G. Yossifon, and O. D. Velev, *Supercolloidal Spinners: Complex Active Particles for Electrically Powered and Switchable Rotation*, *Adv. Funct. Mater.* **28**, 1803465 (2018).
31. A. M. Brooks, S. Sabrina, and K. J. M. Bishop, *Shape-Directed Dynamics of Active Colloids Powered by Induced-Charge Electrophoresis*, *Proceedings of the National Academy of Sciences* **115**, E1090 (2018).
32. G. Kunti, Y. Wu, and G. Yossifon, *Rational Design of Self-Propelling Particles for Unified Cargo Loading and Transportation*, *Small* **17**, e2007819 (2021).
33. N. L. Abbott and O. D. Velev, *Active Particles Propelled into Researchers' Focus*, *Current Opinion in Colloid & Interface Science* **21**, 1 (2016).
34. J. Orozco, G. Cheng, D. Vilela, S. Sattayasamitsathit, R. Vazquez-Duhalt, G. Valdés-Ramírez, O. S. Pak, A. Escarpa, C. Kan, and J. Wang, *Micromotor-Based High-Yielding Fast Oxidative Detoxification of Chemical Threats*, *Angewandte Chemie International Edition* **52**, 13276 (2013).
35. M. Guix, C. C. Mayorga-Martinez, and A. Merkoçi, *Nano/Micromotors in (Bio)Chemical Science Applications*, *Chem. Rev.* **114**, 6285 (2014).
36. V. Liljeström, C. Chen, P. Dommersnes, J. O. Fossum, and A. H. Gröschel, *Active Structuring of Colloids through Field-Driven Self-Assembly*, *Current Opinion in Colloid & Interface Science* **40**, 25 (2019).
37. H. Wang and M. Pumera, *Fabrication of Micro/Nanoscale Motors*, *Chem. Rev.* **115**, 8704 (2015).
38. M. Driscoll and B. Delmotte, *Leveraging Collective Effects in Externally Driven Colloidal Suspensions: Experiments and Simulations*, *Current Opinion in Colloid & Interface Science* **40**, 42 (2019).
39. S. J. Ebbens and J. R. Howse, *In Pursuit of Propulsion at the Nanoscale*, *Soft Matter* **6**, 726 (2010).
40. T. Xu, W. Gao, L.-P. Xu, X. Zhang, and S. Wang, *Fuel-Free Synthetic Micro-/Nanomachines*, *Advanced Materials* **29**, 1603250 (2017).
41. L. Bouffier, V. Ravaine, N. Sojic, and A. Kuhn, *Electric Fields for Generating Unconventional Motion of Small Objects*, *Current Opinion in Colloid & Interface Science* **21**, 57 (2016).

42. F. Kümmer, B. ten Hagen, R. Wittkowski, I. Buttinoni, R. Eichhorn, G. Volpe, H. Löwen, and C. Bechinger, *Circular Motion of Asymmetric Self-Propelling Particles*, Phys. Rev. Lett. **110**, 198302 (2013).
43. A. M. Boymelgreen, T. Balli, T. Miloh, and G. Yossifon, *Active Colloids as Mobile Microelectrodes for Unified Label-Free Selective Cargo Transport*, Nat Commun **9**, 760 (2018).
44. O. D. Velev and K. H. Bhatt, *On-Chip Micromanipulation and Assembly of Colloidal Particles by Electric Fields*, Soft Matter **2**, 738 (2006).
45. M. Trau, D. A. Saville, and I. A. Aksay, *Field-Induced Layering of Colloidal Crystals*, Science **272**, 706 (1996).
46. X. Yang, S. Johnson, and N. Wu, *The Impact of Stern-Layer Conductivity on the Electrohydrodynamic Flow Around Colloidal Motors under an Alternating Current Electric Field*, Advanced Intelligent Systems **1**, 1900096 (2019).
47. W. D. Ristenpart, P. Jiang, M. A. Slowik, C. Punckt, D. A. Saville, and I. A. Aksay, *Electrohydrodynamic Flow and Colloidal Patterning near Inhomogeneities on Electrodes*, Langmuir **24**, 12172 (2008).
48. S. T. Chang, V. N. Paunov, D. N. Petsev, and O. D. Velev, *Remotely Powered Self-Propelling Particles and Micropumps Based on Miniature Diodes*, Nature Mater **6**, 235 (2007).
49. R. Sharma and O. D. Velev, *Remote Steering of Self-Propelling Microcircuits by Modulated Electric Field*, Adv. Funct. Mater. **25**, 5512 (2015).
50. T. M. SQUIRES and M. Z. BAZANT, *Induced-Charge Electro-Osmosis*, Journal of Fluid Mechanics **509**, 217 (2004).
51. T. M. Squires and M. Z. Bazant, *Breaking Symmetries in Induced-Charge Electro-Osmosis and Electrophoresis*, Journal of Fluid Mechanics **560**, 65 (2006).
52. A. Boymelgreen, G. Yossifon, and T. Miloh, *Propulsion of Active Colloids by Self-Induced Field Gradients*, Langmuir **32**, 9540 (2016).
53. W. Wang, W. Duan, S. Ahmed, T. E. Mallouk, and A. Sen, *Small Power: Autonomous Nano- and Micromotors Propelled by Self-Generated Gradients*, Nano Today **8**, 531 (2013).
54. M. Trau, D. A. Saville, and I. A. Aksay, *Assembly of Colloidal Crystals at Electrode Interfaces*, Langmuir **13**, 6375 (1997).
55. W. D. Ristenpart, I. A. Aksay, and D. A. Saville, *Assembly of Colloidal Aggregates by Electrohydrodynamic Flow: Kinetic Experiments and Scaling Analysis*, Phys. Rev. E **69**, 021405 (2004).

56. W. D. Ristenpart, I. A. Aksay, and D. A. Saville, *Electrohydrodynamic Flow around a Colloidal Particle near an Electrode with an Oscillating Potential*, *Journal of Fluid Mechanics* **575**, 83 (2007).
57. W. D. Ristenpart, I. A. Aksay, and D. A. Saville, *Electrically Driven Flow near a Colloidal Particle Close to an Electrode with a Faradaic Current*, *Langmuir* **23**, 4071 (2007).
58. J. A. Fagan, P. J. Sides, and D. C. Prieve, *Mechanism of Rectified Lateral Motion of Particles near Electrodes in Alternating Electric Fields below 1 kHz*, *Langmuir* **22**, 9846 (2006).
59. T. J. Woehl, B. J. Chen, K. L. Heatley, N. H. Talken, S. C. Bukosky, C. S. Dutcher, and W. D. Ristenpart, *Bifurcation in the Steady-State Height of Colloidal Particles near an Electrode in Oscillatory Electric Fields: Evidence for a Tertiary Potential Minimum*, *Phys. Rev. X* **5**, 011023 (2015).
60. D. J. Laser, A. M. Myers, S. Yao, K. F. Bell, K. E. Goodson, J. G. Santiago, and T. W. Kenny, *Silicon Electroosmotic Micropumps for Integrated Circuit Thermal Management*, in *TRANSDUCERS '03. 12th International Conference on Solid-State Sensors, Actuators and Microsystems. Digest of Technical Papers (Cat. No.03TH8664)*, Vol. 1 (2003), pp. 151–154 vol.1.
61. O. Schnitzer and E. Yariv, *Strong-Field Electrophoresis*, *Journal of Fluid Mechanics* **701**, 333 (2012).
62. S. Gangwal, O. J. Cayre, and O. D. Velev, *Dielectrophoretic Assembly of Metallodielectric Janus Particles in AC Electric Fields*, *Langmuir* **24**, 13312 (2008).
63. J. G. Lee, A. Al Harraq, K. J. M. Bishop, and B. Bharti, *Fabrication and Electric Field-Driven Active Propulsion of Patchy Microellipsoids*, *J. Phys. Chem. B* **125**, 4232 (2021).
64. Z. Wang, W. Xu, Z. Wang, D. Lyu, Y. Mu, W. Duan, and Y. Wang, *Polyhedral Micromotors of Metal–Organic Frameworks: Symmetry Breaking and Propulsion*, *J. Am. Chem. Soc.* **143**, 19881 (2021).
65. E. Han, L. Zhu, J. W. Shaevitz, and H. A. Stone, *Low-Reynolds-Number, Biflagellated Quincke Swimmers with Multiple Forms of Motion*, *Proceedings of the National Academy of Sciences* **118**, e2022000118 (2021).
66. G. E. Pradillo, H. Karani, and P. M. Vlahovska, *Quincke Rotor Dynamics in Confinement: Rolling and Hovering*, *Soft Matter* **15**, 6564 (2019).
67. A. Bricard, J.-B. Caussin, N. Desreumaux, O. Dauchot, and D. Bartolo, *Emergence of Macroscopic Directed Motion in Populations of Motile Colloids*, *Nature* **503**, 95 (2013).

68. A. Bricard, J.-B. Caussin, D. Das, C. Savoie, V. Chikkadi, K. Shitara, O. Chepizhko, F. Peruani, D. Saintillan, and D. Bartolo, *Emergent Vortices in Populations of Colloidal Rollers*, *Nat Commun* **6**, 7470 (2015).
69. R. Dong, Q. Zhang, W. Gao, A. Pei, and B. Ren, *Highly Efficient Light-Driven TiO_2 -Au Janus Micromotors*, *ACS Nano* **10**, 839 (2016).
70. A. Ruditskiy, B. Ren, and I. Kretzschmar, *Behaviour of Iron Oxide (Fe_3O_4) Janus Particles in Overlapping External AC Electric and Static Magnetic Fields*, *Soft Matter* **9**, 9174 (2013).
71. M. Guix, A. K. Meyer, B. Koch, and O. G. Schmidt, *Carbonate-Based Janus Micromotors Moving in Ultra-Light Acidic Environment Generated by HeLa Cells in Situ*, *Scientific Reports* (Nature Publisher Group) **6**, 21701 (2016).
72. W. Gao, A. Pei, R. Dong, and J. Wang, *Catalytic Iridium-Based Janus Micromotors Powered by Ultralow Levels of Chemical Fuels*, *J. Am. Chem. Soc.* **136**, 2276 (2014).
73. M. Valdez-Garduño, M. Leal-Estrada, E. S. Oliveros-Mata, D. I. Sandoval-Bojorquez, F. Soto, J. Wang, and V. Garcia-Gradilla, *Density Asymmetry Driven Propulsion of Ultrasound-Powered Janus Micromotors*, *Advanced Functional Materials* **30**, 2004043 (2020).
74. X. Zhang, Q. Fu, H. Duan, J. Song, and H. Yang, *Janus Nanoparticles: From Fabrication to (Bio)Applications*, *ACS Nano* (2021).
75. F. Mou, C. Chen, H. Ma, Y. Yin, Q. Wu, and J. Guan, *Self-Propelled Micromotors Driven by the Magnesium–Water Reaction and Their Hemolytic Properties*, *Angewandte Chemie International Edition* **52**, 7208 (2013).
76. C. Chen et al., *Light-Steered Isotropic Semiconductor Micromotors*, *Advanced Materials* **29**, 1603374 (2017).
77. A. Boymelgreen, G. Yossifon, S. Park, and T. Miloh, *Spinning Janus Doublets Driven in Uniform AC Electric Fields*, *Phys. Rev. E* **89**, 011003 (2014).
78. M. Li and D. Li, *Fabrication and Electrokinetic Motion of Electrically Anisotropic Janus Droplets in Microchannels*, *ELECTROPHORESIS* **38**, 287 (2017).
79. M. Li and D. Li, *Janus Droplets and Droplets with Multiple Heterogeneous Surface Strips Generated with Nanoparticles under Applied Electric Field*, *J. Phys. Chem. C* **122**, 8461 (2018).
80. F. Ma, S. Wang, L. Smith, and N. Wu, *Two-Dimensional Assembly of Symmetric Colloidal Dimers under Electric Fields*, *Advanced Functional Materials* **22**, 4334 (2012).
81. A. F. Demirörs, P. M. Johnson, C. M. van Kats, A. van Blaaderen, and A. Imhof, *Directed Self-Assembly of Colloidal Dumbbells with an Electric Field*, *Langmuir* **26**, 14466 (2010).

82. M. M. Panczyk, J.-G. Park, N. J. Wagner, and E. M. Furst, *Two-Dimensional Directed Assembly of Dicolloids*, *Langmuir* **29**, 75 (2013).
83. I. D. Hosein, S. H. Lee, and C. M. Liddell, *Dimer-Based Three-Dimensional Photonic Crystals*, *Advanced Functional Materials* **20**, 3085 (2010).
84. S. Hernández-Navarro, J. Ignés-Mullol, F. Sagués, and P. Tierno, *Role of Anisotropy in Electrostatically Induced Colloidal Aggregates*, *Langmuir* **28**, 5981 (2012).
85. S. Wang, F. Ma, H. Zhao, and N. Wu, *Bulk Synthesis of Metal–Organic Hybrid Dimers and Their Propulsion under Electric Fields*, *ACS Appl. Mater. Interfaces* **6**, 4560 (2014).
86. C. L. Wirth and S. H. Nuthalapati, *Response of a Doublet to a Nearby Dc Electrode of Uniform Potential*, *Phys. Rev. E* **94**, 042614 (2016).
87. S. Ni, E. Marini, I. Buttinoni, H. Wolf, and L. Isa, *Rational Design and Fabrication of Versatile Active Colloidal Molecules*, arXiv:1701.08061.
88. U. Ohiri, C. W. Shields, K. Han, T. Tyler, O. D. Velev, and N. Jokerst, *Reconfigurable Engineered Motile Semiconductor Microparticles*, *Nat Commun* **9**, 1791 (2018).
89. Z. Wang, Z. Wang, J. Li, C. Tian, and Y. Wang, *Active Colloidal Molecules Assembled via Selective and Directional Bonds*, *Nat Commun* **11**, 2670 (2020).
90. X. Zhu, Y. Gao, R. Mhana, T. Yang, B. L. Hanson, X. Yang, J. Gong, and N. Wu, *Synthesis and Propulsion of Magnetic Dimers under Orthogonally Applied Electric and Magnetic Fields*, *Langmuir* **37**, 9151 (2021).
91. Y. Alapan, B. Yigit, O. Beker, A. F. Demirörs, and M. Sitti, *Shape-Encoded Dynamic Assembly of Mobile Micromachines*, *Nat. Mater.* **18**, 1244 (2019).
92. Z. Xiao, S. Duan, P. Xu, J. Cui, H. Zhang, and W. Wang, *Synergistic Speed Enhancement of an Electric-Photochemical Hybrid Micromotor by Tilt Rectification*, *ACS Nano* **14**, 8658 (2020).
93. Y.-L. Chen, C.-X. Yang, and H.-R. Jiang, *Electrically Enhanced Self-Thermophoresis of Laser-Heated Janus Particles under a Rotating Electric Field*, *Sci Rep* **8**, 5945 (2018).
94. A. Kirillova, C. Marschelke, and A. Synytska, *Hybrid Janus Particles: Challenges and Opportunities for the Design of Active Functional Interfaces and Surfaces*, *ACS Appl. Mater. Interfaces* **11**, 9643 (2019).
95. W. Gao, X. Feng, A. Pei, Y. Gu, J. Li, and J. Wang, *Seawater-Driven Magnesium Based Janus Micromotors for Environmental Remediation*, *Nanoscale* **5**, 4696 (2013).

96. Y. Komazaki, H. Hirama, and T. Torii, *Electrically and Magnetically Dual-Driven Janus Particles for Handwriting-Enabled Electronic Paper*, *Journal of Applied Physics* **117**, 154506 (2015).
97. L. Ren, D. Zhou, Z. Mao, P. Xu, T. J. Huang, and T. E. Mallouk, *Rheotaxis of Bimetallic Micromotors Driven by Chemical–Acoustic Hybrid Power*, *ACS Nano* **11**, 10591 (2017).
98. G. Celik Cogal, P. Kr. Das, S. Li, A. Uygun Oksuz, and V. R. Bhethanabotla, *Unraveling the Autonomous Motion of Polymer-Based Catalytic Micromotors Under Chemical–Acoustic Hybrid Power*, *Advanced NanoBiomed Research* **1**, 2000009 (2021).
99. S. Zhang et al., *Patterned Optoelectronic Tweezers: A New Scheme for Selecting, Moving, and Storing Dielectric Particles and Cells*, *Small* **14**, 1803342 (2018).
100. U. Choudhury, D. P. Singh, T. Qiu, and P. Fischer, *Chemical Nanomotors at the Gram Scale Form a Dense Active Optorheological Medium*, *Adv. Mater.* **31**, 1807382 (2019).
101. F. Mou, J. Zhang, Z. Wu, S. Du, Z. Zhang, L. Xu, and J. Guan, *Phototactic Flocking of Photochemical Micromotors*, *iScience* **19**, 415 (2019).
102. X. Peng, Z. Chen, P. S. Kollipara, Y. Liu, J. Fang, L. Lin, and Y. Zheng, *Opto-Thermoelectric Microswimmers*, *Light Sci Appl* **9**, 141 (2020).
103. N. H. P. Nguyen, D. Klotsa, M. Engel, and S. C. Glotzer, *Emergent Collective Phenomena in a Mixture of Hard Shapes through Active Rotation*, *Phys. Rev. Lett.* **112**, 075701 (2014).
104. M. Spellings, M. Engel, D. Klotsa, S. Sabrina, A. M. Drews, N. H. P. Nguyen, K. J. M. Bishop, and S. C. Glotzer, *Shape Control and Compartmentalization in Active Colloidal Cells*, *Proceedings of the National Academy of Sciences* **112**, E4642 (2015).
105. Z. Wang, Z. Wang, J. Li, S. T. H. Cheung, C. Tian, S.-H. Kim, G.-R. Yi, E. Ducrot, and Y. Wang, *Active Patchy Colloids with Shape-Tunable Dynamics*, *J. Am. Chem. Soc.* **141**, 14853 (2019).
106. R. Zhuang, D. Zhou, X. Chang, Y. Mo, G. Zhang, and L. Li, *Alternating Current Electric Field Driven Topologically Defective Micro/Nanomotors*, *Applied Materials Today* **26**, 101314 (2022).
107. P. Calvo-Marzal, S. Sattayasamitsathit, S. Balasubramanian, J. R. Windmiller, C. Dao, and J. Wang, *Propulsion of Nanowire Diodes*, *Chem. Commun.* **46**, 1623 (2010).
108. S. Park, L. Finkelman, and G. Yossifon, *Enhanced Cargo Loading of Electrically Powered Metallo-Dielectric Pollen Bearing Multiple Dielectrophoretic Traps*, *Journal of Colloid and Interface Science* **588**, 611 (2021).

109. D. Yamamoto, K. Kosugi, K. Hiramatsu, W. Zhang, A. Shioi, K. Kamata, T. Iyoda, and K. Yoshikawa, *Helical Micromotor Operating under Stationary DC Electrostatic Field*, *The Journal of Chemical Physics* **150**, 014901 (2019).
110. T. Qiu, T.-C. Lee, A. G. Mark, K. I. Morozov, R. Münster, O. Mierka, S. Turek, A. M. Leshansky, and P. Fischer, *Swimming by Reciprocal Motion at Low Reynolds Number*, *Nat Commun* **5**, 5119 (2014).
111. N. M. Diwakar, G. Kunti, T. Miloh, G. Yossifon, and O. D. Velev, *AC Electrohydrodynamic Propulsion and Rotation of Active Particles of Engineered Shape and Asymmetry*, *Current Opinion in Colloid & Interface Science* **59**, 101586 (2022).
112. K. Han, C. W. Shields, and O. D. Velev, *Engineering of Self-Propelling Microbots and Microdevices Powered by Magnetic and Electric Fields*, *Adv. Funct. Mater.* **28**, 1705953 (2018).
113. W. Wang, L. A. Castro, M. Hoyos, and T. E. Mallouk, *Autonomous Motion of Metallic Microrods Propelled by Ultrasound*, *ACS Nano* **6**, 6122 (2012).
114. W. F. Paxton, A. Sen, and T. E. Mallouk, *Motility of Catalytic Nanoparticles through Self-Generated Forces*, *Chemistry – A European Journal* **11**, 6462 (2005).
115. D. Kagan, S. Balasubramanian, and J. Wang, *Chemically Triggered Swarming of Gold Microparticles*, *Angewandte Chemie International Edition* **50**, 503 (2011).
116. N. Chaturvedi, Y. Hong, A. Sen, and D. Velegol, *Magnetic Enhancement of Phototaxing Catalytic Motors*, *Langmuir* **26**, 6308 (2010).
117. H. Ke, S. Ye, R. L. Carroll, and K. Showalter, *Motion Analysis of Self-Propelled Pt–Silica Particles in Hydrogen Peroxide Solutions*, *J. Phys. Chem. A* **114**, 5462 (2010).
118. D. P. Singh, W. E. Uspal, M. N. Popescu, L. G. Wilson, and P. Fischer, *Photogravitactic Microswimmers*, *Advanced Functional Materials* **28**, 1706660 (2018).
119. N. Mano and A. Heller, *Bioelectrochemical Propulsion*, *J. Am. Chem. Soc.* **127**, 11574 (2005).
120. D. Pantarotto, W. R. Browne, and B. L. Feringa, *Autonomous Propulsion of Carbon Nanotubes Powered by a Multienzyme Ensemble*, *Chem. Commun.* 1533 (2008).
121. D. Vilela, J. Parmar, Y. Zeng, Y. Zhao, and S. Sánchez, *Graphene-Based Microbots for Toxic Heavy Metal Removal and Recovery from Water*, *Nano Lett.* **16**, 2860 (2016).
122. C. Chen, E. Karshalev, J. Guan, and J. Wang, *Magnesium-Based Micromotors: Water-Powered Propulsion, Multifunctionality, and Biomedical and Environmental Applications*, *Small* **14**, 1704252 (2018).

123. R.-Y. Dong, Y. Zhang, K. Lou, and S. Granick, *Micromotor That Carries Its Own Fuel Internally*, *Langmuir* (2020).
124. A. Musin, R. Grynyov, M. Frenkel, and E. Bormashenko, *Self-Propulsion of a Metallic Superoleophobic Micro-Boat*, *Journal of Colloid and Interface Science* **479**, 182 (2016).
125. C. H. Ooi, A. van Nguyen, G. M. Evans, O. Gendelman, E. Bormashenko, and N.-T. Nguyen, *A Floating Self-Propelling Liquid Marble Containing Aqueous Ethanol Solutions*, *RSC Adv.* **5**, 101006 (2015).
126. C. Maggi, J. Simmchen, F. Saglimbeni, J. Katuri, M. Dipalo, F. De Angelis, S. Sanchez, and R. Di Leonardo, *Self-Assembly of Micromachining Systems Powered by Janus Micromotors*, *Small* **12**, 446 (2016).
127. W. Francis, C. Fay, L. Florea, and D. Diamond, *Self-Propelled Chemotactic Ionic Liquid Droplets*, *Chem. Commun.* **51**, 2342 (2015).
128. R. Sharma, S. T. Chang, and O. D. Velev, *Gel-Based Self-Propelling Particles Get Programmed To Dance*, *Langmuir* **28**, 10128 (2012).
129. Y.-J. Chen, Y. Nagamine, and K. Yoshikawa, *Self-Propelled Motion of a Droplet Induced by Marangoni-Driven Spreading*, *Phys. Rev. E* **80**, 016303 (2009).
130. J. L. Moran and J. D. Posner, *Phoretic Self-Propulsion*, *Annu. Rev. Fluid Mech.* **49**, 511 (2017).
131. U. M. Córdoba-Figueroa and J. F. Brady, *Osmotic Propulsion: The Osmotic Motor*, *Phys. Rev. Lett.* **100**, 158303 (2008).
132. G. F. Froment, K. B. Bischoff, and J. De Wilde, *Chemical Reactor Analysis and Design*, 3rd ed. (John Wiley & Sons, Inc., 2011).
133. A. S. Bartosik, *Advances in Numerical Heat Transfer and Fluid Flow*, *Energies* **17**, 2108 (2024).
134. E. M. Purcell, *Life at Low Reynolds-Number*, *Am. J. Phys.* **45**, 3 (1977).
135. A. A. Solovev, S. Sanchez, and O. G. Schmidt, *Collective Behaviour of Self-Propelled Catalytic Micromotors*, *Nanoscale* **5**, 1284 (2013).
136. W. Wang, W. Duan, S. Ahmed, A. Sen, and T. E. Mallouk, *From One to Many: Dynamic Assembly and Collective Behavior of Self-Propelled Colloidal Motors*, *Acc. Chem. Res.* **48**, 1938 (2015).
137. J. Bialké, T. Speck, and H. Löwen, *Active Colloidal Suspensions: Clustering and Phase Behavior*, *Journal of Non-Crystalline Solids* **407**, 367 (2015).

138. P. Illien, R. Golestanian, and A. Sen, *'Fuelled' Motion: Phoretic Motility and Collective Behaviour of Active Colloids*, Chem. Soc. Rev. **46**, 5508 (2017).
139. K. Villa, J. Viktorova, J. Plutnar, T. Ruml, L. Hoang, and M. Pumera, *Chemical Microrobots as Self-Propelled Microbrushes against Dental Biofilm*, Cell Reports Physical Science **1**, 100181 (2020).
140. A. A. Solovev, Y. Mei, E. Bermúdez Ureña, G. Huang, and O. G. Schmidt, *Catalytic Microtubular Jet Engines Self-Propelled by Accumulated Gas Bubbles*, Small **5**, 1688 (2009).
141. W. Z. Teo, H. Wang, and M. Pumera, *Beyond Platinum: Silver-Catalyst Based Bubble-Propelled Tubular Micromotors*, Chem. Commun. **52**, 4333 (2016).
142. B. E.-F. de Ávila et al., *Micromotor-Enabled Active Drug Delivery for in Vivo Treatment of Stomach Infection*, Nature Communications; London **8**, 1 (2017).
143. K. Liu et al., *Micromotor Based Mini-Tablet for Oral Delivery of Insulin*, ACS Nano (2022).
144. R. Mundaca-Urbe, E. Karshalev, B. E.-F. de Ávila, X. Wei, B. Nguyen, I. Litvan, R. H. Fang, L. Zhang, and J. Wang, *A Microstirring Pill Enhances Bioavailability of Orally Administered Drugs*, Advanced Science **n/a**, 2100389 (n.d.).
145. Y. Wang, R. M. Hernandez, D. J. Bartlett, J. M. Bingham, T. R. Kline, A. Sen, and T. E. Mallouk, *Bipolar Electrochemical Mechanism for the Propulsion of Catalytic Nanomotors in Hydrogen Peroxide Solutions*, Langmuir **22**, 10451 (2006).
146. M. Manjare, F. Yang, R. Qiao, and Y. Zhao, *Marangoni Flow Induced Collective Motion of Catalytic Micromotors*, J. Phys. Chem. C **119**, 28361 (2015).
147. S. Imamura and T. Kawakatsu, *Modeling of Chemically Active Particles at an Air–Liquid Interface*, Eur. Phys. J. E **44**, 127 (2021).
148. C. H. Meredith, A. C. Castonguay, Y.-J. Chiu, A. M. Brooks, P. G. Moerman, P. Torab, P. K. Wong, A. Sen, D. Velegol, and L. D. Zarzar, *Chemical Design of Self-Propelled Janus Droplets*, Matter **5**, 616 (2022).
149. Z. Izri, M. N. van der Linden, S. Michelin, and O. Dauchot, *Self-Propulsion of Pure Water Droplets by Spontaneous Marangoni-Stress-Driven Motion*, Phys. Rev. Lett. **113**, 248302 (2014).
150. W. Duan, R. Liu, and A. Sen, *Transition between Collective Behaviors of Micromotors in Response to Different Stimuli*, J. Am. Chem. Soc. **135**, 1280 (2013).

151. F. Mou, X. Li, Q. Xie, J. Zhang, K. Xiong, L. Xu, and J. Guan, *Active Micromotor Systems Built from Passive Particles with Biomimetic Predator–Prey Interactions*, ACS Nano **14**, 406 (2020).
152. I. Theurkauff, C. Cottin-Bizonne, J. Palacci, C. Ybert, and L. Bocquet, *Dynamic Clustering in Active Colloidal Suspensions with Chemical Signaling*, Phys. Rev. Lett. **108**, 268303 (2012).
153. A. A. Solovev, Y. Mei, and O. G. Schmidt, *Catalytic Microstrider at the Air–Liquid Interface*, Advanced Materials **22**, 4340 (2010).
154. M. P. Kummer, J. J. Abbott, B. E. Kratochvil, R. Borer, A. Sengul, and B. J. Nelson, *OctoMag: An Electromagnetic System for 5-DOF Wireless Micromanipulation*, IEEE Transactions on Robotics **26**, 1006 (2010).
155. C. Gao, Y. Wang, Z. Ye, Z. Lin, X. Ma, and Q. He, *Biomedical Micro-/Nanomotors: From Overcoming Biological Barriers to In Vivo Imaging*, Advanced Materials **n/a**, 2000512 (n.d.).
156. J. Wang, Z. Xiong, J. Zheng, X. Zhan, and J. Tang, *Light-Driven Micro/Nanomotor for Promising Biomedical Tools: Principle, Challenge, and Prospect*, Acc. Chem. Res. **51**, 1957 (2018).
157. R. Pu, X. Yang, H. Mu, Z. Xu, and J. He, *Current Status and Future Application of Electrically Controlled Micro/Nanorobots in Biomedicine*, Front Bioeng Biotechnol **12**, 1353660 (2024).
158. H. Eskandarloo, A. Kierulf, and A. Abbaspourrad, *Nano- and Micromotors for Cleaning Polluted Waters: Focused Review on Pollutant Removal Mechanisms*, Nanoscale **9**, 13850 (2017).
159. J. Li, V. V. Singh, S. Sattayasamitsathit, J. Orozco, K. Kaufmann, R. Dong, W. Gao, B. Jurado-Sanchez, Y. Fedorak, and J. Wang, *Water-Driven Micromotors for Rapid Photocatalytic Degradation of Biological and Chemical Warfare Agents*, ACS Nano **8**, 11118 (2014).
160. B. Jurado-Sánchez, S. Sattayasamitsathit, W. Gao, L. Santos, Y. Fedorak, V. V. Singh, J. Orozco, M. Galarnyk, and J. Wang, *Self-Propelled Activated Carbon Janus Micromotors for Efficient Water Purification*, Small **11**, 499 (2015).
161. H. Ge, X. Chen, W. Liu, X. Lu, and Z. Gu, *Metal-Based Transient Micromotors: From Principle to Environmental and Biomedical Applications*, Chemistry – An Asian Journal **14**, 2348 (2019).
162. W. Z. Teo, R. Zboril, I. Medrik, and M. Pumera, *FeO Nanomotors in Ton Quantities (1020 Units) for Environmental Remediation*, Chemistry – A European Journal **22**, 4789 (2016).
163. A. B. Pawar and I. Kretzschmar, *Fabrication, Assembly, and Application of Patchy Particles*, Macromolecular Rapid Communications **31**, 150 (2010).

164. L. C. Bradley, K. J. Stebe, and D. Lee, *Clickable Janus Particles*, J. Am. Chem. Soc. **138**, 11437 (2016).
165. S. Rahmani, S. Saha, H. Durmaz, A. Donini, A. C. Misra, J. Yoon, and J. Lahann, *Chemically Orthogonal Three-Patch Microparticles*, Angewandte Chemie International Edition **53**, 2332 (2014).
166. A. M.Boymelgreen, G. Kunti, P. Garcia-Sanchez, A. Ramos, G. Yossifon, and T. Miloh, *The Role of Particle-Electrode Wall Interactions in Mobility of Active Janus Particles Driven by Electric Fields*, Journal of Colloid and Interface Science **616**, 465 (2022).
167. N. M. Diwakar, G. Kunti, T. Miloh, G. Yossifon, and O. D. Velev, *AC Electrohydrodynamic Propulsion and Rotation of Active Particles of Engineered Shape and Asymmetry*, Current Opinion in Colloid & Interface Science **59**, 101586 (2022).
168. O. D. Lavrentovich, I. Lazo, and O. P. Pishnyak, *Nonlinear Electrophoresis of Dielectric and Metal Spheres in a Nematic Liquid Crystal*, Nature **467**, 7318 (2010).
169. T. Miloh and J. Nagler, *Electrorotation of Leaky-Dielectric and Conducting Microspheres in Asymmetric Electrolytes and Angular Velocity Reversal*, ELECTROPHORESIS **41**, 1296 (2020).
170. A. Hashemi, S. C. Bukosky, S. P. Rader, W. D. Ristenpart, and G. H. Miller, *Oscillating Electric Fields in Liquids Create a Long-Range Steady Field*, Phys. Rev. Lett. **121**, 185504 (2018).
171. O. Kedem, B. Lau, and E. A. Weiss, *Mechanisms of Symmetry Breaking in a Multidimensional Flashing Particle Ratchet*, ACS Nano **11**, 7148 (2017).
172. L. Gorre-Talini, J. P. Spatz, and P. Silberzan, *Dielectrophoretic Ratchets*, Chaos **8**, 650 (1998).
173. A. Kale, X. Lu, S. Patel, and X. Xuan, *Continuous-Flow Dielectrophoretic Trapping and Patterning of Colloidal Particles in a Ratchet Microchannel*, J. Micromech. Microeng. **24**, 075007 (2014).
174. X. Xiao, V. F. Geyer, H. Bowne-Anderson, J. Howard, and I. F. Sbalzarini, *Automatic Optimal Filament Segmentation with Sub-Pixel Accuracy Using Generalized Linear Models and B-Spline Level-Sets*, Medical Image Analysis **32**, 157 (2016).
175. R. Fernández-Mateo, P. García-Sánchez, V. Calero, H. Morgan, and A. Ramos, *Stationary Electro-Osmotic Flow Driven by AC Fields around Charged Dielectric Spheres*, Journal of Fluid Mechanics **924**, (2021).
176. F. Katzmeier and F. C. Simmel, *Microrobots Powered by Concentration Polarization Electrophoresis (CPEP)*, Nat Commun **14**, 6247 (2023).

177. D. C. Prieve, J. L. Anderson, J. P. Ebel, and M. E. Lowell, *Motion of a Particle Generated by Chemical Gradients. Part 2. Electrolytes*, *Journal of Fluid Mechanics* **148**, 247 (1984).
178. M. R. Spiegel and L. J. Stephens, *Schaum's Outline of Statistics, 6th Edition* (McGraw-Hill Education, 2018).
179. D. Ben-Bassat, A. Boymelgreen, and G. Yossifon, *The Influence of Flow Intensity and Field Frequency on Continuous-Flow Dielectrophoretic Trapping*, *Journal of Colloid and Interface Science* **442**, 154 (2015).
180. A. Barnaveli and R. van Roij, *Asymmetric Rectified Electric Fields for Symmetric Electrolytes*, *Langmuir* (2024).
181. H. Morgan and N. G. Green, *AC Electrokinetics: Colloids and Nanoparticles* (Research Studies Press Ltd., Baldock, 2003).
182. A. Castellanos, A. Ramos, A. González, N. G. Green, and H. Morgan, *Electrohydrodynamics and Dielectrophoresis in Microsystems: Scaling Laws*, *J. Phys. D: Appl. Phys.* **36**, 2584 (2003).
183. A. S. Dukhin and S. S. Dukhin, *Aperiodic Capillary Electrophoresis Method Using an Alternating Current Electric Field for Separation of Macromolecules*, *ELECTROPHORESIS* **26**, 2149 (2005).
184. A. S. Khair, *Nonlinear Electrophoresis of Colloidal Particles*, *Current Opinion in Colloid & Interface Science* **59**, 101587 (2022).
185. N. A. Mishchuk and N. O. Barinova, *Theoretical and Experimental Study of Nonlinear Electrophoresis*, *Colloid J* **73**, 88 (2011).
186. S. M. Kontush, *Aperiodic Electrophoresis*, *Colloid J. USSR* **56**, (1994).
187. S. S. Dukhin and N. A. Mishchuk, *High-Voltage Pulse Electrophoresis*, *Colloid J.* **50**, (1988).
188. A. Shibata, K. Komiya, K. Watanabe, T. Sato, T. Shiomi, H. Kotaki, P. J. Schuele, M. A. Crowder, C. Zhan, and J. W. Hartzell, *Bidirectional Migration of Au Colloids and Silicon Microrods in Liquid Using Asymmetrical Alternating Current Electric Field with Insulated Electrodes*, *Jpn. J. Appl. Phys.* **53**, 027301 (2014).
189. A. Hashemi, M. Tahernia, W. D. Ristenpart, and G. H. Miller, *Controlling the Direction of Steady Electric Fields in Liquid Using Nonantiperiodic Potentials*, *Phys. Rev. E* **107**, 054608 (2023).

190. F. Leermakers, J. C. Eriksson, and H. Lyklema, *Chapter 4 - Association Colloids and Their Equilibrium Modelling*, in *Fundamentals of Interface and Colloid Science*, edited by J. Lyklema, Vol. 5 (Academic Press, 2005), p. 4.1-4.123.
191. L. Rozitsky, A. Fine, D. Dado, S. Nussbaum-Ben-Shaul, S. Levenberg, and G. Yossifon, *Quantifying Continuous-Flow Dielectrophoretic Trapping of Cells and Micro-Particles on Micro-Electrode Array*, *Biomed Microdevices* **15**, 859 (2013).
192. R. H. Ottewill and J. N. Shaw, *Electrophoretic Studies on Polystyrene Latices*, *Journal of Electroanalytical Chemistry and Interfacial Electrochemistry* **37**, 133 (1972).
193. V. Calero, R. Fernández-Mateo, H. Morgan, P. García-Sánchez, and A. Ramos, *Stationary Electro-Osmotic Flow Driven by Ac Fields around Insulators*, *Phys. Rev. Appl.* **15**, 014047 (2021).
194. M. Ammam and J. Fransaer, *Effects of AC-Electrolysis on the Enzymatic Activity of Glucose Oxidase*, *Electroanalysis* **23**, 755 (2011).
195. R. Mundaca-Urbe, E. Karshalev, B. Esteban-Fernández de Ávila, X. Wei, B. Nguyen, I. Litvan, R. H. Fang, L. Zhang, and J. Wang, *A Microstirring Pill Enhances Bioavailability of Orally Administered Drugs*, *Adv Sci (Weinh)* **8**, 2100389 (2021).
196. S. Ebbens, D. A. Gregory, G. Dunderdale, J. R. Howse, Y. Ibrahim, T. B. Liverpool, and R. Golestanian, *Electrokinetic Effects in Catalytic Platinum-Insulator Janus Swimmers*, *EPL* **106**, 58003 (2014).
197. T. Chen, Y. Jiang, C. Wang, Z. Cai, H. Chen, J. Zhu, P. Tao, and M. Wu, *The pH-Triggered Drug Release and Simultaneous Carrier Decomposition of Effervescent SiO₂-Drug-Na₂CO₃ Composite Nanoparticles: To Improve the Antitumor Activity of Hydrophobic Drugs*, *RSC Adv.* **11**, 5335 (2021).
198. J. D. Eichman and J. R. Robinson, *Mechanistic Studies on Effervescent-Induced Permeability Enhancement*, *Pharm Res* **15**, 925 (1998).
199. M. Lambros, T. (Henry) Tran, Q. Fei, and M. Nicolaou, *Citric Acid: A Multifunctional Pharmaceutical Excipient*, *Pharmaceutics* **14**, 972 (2022).
200. N. P. Nghiem, S. Kleff, and S. Schwegmann, *Succinic Acid: Technology Development and Commercialization*, *Fermentation* **3**, 2 (2017).
201. L. E. Scriven and C. V. Sternling, *The Marangoni Effects*, *Nature* **187**, 186 (1960).
202. H. Kim, K. Muller, O. Shardt, S. Afkhami, and H. A. Stone, *Solutal Marangoni Flows of Miscible Liquids Drive Transport without Surface Contamination*, *Nature Phys* **13**, 1105 (2017).

203. D. G. Suci, O. Smigelschi, and E. Ruckenstein, *The Spreading of Liquids on Liquids*, *Journal of Colloid and Interface Science* **33**, 520 (1970).
204. S. Mahiuddin, B. Minofar, J. M. Borah, M. R. Das, and P. Jungwirth, *Propensities of Oxalic, Citric, Succinic, and Maleic Acids for the Aqueous Solution/Vapour Interface: Surface Tension Measurements and Molecular Dynamics Simulations*, *Chemical Physics Letters* **462**, 217 (2008).
205. L. Chen, Z. He, K. Kunnath, K. Zheng, S. Kim, and R. N. Davé, *Fine Grade Engineered Microcrystalline Cellulose Excipients for Direct Compaction: Assessing Suitability of Different Dry Coating Processes*, *European Journal of Pharmaceutical Sciences* **151**, 105408 (2020).
206. G. Thoorens, F. Krier, B. Leclercq, B. Carlin, and B. Evrard, *Microcrystalline Cellulose, a Direct Compression Binder in a Quality by Design Environment—A Review*, *International Journal of Pharmaceutics* **473**, 64 (2014).
207. H. Zhao, L. Zhao, X. Lin, and L. Shen, *An Update on Microcrystalline Cellulose in Direct Compression: Functionality, Critical Material Attributes, and Co-Processed Excipients*, *Carbohydrate Polymers* **278**, 118968 (2022).
208. S. Yassin, D. J. Goodwin, A. Anderson, J. Sibik, D. I. Wilson, L. F. Gladden, and J. A. Zeitler, *The Disintegration Process in Microcrystalline Cellulose Based Tablets, Part I: Influence of Temperature, Porosity and Superdisintegrants*, *J Pharm Sci* **104**, 3440 (2015).
209. P. Hiemenz and R. Rajagopalan, *Principles of Colloid and Surface Chemistry*, 3rd, Revised and Expanded ed. (CRC Press, Boca Raton, 1977).
210. S. Bobroff, R. J. Phillips, and A. Shekarriz, *Nuclear Magnetic Resonance Measurement of Ammonia Diffusion in Dense Solid-Liquid Slurries*, United States **Revision 1**, (n.d.).
211. R. E. Zeebe, *On the Molecular Diffusion Coefficients of Dissolved CO₂, HCO₃⁻, and CO₃²⁻ and Their Dependence on Isotopic Mass*, *Geochimica et Cosmochimica Acta* **75**, 2483 (2011).
212. G. T. A. Müller and R. H. Stokes, *The Mobility of the Undissociated Citric Acid Molecule in Aqueous Solution*, *Trans. Faraday Soc.* **53**, 642 (1957).
213. O. Schnitzer and E. Yariv, *Nonlinear Electrophoresis at Arbitrary Field Strengths: Small-Dukhin-Number Analysis*, *Physics of Fluids* **26**, 122002 (2014).
214. S. Gangwal, A. Pawar, I. Kretschmar, and O. D. Velev, *Programmed Assembly of Metallodielectric Patchy Particles in External AC Electric Fields*, *Soft Matter* **6**, 1413 (2010).
215. M. S. Kilic and M. Z. Bazant, *Induced-charge electrophoresis near a wall*, *ELECTROPHORESIS* **32**, 614 (2011).

216. M. F. Khanfar, W. Al-Faqheri, and A. Al-Halhouli, *Low Cost Lab on Chip for the Colorimetric Detection of Nitrate in Mineral Water Products*, *Sensors (Basel)* **17**, 2345 (2017).
217. C. W. Bae, P. T. Toi, B. Y. Kim, W. I. Lee, H. B. Lee, A. Hanif, E. H. Lee, and N.-E. Lee, *Fully Stretchable Capillary Microfluidics-Integrated Nanoporous Gold Electrochemical Sensor for Wearable Continuous Glucose Monitoring*, *ACS Appl Mater Interfaces* **11**, 14567 (2019).
218. A. Cazalé, W. Sant, F. Ginot, J.-C. Launay, G. Savourey, F. Revol-Cavalier, J. M. Lagarde, D. Henry, J. Launay, and P. Temple-Boyer, *Physiological Stress Monitoring Using Sodium Ion Potentiometric Microsensors for Sweat Analysis*, *Sensors and Actuators B: Chemical* **225**, 1 (2016).
219. S. Anastasova, B. Crewther, P. Bembnowicz, V. Curto, H. M. Ip, B. Rosa, and G.-Z. Yang, *A Wearable Multisensing Patch for Continuous Sweat Monitoring*, *Biosensors and Bioelectronics* **93**, 139 (2017).
220. A. Gonzalez, L. Estala, M. Gaines, and F. A. Gomez, *Mixed Thread/Paper-Based Microfluidic Chips as a Platform for Glucose Assays*, *ELECTROPHORESIS* **37**, 1685 (2016).
221. D. S. Dkhar, R. Kumari, S. J. Malode, N. P. Shetti, and P. Chandra, *Integrated Lab-on-a-Chip Devices: Fabrication Methodologies, Transduction System for Sensing Purposes*, *Journal of Pharmaceutical and Biomedical Analysis* **223**, 115120 (2023).
222. S. Yang and J. D. Zahn, *Lab-on-a-Chip Devices for Particle and Cell Separation*, in *Encyclopedia of Microfluidics and Nanofluidics*, edited by D. Li (Springer US, Boston, MA, 2008), pp. 930–940.
223. S. Ahmed and J. Perez-Mercader, *Autonomous Low-Reynolds-Number Soft Robots with Structurally Encoded Motion and Their Thermodynamic Efficiency*, *Langmuir* **37**, 8148 (2021).
224. H. Xu, M. Medina-Sánchez, V. Magdanz, L. Schwarz, F. Hebenstreit, and O. G. Schmidt, *Sperm-Hybrid Micromotor for Targeted Drug Delivery*, *ACS Nano* **12**, 327 (2018).
225. É. O’Neel-Judy, D. Nicholls, J. Castañeda, and J. G. Gibbs, *Light-Activated, Multi-Semiconductor Hybrid Microswimmers*, *Small* **14**, 1801860 (2018).
226. C. J. Martin, G. Rapenne, T. Nakashima, and T. Kawai, *Recent Progress in Development of Photoacid Generators*, *Journal of Photochemistry and Photobiology C: Photochemistry Reviews* **34**, 41 (2018).
227. N. A. Kuznetsova, G. V. Malkov, and B. G. Gribov, *Photoacid Generators. Application and Current State of Development*, *Russ. Chem. Rev.* **89**, 173 (2020).
228. T. Sun, L. Kang, H. Zhao, Y. Zhao, and Y. Gu, *Photoacid Generators for Biomedical Applications*, *Advanced Science* **11**, 2302875 (2024).

229. X. Liu, K. Sambath, L. Hutnik, J. Du, K. D. Belfield, and Y. Zhang, *Activating Acid-Sensing Ion Channels with Photoacid Generators*, *ChemPhotoChem* **4**, 5337 (2020).
230. B. S. Atiyeh, S. A. Dibo, and S. N. Hayek, *Wound Cleansing, Topical Antiseptics and Wound Healing*, *Int Wound J* **6**, 420 (2009).
231. Y. Mori, G. Nakagami, A. Kitamura, T. Minematsu, M. Kinoshita, H. Suga, M. Kurita, C. Hayashi, A. Kawasaki, and H. Sanada, *Effectiveness of Biofilm-Based Wound Care System on Wound Healing in Chronic Wounds*, *Wound Repair and Regeneration* **27**, 540 (2019).
232. X. Shen, L. Dong, X. He, C. Zhao, W. Zhang, X. Li, and Y. Lu, *Treatment of Infected Wounds with Methylene Blue Photodynamic Therapy: An Effective and Safe Treatment Method*, *Photodiagnosis and Photodynamic Therapy* **32**, 102051 (2020).
233. Q. D. Ngo, K. Vickery, and A. K. Deva, *The Effect of Topical Negative Pressure on Wound Biofilms Using an in Vitro Wound Model*, *Wound Repair and Regeneration* **20**, 83 (2012).
234. G. Nakagami, T. Morohoshi, T. Ikeda, Y. Ohta, H. Sagara, L. Huang, T. Nagase, J. Sugama, and H. Sanada, *Contribution of Quorum Sensing to the Virulence of Pseudomonas Aeruginosa in Pressure Ulcer Infection in Rats*, *Wound Repair Regen* **19**, 214 (2011).
235. J. L. Del Pozo, *Biofilm-Related Disease*, *Expert Rev Anti Infect Ther* **16**, 51 (2018).
236. R. F. Donnelly, P. A. McCarron, and A. D. Woolfson, *Derivatives of 5-Aminolevulinic Acid for Photodynamic Therapy*, *Perspect Medicin Chem* **1**, 49 (2007).
237. F. Harris and L. Pierpoint, *Photodynamic Therapy Based on 5-Aminolevulinic Acid and Its Use as an Antimicrobial Agent*, *Medicinal Research Reviews* **32**, 1292 (2012).
238. K. Inoue, *5-Aminolevulinic Acid-Mediated Photodynamic Therapy for Bladder Cancer*, *International Journal of Urology* **24**, 97 (2017).
239. K. Mahmoudi, K. L. Garvey, A. Bouras, G. Cramer, H. Stepp, J. G. Jesu Raj, D. Bozec, T. M. Busch, and C. G. Hadjipanayis, *5-Aminolevulinic Acid Photodynamic Therapy for the Treatment of High-Grade Gliomas*, *J Neurooncol* **141**, 595 (2019).
240. C. Zhang, T. Gong, J. Wang, A. Chou, and J. J. Jiang, *Topical Application of 5-Aminolevulinic Acid Is Sufficient for Photodynamic Therapy on Vocal Folds*, *The Laryngoscope* **129**, E80 (2019).
241. T. Cwalinski, W. Polom, L. Marano, G. Roviello, A. D'Angelo, N. Cwalina, M. Matuszewski, F. Roviello, J. Jaskiewicz, and K. Polom, *Methylene Blue—Current Knowledge, Fluorescent Properties, and Its Future Use*, *J Clin Med* **9**, 3538 (2020).
242. M. Pourhajibagher, N. Chiniforush, R. Raoofian, B. Pourakbari, R. Ghorbanzadeh, F. Bazarjani, and A. Bahador, *Evaluation of Photo-Activated Disinfection Effectiveness with*

Methylene Blue against Porphyromonas Gingivalis Involved in Endodontic Infection: An in Vitro Study, *Photodiagnosis and Photodynamic Therapy* **16**, 132 (2016).

243. C.-Y. Su, M. W. Hughes, T.-Y. Liu, C.-M. Chuong, H.-V. Wang, and W.-C. Yang, *Defining Wound Healing Progression in Cetacean Skin: Characteristics of Full-Thickness Wound Healing in Fraser's Dolphins (Lagenodelphis Hosei)*, *Animals (Basel)* **12**, 537 (2022).

244. M. Seaton, A. Hocking, and N. S. Gibran, *Porcine Models of Cutaneous Wound Healing*, *ILAR Journal* **56**, 127 (2015).

APPENDICES

Appendix A

Numerical simulations of the electroconvection around a charged dielectric particle

Here a simplified numerical simulation of the electroconvection around a charged dielectric particle was performed via a fully coupled, two-dimensional (2D) axisymmetric cylindrical coordinate system, time-dependent model, using the finite-element based software COMSOL (V5.3). The governing equations in the system are the continuity of ions, c_i , expressed using the Nernst–Planck relation for the ion fluxes, \mathbf{j}_i , while negating the convective contribution (assuming a small Peclet number $\ll 1$)

$$\frac{\partial c_{\pm}}{\partial t} = -\nabla \cdot \mathbf{j}_i, \quad \mathbf{j}_i = -(D_i \nabla c_i + Z_i \frac{F}{RT} D_i c_i \nabla \phi), \quad (1)$$

the Poisson equation for the electric potential, ϕ , in terms of the excess ionic charge density, ρ_e

$$-\nabla \cdot (\epsilon \nabla \phi) = \rho_e; \quad \rho_e = F \sum_i Z_i c_i, \quad (2)$$

and the incompressible Stokes equations for solving the velocity field \mathbf{u} and pressure p

$$-\nabla p + \eta \nabla^2 \mathbf{u} + \mathbf{f}_E = 0, \quad \nabla \cdot \mathbf{u} = 0, \quad (3)$$

including the Columbic volumetric electrical forcing

$$\mathbf{f}_E = \rho_e \mathbf{E} = -\rho_e \nabla \phi. \quad (4)$$

Herein, F is the Faraday constant, R is the universal gas constant, T is the temperature, ε is the permittivity of water and η is the dynamic viscosity of water. We use $z_+ = -z_- = 1$ for the ionic valence and $D_+ = D_- = D = 5.3 \cdot 10^{-9} \text{ m}^2 \text{ s}^{-1}$ for the effective diffusion coefficient of deionized water (DI) [179] and conductivity of $\sigma \sim 0.1 \text{ } \mu\text{S/cm}$.

A simple two-dimensional geometry was used to model the experimental setup; consisting of a rectangular channel, $50 \text{ } \mu\text{m}$ height and $25 \text{ } \mu\text{m}$ radial dimension, with a $10 \text{ } \mu\text{m}$ diameter half circle at the center. At the radial outer surface of the rectangular domain an insulating condition is applied, while at the left and right side walls along the z -coordinate an oscillating electric potential of a sawtooth form is applied with an amplitude of $V_0/2$. The particle surface is assumed to have a uniform surface charge that is equivalent to a zeta potential of -100 mV .

Figures 1 and 2 describe the time-dependent normalized velocity as well as the induced ionic concentration-polarization around the cylindrical particle upon a step-wise application of a sawtooth shaped applied potential in forward and reverse modes, respectively. Interestingly, due to the ramping of the signal there is a residual ionic concentration-polarization with a time-averaged gradient of opposite direction for the forward and reverse signals. Figure 3 shows that the mobility decays with decreasing particle's zeta potential which further supports the hypothesis that the effect results from the dominating surface conductance.

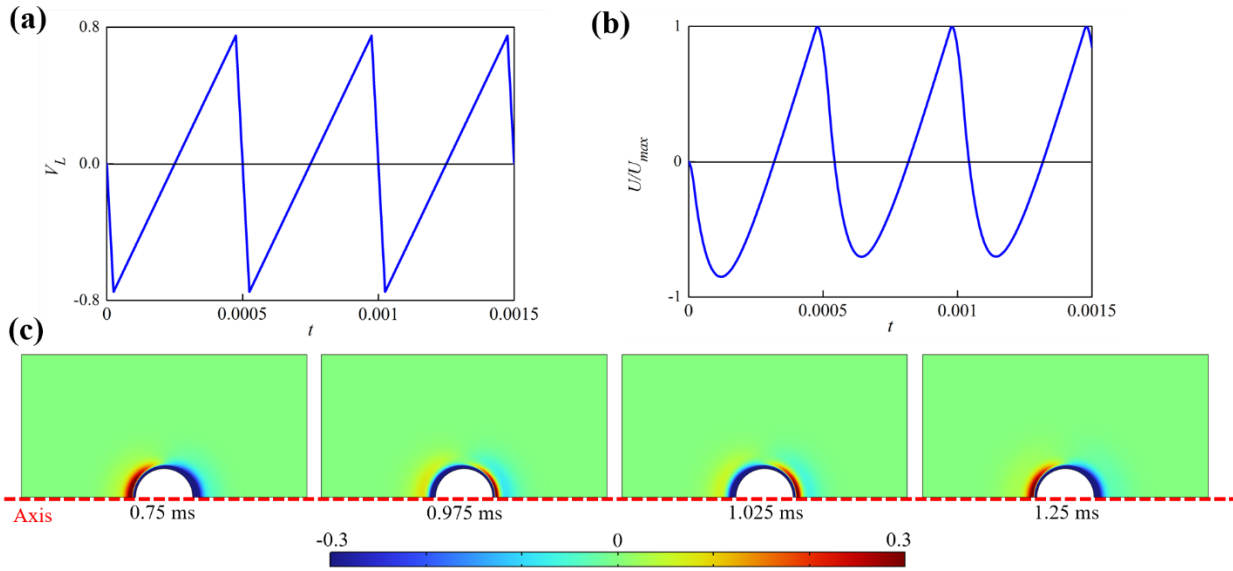


Figure 1: Simulation with **a)** an applied periodic sawtooth shaped potential on the left side wall with a signal asymmetry of 0.4. **b)** The transient cross-sectional average velocity, U/U_{max} normalized by its maximal value, that is generated relative to a fixed cylinder. **c)** The time-dependent induced ionic concentration-polarization, $(c_- - c_0)/c_0$, that is generated due to surface conductance.

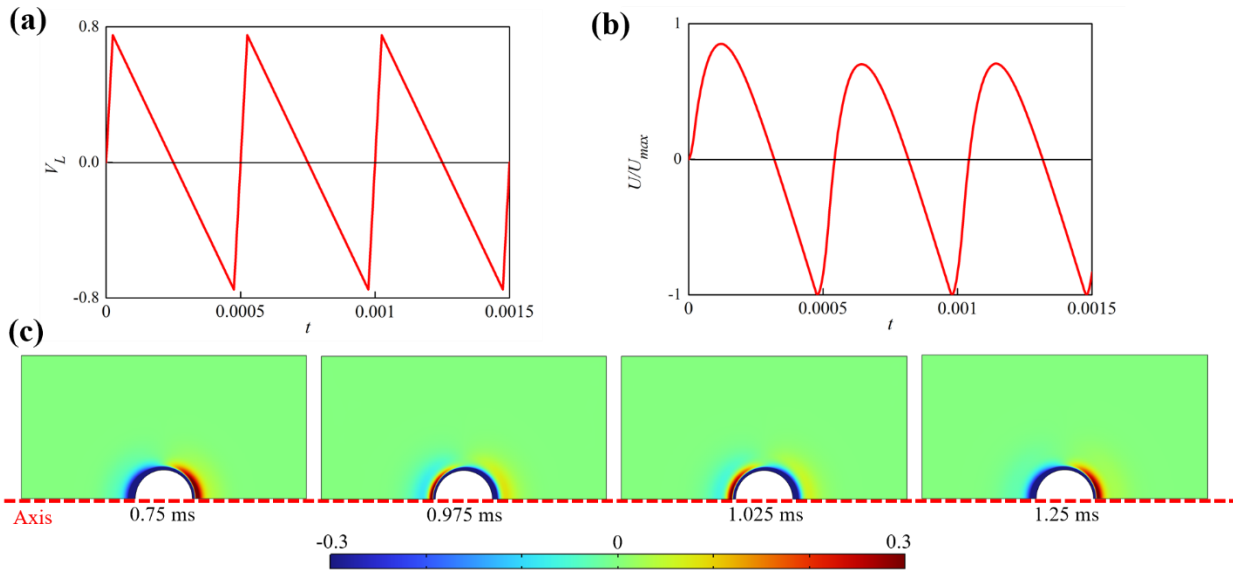


Figure 2: Same type of simulation as in Figure 1 above but for a time-reversed signal.

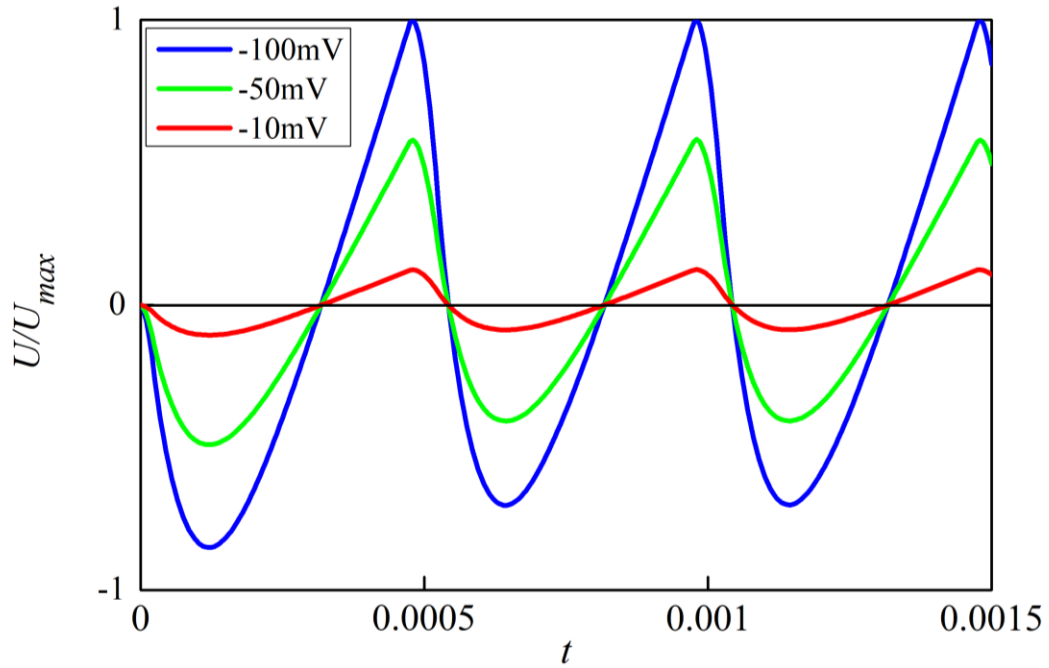


Figure 3: The transient cross-sectional average velocity, U/U_{max} normalized by its maximal value, that is generated relative to a fixed cylinder for varying particle surface's zeta potentials. Here, a signal asymmetry of 0.4 was used.

Appendix B

Theoretical analysis – mobility as a function of asymmetry

We present a simple linearized transient model corresponding to the mobility of charged symmetric dielectric spherical microparticles under an asymmetric triangular AC electric field. Our aim is to discuss the mobility reversal of free dielectric particles in the low-frequency region by taking into account the effect of surface conductance and concentration polarization assuming a weak field and thin EDL [175]. In particular, we consider the following two forms (“forward” and “reverse”) of an oscillating electric field of triangular-type of period T and characteristic time t_1 ($0 < t_1 < T/4$) possessing a zero time-average over a single period, such that $t_1 = 0$ describes an asymmetric sawtooth and $t_1 = T/4$ a symmetric triangular signal (see Figure 1). The two forms $F_{\pm}(t, t_1)$ of unit amplitude are defined over a time (t) interval $T > t > 0$ as

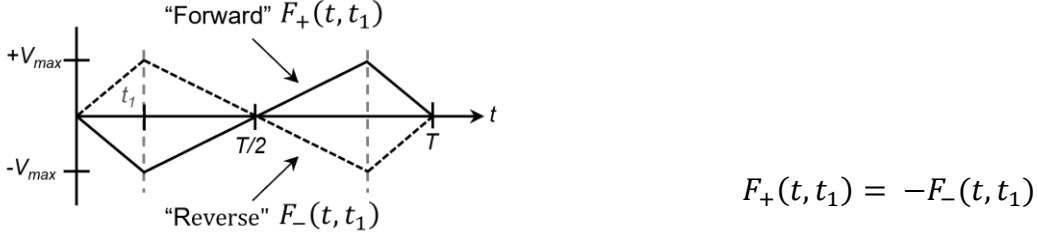


Figure 1: Schematic for definition of a triangular-type AC signal.

where $F_-(t, 0)$ corresponds to the “reverse” and $F_+(t, 0)$ to “forward” sawtooth forms depicted in Figure 1. The time asymmetry parameter for the “reverse” signal is defined as $2\lambda = 4t_1/T - 1$ and for the “forward” signal as $2\lambda = 1 - 4t_1/T$, such that $\lambda = 1/2$ ($t_1 = 0$) represents a “forward” sawtooth signal and $\lambda = -1/2$ a “reverse” sawtooth signal (see Figure 2).

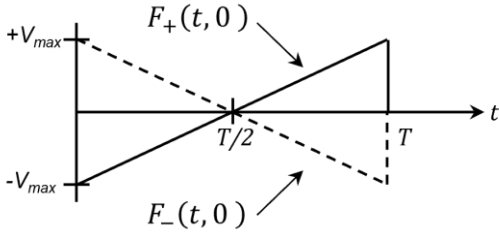


Figure 2: A sawtooth signal corresponding to $t_1 = 0$.

and the value of $\lambda = 0$ ($t_1 = T/4$) corresponds to the following symmetric triangular signal (see Figure 3).

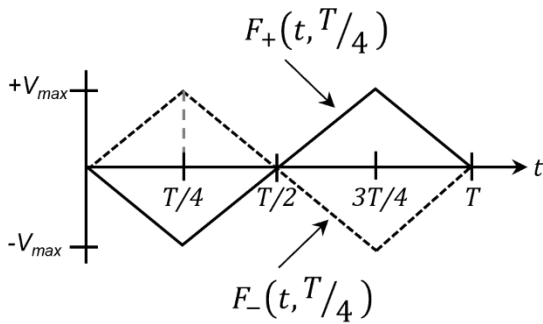


Figure 3: A triangular signal corresponding to $t_1 = T/4$.

Laplace Transform

The Laplace transform (LT) of the asymmetric triangular signal $F_{\pm}(t, t_1)$ can be expressed in terms of the ramp function $tu(t)$ where $u(t)$ denotes the Heaviside function $u(t) = 1$ for $t > 0$. For example, for the “reverse” waveform, one gets:

$$F_-(t, t_1) = \frac{t}{t_1} [u(t) - u(t - t_1)] + \frac{T-2t}{T-2t_1} [u(t - t_1) - u(t - T + t_1)] + \frac{t-T}{t_1} [u(t - T + t_1) - u(t - T)], \quad (1)$$

or, after collecting terms:

$$F_-(t, t_1) = \frac{1}{t_1} \left[tu(t) - \frac{T(t-t_1)}{T-2t_1} u(t-t_1) + \frac{T(t-T+t_1)}{T-2t_1} u(t-T+t_1) - (t-T)u(t-T) \right]. \quad (2)$$

Defining the LT of $F(t, t_1)$ as $\tilde{F}(s, t_1)$, where s denotes the usual complex frequency parameter, one readily finds from eq. (2):

$$\tilde{F}_-(s, t_1) = \frac{1}{t_1 s^2} \left[1 - \frac{T}{T-2t_1} (e^{-st_1} - e^{-s(T-t_1)}) - e^{-sT} \right]. \quad (3)$$

Note that for $t_1 = 0$, eq. (3) reduces to the well-known LT of a sawtooth signal, namely:

$$\tilde{F}_-(s, t_1 \rightarrow 0) = \frac{1}{s} (1 + e^{-sT}) - \frac{2}{s^2 T} (1 - e^{-sT}). \quad (4)$$

It is also important to note that the average of $F_{\pm}(t, t_1)$ over a single period can be evaluated as:

$$\frac{1}{T} \int_0^T F_{\pm}(t, t_1) dt = \frac{1}{T} \mathcal{L}^{-1} \left[\frac{\tilde{F}_{\pm}(s, t_1)}{s} \right] \Big|_{s=T}, \quad (5)$$

where \mathcal{L}^{-1} (the inverse LT) in eq. (5) is null as expected, since following eq. (3):

$$\begin{aligned} \mathcal{L}^{-1} \left[\frac{\tilde{F}_-(s, t_1)}{s} \right] &= \frac{1}{2t_1} \left[t^2 u(t) - \frac{T(t-t_1)^2}{T-2t_1} u(t-t_1) + \frac{T}{T-2t_1} (t-T+t_1)^2 u(t-T+t_1) - \right. \\ &\quad \left. (t-T)^2 u(t-T) \right] \Big|_{t=T} = 0. \end{aligned} \quad (6)$$

Transient Mobility

The periodic asymmetric triangular waveforms depicted in Figure 1 have two timescales; a long timescale connected with the period $T = 2\pi/\omega$ of its AC nature and a short timescale $\tau \ll T$ associated with the instantaneous (sign) change of the field gradient occurring twice during a single cycle. Expressed in a spherical coordinate system preserving axial symmetry (r, θ) , where r is the radial distance normalized with respect to the radius a , the transient (short-time) electric field and solute concentration (defined over a single period) are given by $\varphi(r, \theta; \tau)$ and $c(r, \theta; \tau)$ respectively. The corresponding LT of the above two phasors are represented here as $\tilde{\varphi}(r, \theta; s)$ and $\tilde{c}(r, \theta; s)$. Following the linearized time-dependent formulation of [175] related to the mobility of charged dielectric spherical particles affected by surface conductance (SC) and concentration polarization (CP) assuming weak field and thin EDL, the governing equations for $\tilde{\varphi}(r, \theta; s)$ and $\tilde{c}(r, \theta; s)$ can be written as:

$$\nabla^2 \tilde{\varphi} = 0 \quad ; \quad \nabla^2 \tilde{c} = k^2 \tilde{c} \quad ; \quad k^2 = s \frac{a^2}{D} \quad \text{in } \mathcal{V}, \quad (7)$$

where \mathcal{V} denotes the unbounded expanse of a symmetric electrolyte of ionic diffusivity D . The appropriate boundary conditions prevailing on the surface of the spherical particle ($r=1$), supplementing eq. (7) are [175]:

$$\frac{\partial \tilde{\varphi}}{\partial r} = \frac{\partial \tilde{c}}{\partial r} = -Du \nabla_s^2 (\tilde{\varphi} + \tilde{c}) \quad \text{or} \quad r = 1, \quad (8)$$

where Du represents the Dukhin number (ratio between surface and bulk conductance) and ∇_s^2 is the surface Laplace operator. Closure is provided by imposing the far-field conditions:

$$\tilde{\varphi} \rightarrow -\tilde{E}(s)r \cos \theta \quad ; \quad \tilde{c} \rightarrow 0 \quad \text{as} \quad r \rightarrow \infty, \quad (9)$$

with $\tilde{E}(s)$ denoting the LT of the ambient time-dependent field.

Following [177], the slip velocity generated at the edge of the thin EDL surrounding the particle can be expressed as:

$$\vec{u}_s = \zeta_0 \nabla_{\parallel} \tilde{\varphi} - 4 \log(\cosh \zeta_0/4) \nabla \tilde{c} \quad \text{on} \quad r = 1, \quad (10)$$

where ζ_0 is the zeta potential of the dielectric particle related to its intrinsic charge and ∇_{\parallel} represents the surface gradient.

An explicit solution for $\tilde{\varphi}$, \tilde{c} , and \vec{u}_s can be readily obtained from eqs. (6-10) depending on the parameters $k(s)$, Du , and ζ_0 [175] and by imposing the condition for a force-free colloid, the particle mobility $\tilde{U}(s; \zeta_0, Du)$ for a harmonic signal of unit amplitude (i.e., $\tilde{E}(s) = 1$) can be determined [175]. Consequently, the mobility LT of the same particle under the present asymmetric triangular periodic signal $\tilde{E}(s) = \tilde{F}_{\pm}(s)$ can be written as $\tilde{U}_1(s; \zeta_0, Du) = \tilde{F}_{\pm}(s) \tilde{U}(s; \zeta_0, Du)$. Furthermore, since the colloid motility is assumed to be mostly affected by the fast transients (short time scales) of the signal compared to its periodic (long time) nature, the resulting transient mobility can be determined by considering the limit of large k in eq. (2.20) of [175], resulting in:

$$\lim_{s \rightarrow \infty} \tilde{U}_1(s; \zeta_0, Du) \sim \left[c_1 + \frac{c_2}{s^{1/2}} \right] \tilde{F}_{\pm}(s) + 0 \left(\frac{1}{s} \right), \quad (11)$$

where

$$c_1 = \frac{\zeta_0}{1+Du} ; \quad c_2 = 2Du \frac{\sqrt{D}}{a} \left[\frac{4 \log(\cosh \frac{\zeta_0}{4}) + \zeta_0 Du}{1+Du} \right]. \quad (12)$$

Since the time-dependent mobility (depending on T and t_1) is defined as $U_1(t) = \mathcal{L}^{-1}\{\tilde{U}_1(s)\}$, its average value over one cycle following eqs. (5) and (6), is given by:

$$U_1(t) \sim \text{Re}\{U_1(\tau)e^{i\omega t}\}, \quad \text{where } U_1(t) = \mathcal{L}^{-1}\{\tilde{U}_1(s)\}.$$

Next, we evaluate the average value of $U_1(t)$ over one cycle following eq. (5), by invoking eq. (6) which renders:

$$\bar{U}_1 = \frac{1}{T} \int_0^T U_1(t) dt = \frac{1}{T} \mathcal{L}^{-1} \left\{ \frac{\tilde{U}_1(s)}{s} \right\} \Big|_{s=T} = \frac{c_2}{T} \mathcal{L}^{-1} \left\{ \frac{\tilde{F}_+(s)}{s^{3/2}} \right\} \Big|_{s=T}. \quad (13)$$

Finally, substituting eq. (3) in eq. (13) renders for the “reverse” case:

$$\begin{aligned} \bar{U}_1(t_1, T) &= \frac{c_2}{t_1 T} \mathcal{L}^{-1} \left\{ \frac{1}{s^{7/2}} \left[1 - \frac{T}{T-2t_1} (e^{-st_1} - e^{-s(T-t_1)}) - e^{-sT} \right] \right\} \Big|_{t=T} \\ &= \frac{4c_2}{15\sqrt{\pi}t_1 T} \left\{ T^{5/2} - \frac{T(T-t_1)^{5/2}}{T-2t_1} + \frac{Tt_1^{5/2}}{T-2t_1} \right\}. \end{aligned} \quad (14)$$

Since the mobility expression in eq. (14) depends (for a prescribed T) on t_1 and in lieu of the relation $F_+(t, t_1) = -F_-(t, t_1)$, it is evident that the corresponding “reverse” and “forward” mobilities act in precisely opposite directions and are symmetric with respect to the “asymmetry”

parameter λ (t_1/T) (see Figure 1). Thus, considering for example the case of $1/2 > \lambda > 0$ (“forward” signal), collecting terms in eq. (14) leads to the following expression for the particle mobility in terms of the asymmetric parameter $2\lambda = 1 - 4t_1/T$:

$$\bar{U}_1(\lambda) = \frac{c_2}{15\sqrt{\pi}} \frac{T^{1/2}}{(1-2\lambda)} \left\{ 16 + \frac{(1-2\lambda)^{5/2} - (3+2\lambda)^{5/2}}{1+2\lambda} \right\}. \quad (15)$$

The maximum mobility is attained at $\lambda = 1/2$ (sawtooth signal) where $\bar{U}_1(1/2) = \frac{2c_2}{15\sqrt{\pi}} T^{1/2}$, and the minimum mobility is found at $\lambda = 0$ (symmetric triangular signal), namely $\bar{U}_1(0)$. Note also according to eq. (12b) that $\bar{U}_1 = 0$ when $\zeta_0 = 0$. Thus, one can define for example the normalized mobility asymmetry parameter $1 > q(\lambda) > 0$ by virtue of eq. (15) for positive values of lambda (“forward”) as

$$q(\lambda) = 1 - \frac{\bar{U}_1(1/2) - \bar{U}_1(\lambda)}{\bar{U}_1(1/2) - \bar{U}_1(0)} = 1 - \frac{2(\lambda+7) + \frac{(1-2\lambda)^{5/2} - (3+2\lambda)^{5/2}}{1-2\lambda}}{(15-9\sqrt{3})(1-\lambda)}, \quad (16)$$

such that $q(0) = 0$ and $q(1/2) = 1$ and a symmetric relation for negative values of λ (“reverse”) as depicted in Figure 1. Eq. (16) is plotted in Figure 4 and compared against the experimental measurements. The numerical results suggest that the asymmetry mobility parameter for both signals ($-1/2 < \lambda < 1/2$) can be also approximated by the following rather simple expression (see comparison in Figure 4):

$$q(\lambda) = 2|\lambda|. \quad (17)$$

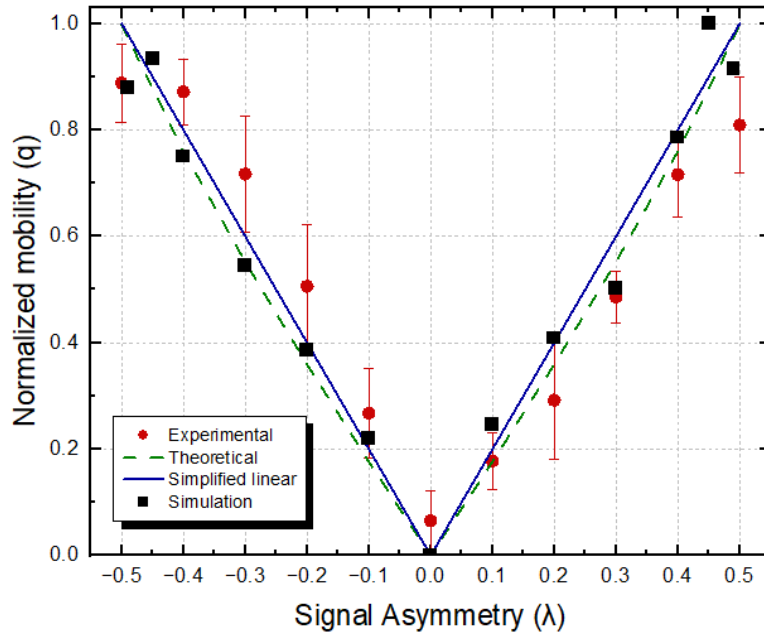


Figure 4: Normalized 5.0 μm particle absolute velocity data as a function of signal asymmetry at 2 kHz and 183.3 V/cm. “Forward” and “reverse” sawtooth signals correspond to 0.5 and -0.5 and act in opposite directions. Mobility measurements show a good qualitative agreement with the theoretical model (eq. 16) and the simplified linear model (eq. 17).

Appendix C

Experimental results for Ag-PMMA particles in an asymmetric AC field

A suspension of polydisperse (5 – 45 μm) Ag-PMMA particles (Cospheric LLC) was prepared in DI water (0.055 $\mu\text{S}/\text{cm}$) with the addition 0.1 wt% Tween-20 (Sigma-Aldrich) to mitigate aggregation and adsorption of particles to the electrode surface. The samples were exposed to a range of field strengths and frequencies of the forward and reverse sawtooth signals. Representative points are shown in the table below alongside data for the largest dielectric particle measured for ease of comparison. The general trend seen for dielectric particles under the AFEP effect is a reduction in velocity as size increases. However, under all conditions, the Ag-PMMA particles move with a much higher velocity despite being 2-4 times larger. Zeta potential measurements of the Ag-PMMA samples revealed an average zeta potential of -32.6 mV with a standard deviation of 10.4 due to rapid sedimentation and polydispersity.

Table 1: Table summarizing velocity data for Ag-PMMA and PS beads under a range of conditions.

Bead type	Diameter (μm)	Signal Symmetry	Field Strength (V/cm)	Frequency (kHz)	Velocity ($\mu\text{m}/\text{sec}$)
Ag-PMMA	41	Forward ($\lambda = 0.5$)	183	0.5	19.4
	31	Forward ($\lambda = 0.5$)	216	0.05	59.6
	31	Forward ($\lambda = 0.5$)	216	1	10.7
	31	Reverse ($\lambda = -0.5$)	216	1	11.4
PS	9.4	Forward ($\lambda = 0.5$)	183	1	4.9
	9.4	Reverse ($\lambda = -0.5$)	183	1	3.9
	9.4	Forward ($\lambda = 0.5$)	183	0.5	6.4
	9.4	Forward ($\lambda = 0.5$)	183	0.05	2.3
	9.4	Forward ($\lambda = 0.5$)	216	1	6.5